Fabrication of ultra-thin graphene oxide films enhanced by bio-interfactants

Dissertation

approved for the degree of
Doctor of Engineering
– Dr.-Ing –

Faculty of Production Engineering
Department of Production Engineering
University of Bremen

by

Felipe Perez

Bremen, July 2020

Fraunhofer

IFAM

Universität Bremen

Herstellung von durch "Bio-Interfactants" optimierten ultradünnen Graphenoxidschichten

Vom Fachbereich Produktionstechnik
der
Universität Bremen

zur Erlangung des Grades
Doktor-Ingenieur
genehmigte

Dissertation
von
Felipe Perez

Bremen, Juli 2020

O glaube, mein Herz, o glaube:
Es geht dir nichts verloren!
Dein ist, ja dein, was du gesehnt!
Dein, was du geliebt,
Was du gestritten!

O glaube
Du wardst nicht umsonst geboren!
Hast nicht umsonst gelebt, gelitten!

Was entstanden ist
Das muss vergehen!
Was vergangen, auferstehen!
Hör' auf zu beben!
Bereite dich zu leben!

O Schmerz! Du Alldurchdringer!
Dir bin ich entrungen!
O Tod! Du Allbezwinger!
Nun bist du bezwungen!

Mit Flügeln, die ich mir errungen,
In heißem Liebesstreben,
Werd' ich entschweben
Zum Licht, zu dem kein Aug' gedrungen!

Sterben werd' ich, um zu leben!
Aufersteh'n, ja aufersteh'n
wirst du, mein Herz, in einem Nu!
Was du geschlagen
zu Gott wird es dich tragen!

— Gustav Mahler

1. Referee

Prof. Dr. –Ing. Lucio Colombi Ciacchi

Universität Bremen - Faculty of Production Engineering (FB4)

Am Fallturm 1 | 28359 Bremen - Germany

2. Referee

Prof. Dr.-Ing. habil. Sven Kerzenmacher

Universität Bremen - Fachgebiet Umweltverfahrenstechnik (FB4/FG14)

Leobener Str. 6 | 28359 Bremen – Germany

Defense date of Phd Thesis: 26th June 2020

Eidesstattliche Versicherung

Hiermit versichere ich, Felipe Perez, dass ich diese Arbeit ohne unerlaubte fremde Hilfe angefertigt habe, keine anderen als die von mir angegebenen Quellen und Hilfsmittel benutzt habe und die den benutzten Werken wörtlich oder inhaltlich entnommenen Stellen als solche kenntlich gemacht habe.

_____   _____
           Ort, Datum   Unterschrift

Abstract

Graphene-based materials have been emerging at a fast pace since the isolation of a single crystal in 2004 and the Nobel prize in physics for that in 2010. Due to the outstanding properties of graphene, new lines of research aim to address challenges in production and methods to strongly attach graphene onto surfaces. Addressing this challenge requires (i) efficient transport of graphene to surfaces where it, (ii) remains strongly attached and (iii) manifests the sought graphene-like properties. This thesis aims to address these points by exploring synergetic interactions between graphene oxide and biomolecules that act as linkers (here named "bio-interfactants"). A layer-by-layer method was devised, which allowed the formation of ultra-thin coatings that safeguarded the overlapping graphene oxide flakes. In order to characterize the attainment of graphene-like properties, a mild thermal reduction of these newly-devised materials was conducted. It was found that the choice of the bio-interfactant played a crucial role in the efficiency of achieving these properties. Besides that, the bio-interfactants allowed further verticals assemblies by repeating the layer-by-layer process. In that case, too, the bio-interfactants played a role in the scaling of coating properties and allowed the tailoring of thicknesses from ~5.5 nm to ~233 nm. After thermal reduction, the lowest coating thicknesses could be achieved with high degree of homogeneity, and the thicker coatings presented some level of expansion (puffing). Finally, the coating presented here was found to be a suitable material when employed as a hair cosmetic. A study case about the cosmetic benefits of this material and its potential role as a fundamentally new technology for hair cosmetics is presented in this thesis, too.

Keywords: Graphene, bio-nanocomposites, coatings; graphene oxide; hair cosmetics; nanomaterials; bio-interfactants; layer-by-layer; dip-coating; surface functionalization; anchoring

Zusammenfassung

Graphenbasierte Materialien entwickeln sich seit der Isolierung eines Einkristalls im Jahr 2004 und dem dafür verliehenen Nobelpreis für Physik im Jahr 2010 rasant. Aufgrund der hervorragenden Eigenschaften von Graphen, zielen neue Forschungslinien darauf ab, Herausforderungen in der Produktion zu bewältigen und Verfahren zur starken Haftung von Graphen an Oberflächen zu entwickeln. Dieses Unterfangen erfordert (i) den effizienten Transport von Graphen zu Oberflächen, an denen es (ii) fest gebunden bleibt, und (iii) die gesuchten graphenähnlichen Eigenschaften aufweist. Diese Arbeit zielt darauf ab, diese Punkte zu behandeln, indem sie synergetische Wechselwirkungen zwischen Graphenoxid und Biomolekülen untersucht, die als Linker fungieren (hier "Bio-Interfactants" genannt). Es wurde ein Schicht-für-Schicht-Verfahren entwickelt, welches die Bildung ultradünner Schichten ermöglichte und dadurch die Überlappung der Graphenoxidflocken sicherstellt. Um die erreichten graphenähnlichen Eigenschaften dieser neu entwickelten Materialien zu charakterisieren, wurde eine leichte thermische Reduktion durchgeführt. Es wurde festgestellt, dass die Wahl des "Bio-Interfactants" eine entscheidende Rolle für die Effizienz der Erreichung dieser Eigenschaften spielte. Darüber hinaus ermöglichten die "Bio-Interfactants" weitere vertikale Verbindungen, indem der Schicht-für-Schicht Prozess wiederholt wurde. Auch in diesem Fall spielten die "Bio-Interfactants" eine Rolle bei der Skalierung der Beschichtungseigenschaften und ermöglichten die Anpassung der Dicken von ~5,5 nm bis ~233 nm. Nach der thermischen Reduktion konnten die kleinsten Beschichtungsdicken mit hoher Homogenität erreicht werden und die dickeren Schichten zeigten eine gewisse Ausdehnung (Puffing). Schließlich wurde die hier vorgestellte Beschichtung als geeignetes Material für den Einsatz als Haarkosmetik identifiziert. Eine Fallstudie über die kosmetischen Vorteile dieses Materials und seine potentielle Rolle als grundlegend neue Technologie in Bereich Haarkosmetik wird ebenfalls in dieser Arbeit vorgestellt.

Stichworte: Graphen, Bio-Nanokomposite, Beschichtungen; Graphenoxid; Haarkosmetik; Nanomaterialien; Bio-Interfactants; Schicht-für-Schicht; Tauchbeschichtung; Oberflächenfunktionalisierung; Verankerung

Acknowledgments

Table of Contents

List of acronyms and symbols

Acronym	Definition
AFM	Atomic Force Microscope
BSA	Bovine Serum Albumin
CAS	Chemical Abstracts Service
CPS	Counts per second
CVD	Chemical Vapor Deposition
cmGO	Chemically modified Graphene Oxide
GO	Graphene oxide
GO-Bio$_{nanocoating}$	Layer-by-layer nanometric coating of bio-interfactants and graphene oxide
HOPG	Highly oriented pyrolytic graphite
IEP	Isoelectric Point
LAC	Laccase from Trametes versicolor
LbL	Layer-by-layer
LSCM	Laser Scanning Confocal Microscopy
n	Index for number of process repetitions (for example in $(GO)_n$)
N	Sample size
PDB	Protein Data Bank
rGO	Reduced graphene oxide
rGO-Bio$_{nanocoating}$	Layer-by-layer nanometric coating of bio-interfactants and reduced graphene oxide
SDS	Safety Data Sheet
SEM	Scanning electron microscopy
TGA	Thermogravimetric Analysis
trGO	Thermally reduced Graphene Oxide
upGO	Supernatant fraction of a GO water dispersion
UV-Vis	Ultraviolet-visible spectroscopy
XPS	Photoelectron Spectroscopy

List of Figures

1 Introduction

1.1 Motivation

In a broader sense, this work was conducted with the motivation to explore the fringes of knowledge regarding the production and application of graphene coatings. Graphene is a unique 2D material that poses to revolutionize many areas of modern industry as it has outstanding properties; most popularly spread are the mechanical and electrical qualities. Such properties alone would probably suffice to justify a modest wave of research on the material. However, graphene brings the combination of many other properties simultaneously, garnering the attention of researchers from numerous fields. Instead of resulting in a modest wave of interest, graphene is currently among the most researched materials as since 2015 it topped "steel" in terms of the number of publications per year.

Graphene is far from having any fraction of the industrial importance of steel as of 2019. However, the bigger picture is that graphene is fundamentally unique being a real two-dimensions material that (besides theorized) could be isolated as of 2004[1], leading to the Nobel Prize in physics in 2010. The Prize was given "for groundbreaking experiments regarding the two-dimensional material graphene", which fostered the establishment of a research field for 2D materials; since 2010 many research groups, journals, and conferences emerged carrying in the title "2D materials" or "graphene".

The discovery of the material in 2004 enticed the imagination of engineers and scientists to develop new processing methods, test fundamental theories, and develop proof-of-concept prototypes to demonstrate the potential of graphene-containing technologies. This dissertation is driven by such motivations, as it aspires to:

(i) explore new developments in production technology of graphene-based materials,
(ii) interpret results from characterizations through the lenses of fundamental theories in order to translate phenomena in the nanometric scale to geometric models,
(iii) transfer knowledge developed in (i) and (ii) into a commercially relevant prototype with demonstrated benefits for the use of graphene, and finally
(iv) characterize and discuss through the scientifically lenses the entailing consequences for the use of graphene in such relevant field.

Within the multitude of graphene-based materials, this research focuses on producing coatings. Coatings can be seen as scaled-up versions of 2D materials; hence, graphene-based materials are natural candidates to fulfill demands typically imposed onto coatings. For example, due to their thinness and flexibility, graphene-based materials can intimately interact with the sub-micrometer roughness of other solids and scale the surface properties throughout a large area with minimal weight or thickness increase.

However, there is a shortage of methods to attach graphene onto substrates firmly. This adhesion problem was viewed as a core motivation for this thesis, although further challenges were also relevant to address. For example, besides having a

strong adhesive characteristic, the coating process should be simple, cost-effective, and scalable, yet engineered to offer desirable characteristics like homogeneity, ultra-thinness, transparency, and electrical conductivity.

A summary of these characteristics and their technological importance is listed below:

Strong attachment: A strongly attached coating is resistant to mechanical and chemical damage, leading to more extended periods of performance and less time out for maintenance. This characteristic is relevant for wearables, sensors, and parts that are exposed to mechanical loadings and fluids.

Simple and scalable: It is eminently desirable to implement processes with low number of steps, simple machinery, and use of materials that are abundantly available in the marketplace. Also, it is advantageous to use naturally scalable methods; which can be applied in a continuous line of production and do not require adjustments to process distinct sizes and shapes.

Homogeneity: Homogeneous coatings are beneficial for quality control, and the surface properties are even through the entire coated area, avoiding localized effects for the lack of coverage. These characteristics are desirable for coatings that must be protected from delamination and must protect the substrate from corrosive phenomena.

Ultra-thinness: An ultra-thin coating is a few nanometers thick, which means it has the benefit of being extremely light carrying less than 10 mg for each covered square meter and not interfering with extremely tight dimension constrains. Such requirements are relevant in aerospace and aeronautical purposes.

Transparency: Coatings that do not significantly alter the interaction between light and a coated solid are desirable for aesthetic and functional purposes. Such imperceptible color is relevant in the cases where a screen, a window, or an image has to be covered.

Electrical conductivity: A coating capable of carrying electrical charges is relevant as an anti-static material and even as a conductive material. These coatings can be applied to spread electric charges in aircraft made of composite materials or even carry electricity as a replacement of traditional cabling.

Individually, some of the properties listed above are not particularly outstanding. However, combining and delivering many of these properties simultaneously as advanced functional materials is where the most significant potentials of graphene-based coatings lie. It remains a challenge for researchers to map the achievable properties and engineer solutions that can deliver the right balance of properties.

1.2 State of the art

1.2.1 Research timeline of graphene

The timeline of research on graphene goes back over a long period. The events prior to the current understanding of the material are summarized in Figure 1. One of the earliest recorded research associated with graphene goes back to 1859 where Benjamin Brodie devised a method to produce graphene oxide; at the time he coined the material "graphon".[2] In 1947, P. R. Wallace made theoretical predictions of the band structure of "a monolayer of graphite" (graphene).[3] Next year, published in 1948, Ruess and Vogt observed few-nanometers thick graphene oxide flakes on a TEM grid while doing experiments with the graphene oxide suspension.[4]

In 1958, a century after the first graphene oxide synthesis, Hummers *et al.* devised an enhanced method to synthesize graphene oxide[2], which, is vastly used in modern research of graphene-based materials. Following up on the research from Ruess and Vogt, in 1962, Boehm *et al.* identified single-layer flakes of reduced graphene oxide (at the time "graphite oxide").[5] The researcher coined the name "graphene" to this material in 1986, to distinguish the single-layer material from the mineral (and the 3D crystal) from "graphite". The ending "ene" was to allude to the aromatic nature of the material.[5]

Finally, in the current century, Andre Geim united some ideas he had (not related to the literature mentioned above) and challenged a new Ph.D. student to make films of graphite "as thin as possible". In the process, Geim observed that scotch tape was already being used as a technique to cleave HOPG and expose a fresh surface of graphite to provide a reference sample for scanning tunneling microscopy measurements. For years the tape used to "clean" the HOPG was simply discarded, but due to the challenge at hand Geim observed that disposed tape was carrying the answer to achieving a graphite speck "as thin as possible".[6]
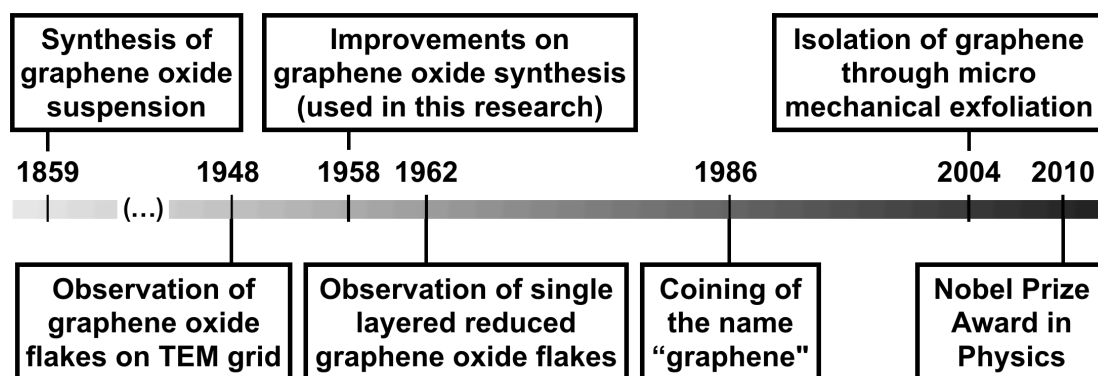
Figure 1 - Timeline of events regarding the discovery of graphene.

The Scotch tape method can be used to cleave crystals of graphite until a single layer of graphene is simply attached to the tape. Geim and his colleagues mastered this exfoliation method, developed a transfer technique, and added electrodes on the material. The groundbreaking discovery depended on two parts: (i) isolating the single

sheet of graphene and (ii) measuring the electric properties of the material. Not only the data demonstrated the superior electrical conductivity but also the material remained stable as a 2D crystal under ambient conditions.[6]

In 2010 the Nobel Prize in physics was awarded to, now laureates, Andre Geim and Konstantin Novoselov "for groundbreaking experiments regarding the two-dimensional material graphene". In view of past observations of graphene-like materials stemming in 1859, Geim attributes the current interest in the material to its actual measured properties.[6]

Since the awarded paper in 2004, the number of publications containing the word "graphene" on their title has increased in exceptional rate, as presented in Figure 2. From the range of few to dozens of publications yearly, the research on graphene was magnified to thousands of papers published yearly. In 2015 the number of publications containing "graphene" in the title surpassed that of "steel".

Interest in other materials are also plotted in Figure 2 for a better perspective. In the time frame from 1992 to 2018 steel and graphite remain materials with a high number of publications and small oscillations year-over-year (best observed in logarithmic scale). Papers about nanotube express a rapid growth, from single-digit publications yearly in 1992 to its maximum scientific output in 2014, followed by a steady decrease since that year. From being a niche topic with less than 100 publications yearly, nanotubes became a mainstream topic (over 1000 publications/year) in 5 years. For graphene, the same growth happened in two years.
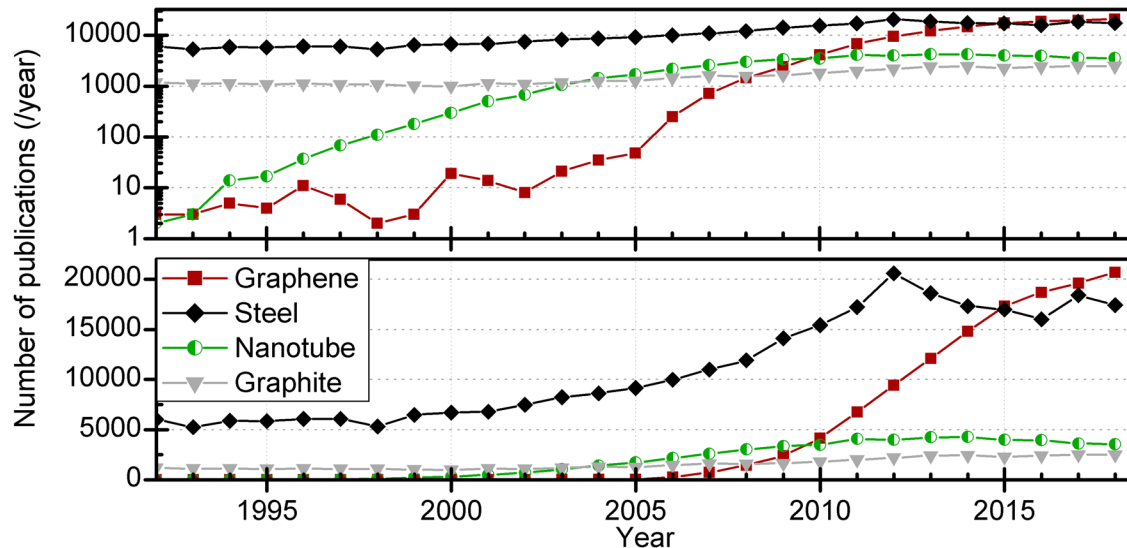
Figure 2 - Scientific output of diverse materials in the last years. Both charts (top and bottom) represent the same dataset but in logarithmic and linear scale. Y-axis indicates the total number of published papers, including the keyword (graphene, steel, nanotube, or graphite) in the publication title. The values provided here are indexed publications in GoogleScholar and do not include "patents" and "citations". The nascent research on graphene is already departed from its initial stage and like many other technologies is likely to follow the "the hype cycle"[7], adapted and represented in Figure 3. This curve is a visual way of representing the stages that new technologies go through, from conception to maturity. The visibility of new technologies starts to emerge after a technology trigger and develops quickly towards a peak of inflated expectations. After

this, the challenges of translating the technology into real-world solutions subdues the expectations. This challenge brings the technology to a trough of disillusionment; such depression is then slowly recovered by the slope of enlightenment and bringing the technology to a plateau of productivity.
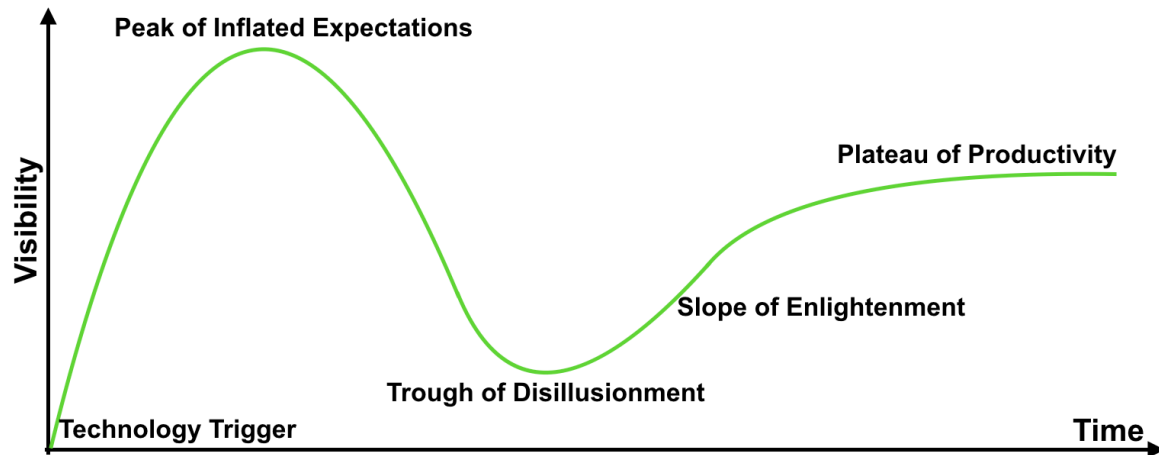
Figure 3 - The hype cycle curve. It represents the visibility of a technology through its developmental stages.

This hype-cycle curve tells the story of carbon nanotubes.[8] In 1991, the paper[9] on carbon nanotubes published by Sumio Iijima triggered a broad interest in the material, and very soon its visibility brought promises like space elevators and revolution in silicon transistors. The hype did not live to its potential, and bad news were in the horizon: There were increasingly more safety concerns involving carbon nanotubes[10], graphene entered the arena of nanomaterials and shifted the interest towards the 2D carbon counterpart, and in 2013 Bayer Materials Science shut down the production of nanotubes.[8] Slowly, carbon nanotubes start to be justifiable in individual cases like the aerospace industry[8]. Also, new production techniques bring the technology closer to real-world applications.[11,12]

Another example of the employment of groundbreaking materials is the case of carbon fiber. With first production in 1860 and further process developments in 1960[13], by 1978 it would still only be used in special cases like military aircraft. During the 1980's it was slowly added in Formula One cars and small components of airliners[14]. It was only since 2007 that a jet airliner (Boeing 787) implemented vast proportions of its fuselage made from carbon fiber components.[15] In this century, carbon fiber is slowly being implemented in the production line of high-volume industries, for example in 2013 with the production line of the carbon-fiber chassis of the BMW i3 electric car.[14]

These examples of carbon fiber and carbon nanotubes reveal clues of what might be the trajectory for graphene. In the case of graphene, the technology trigger happened in 2004 with the research mentioned above[1] and was further fostered by the Nobel Prize in 2010. The rate of published papers in the field was substantially increased (evident in Figure 2), and many new pieces of research indicate the immense potential of graphene. Following the hype-cycle trend (Figure 3), possibly the next steps in the research timeline of graphene will be characterized by significant challenges before graphene's properties can be translated into mainstream technologies.

1.2.2 Definition of graphene and graphene oxide

The word "graphene", as mentioned above, was introduced in 1986[16] and replaced previous terms like "carbon layer", "single graphite layer" and "carbon sheet". The name graphene refers to the building block of a graphite crystal and is characterized by a series of coplanar neighbor aromatic carbons, each bond to other three carbons (represented in Figure 4a). Nevertheless, throughout the discovery of new materials with similarities to graphene, researchers started to use the term "graphene" loosely. Slight changes in the chemical structure of "pure graphene" can still result in materials with "graphene"-like properties, which only contributes to the unprecise notation.
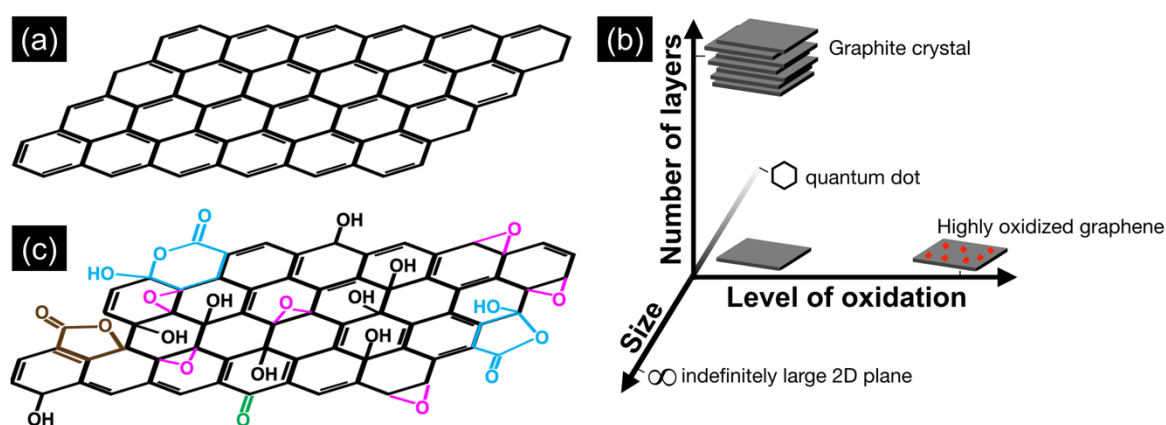
Figure 4 – Types of Graphene (a) Structure of graphene, characterized by carbon atoms organized in a planar polyaromatic structure. All carbon atoms in the honeycomb structure sp^2 hybridization state. (b) Microstructural fluidity of graphene with three distinctive categories. (c) Graphene oxide structure proposed by Gao et al.[17] (adapted). Functional groups are highlighted by colors: epoxy (in pink), ester of tertiary alcohol (in brown), ketone (in green), hydroxyl (in black) and lactol rings (in blue).

Sometimes authors use terms like "graphene-based", "graphene-like" or specific acronyms instead to acknowledge some deviation from the pure form of graphene. A useful way to characterize and denominate such materials is by informing three other characteristics[18] as represented in Figure 4b).

The three important dimensions in which graphene can be changed are the following:

(i) Number of layers: This refers to the geometrical stacking of continuous graphene layers. In the lowest extreme, the number is 1 and characterizes the condition of graphene. In the highest extreme (indefinite value) it characterizes a graphite crystal.

(ii) Level of oxidation: This axis is generally useful for characterizing graphene oxide and reduced graphene oxide. It can be quantified by the atomic proportion of O/C or also by the sp^3/sp^2 bonds. Graphene is characterized by the extreme low case (no oxygen and no sp^3 bonds). On the other extreme, the high proportion describes a form of highly oxidized graphene.

(iii) Size: The size of the graphene-like particle is typically measured as the average lateral dimension. In the minimal case, the size approaches that of quantum dots or even benzene. On the extremely large side, it still describes the characteristic of graphene.

Graphene oxide (Figure 4c) is considered to be the solid particles resulting from a Hummer's method process. Since many suppliers and researchers make their own graphene oxide, it is useful to characterize the GO particles following the same guidelines for graphene (lateral size, degree of oxidation, and number of layers). The GO structure can be chemically changed to a form similar to graphene (along the horizontal axis in Figure 4b), and can receive several denominations, for example "reduced graphene oxide" (rGO), "chemically modified graphene oxide" (cmGO) or "thermally reduced graphene oxide" (trGO).

In the chapters of technical discussion the terms "graphene-based" and "graphene-like" are used in order to refer to graphene with some level of modification (along the axes in Figure 4b).

1.2.3 Graphene processing methods

There are multiple routes to achieve graphene. The methods can be categorized by top-down or bottom-up approaches, and some examples are summarized in Figure 5. Comprehensive reviews on processing methods can be found elsewhere[19–21].
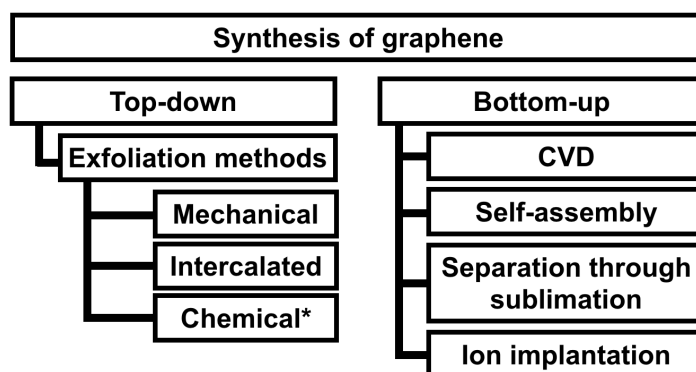
*Figure 5 - Summary of production methods of graphene. * Chemical exfoliation of graphite can be used to produce graphene oxide, in which case it requires further chemical processes to convert back to graphene.*

Top-down methods require raw materials like graphite or highly oriented pyrolytic graphite (HOPG) and use exfoliation mechanisms to peel the layers of graphene from the bulk crystal. The "mechanical" approach requires an adhesive tape and can cleave layers of graphite until a single flake of graphene is isolated.[1] The "intercalated" method[22] is a non-oxidative way of exfoliating graphite; Brønsted acids can intercalate between graphite and split graphene layers without transfer of charges. Besides this inert intercalation, there is the chemical exfoliation of graphite, which in contrast oxidizes the graphene layers during the exfoliation process.[2]

The bottom-up methods (listed on the right part in Figure 5) were devised after the isolation of graphene in 2004. The chemical vapor deposition (CVD) is a process that produces high purity graphene crystals on specific targets, commonly copper. "Self-assembly" methods start with smaller carbon-containing molecules like glucose[23] or ethanol[24] in order to grow graphene-like structures in a controlled way. "Separation through sublimation" is a process that starts with SiC wafers and the Si atoms are removed through sublimation; the remaining C atoms form graphene crystals.[25]

Lastly, "ion implantation"[26], is a technique that bombards a substrate with carbon ions and forms multi-layer graphene films on large substrates.

Currently, the methods vastly used and readily available for purchase are "CVD graphene" and "graphene oxide". The CVD-derived graphene offers a high degree of purity and is sold in a limited number of substrates, making an ideal material for measurements and small-scale experiments. The disadvantage is the cost of ~155,000 €/m² (Annex 1) and the challenge of transferring to other substrates[27]. The other commercially available option is graphene oxide (Annex 1). Its disadvantage is a high degree of oxidation on the flakes and the presence of impurities. The advantage is the ease to manipulate the liquid media and the cost of the material. Assuming single side specific surface area of 368 m²/g[28] and the current cost of graphene oxide, the price is in the range of ~0.08 €/m² (Annex 1).

The staggering difference of 6.3 orders of magnitude in terms of the cost of covered area between both materials is enough reason to research methods that can convert graphene oxide into its original form once it is attached on a target substrate.

The processes that chemically convert graphene oxide into graphene are plentiful. The most practical is merely heating to temperatures above ~175°C.[29,30] Simple chemical reductions with liquid or gas agents are also efficient in converting graphene oxide back to graphene[31–35]. Other more complex reduction processes may also be applied for a distinct degree of reduction, for example: heating up to 2400°C in vacuum[36], high hydrostatic pressure in super-critical liquids[37], microwave[38], UV irradiation[39] or combination of these processes[40,41] such processes heal GO towards graphene-like structure, and therefore graphene-like properties.

In an industrial point of view the processing of graphene oxide as a precursor for graphene stands out for three reasons: (i) high degree of flexibility[31] for chemical reductions, (ii) low cost for area (as mentioned above), (iii) ease in manipulating liquids comparing to manipulating individual atom-thin films.

1.2.4 Graphene and graphene oxide and adsorptive interactions

Understanding the attractive interactions between graphene-based materials and other materials is critical to strategize techniques that employ the right force between the two materials. In some cases, it is desirable to explore strong interaction between two materials and on other occasions, weaker interactions.

In a broad sense, these strategies are essential during two distinct stages: First during the production stages of graphene-based materials and second during the performance of such material. As an example, in the realm of coatings, strong interactions may be desirable between a graphene-based material and the substrate to be covered (production stage). On top of that, it might be desirable to develop such coating in a way that it manifests weak interactions with the external environment, resulting in an inert "self-cleaning" surface (performance stage). These and other examples of interactions are important to be viewed in a fundamental way to develop

better strategies and explain macroscopic effects that result from interactions in the nanometric scale.

1.2.4.1 Ionic Interactions, Hydrogen Bonding and van der Waals interactions

The driving forces stemming from opposite charges are vastly different between graphene and graphene oxide. Graphene has a neutral state of charges across the molecule and no permanent dipoles. Although dipole-induced dipoles can be created to some extent[42], graphene cannot be dispersed in water in its natural state. Typically, graphene tends to be well dispersed in solvents with surface tension close to 40 mJ/m^2 or with good agreement with Hilderbrand solubility parameters.[43]

Graphene oxide, on the other hand, is functionalized with several chemical groups (Figure 4c) that hold permanent dipoles. These features allow easy dispersibility in water and several other solvents, particularly with higher surface tension in the range of 60 mJ/m^2.[44] In contrast to graphene dispersions[43], graphene oxide dispersions have the key characteristic of allowing a higher proportion of single sheets dispersed in liquid media.[45]

Regarding adhesion towards solid substrates, both graphene and graphene oxide are flexible ultra-thin materials, allowing an intimate conformation on substrates which leads to a high adhesion due to van der Waals interactions[1].[46–48] Nevertheless, there is a high distinction of adhesion between graphene and graphene oxide; peeling tests on soda-lime glass substrate indicated that graphene oxide has one order of magnitude of stronger adhesion (to glass) than its reduced form (graphene-like) has to glass.[48]

This distinction results in other interesting phenomena: (i) if a fracture is induced on a graphene coating, the material can "self-unpeel"[2], even after the fracture event, and assemble on itself because it is energetically unfavorable to remain as a coating on the substrate.[49] Graphene oxide, in contrast, is more resistant to crack propagation[50] and confines fractures that are inflicted on the surface.

Interactions with biological materials (relevant to this work) also reveal interesting distinctions between graphene and graphene oxide. Researchers[51,52] performed molecular dynamics simulations of the interaction between amino acids and graphene or graphene oxide and elucidated interesting distinctions. In general, amino acids are attracted to graphene in vacuum conditions. In the presence of water, the forces of attraction were significantly smaller, favoring some degree of solvation due to a negative Coulombic contribution. The researchers also observed that the van der

---

[1] Such effect results in interactions that are more similar to that of liquid-solid interactions than solid-solid.[47]

[2] Even causing fracture of its covalent bonds.

Waals contributions play a decisive role in the adsorption, particularly for amino acids with higher molecular weight.

The corresponding simulations on graphene oxide[52] (performed by the same research group) also showed both trends (i) larger amino acids correlated to higher adsorption forces (caused by the van der Waals component) and (ii) columbic forces facilitate solvation instead of adsorption. Despite similar fundamental behaviors between these amino acids and the graphene or graphene oxide, the latter provides 25% of higher binding energies.[52]

1.2.4.2 π-π interactions

The aromatic rings in graphene and graphene oxide are necessary conditions to allow this interaction and require, therefore, other molecules with such aromatic rings to allow the π-π interaction. Moreover, the geometric shape of both interacting materials can be decisive to allow multiple π-π bonds; particularly when both materials face each other with large flat areas[1].[53]

This driving force results in a noncovalent bond and is a highly relevant factor for graphene, since it has the highest concentration of π systems (ratio of sp^2/sp^3 = 100/0). As for graphene oxide, depending on its oxidation state, the proportion sp^2/sp^3 can be from 33/66[54] to 90/10[55]. As a consequence, graphene adsorbs small aromatic molecules (including biological materials with aromatic moieties[56]) to a larger degree than graphene oxide.[57] Furthermore, from a processing point-of-view, these small molecules can even be used to exfoliate graphene and stabilize dispersions of it.[53]

1.2.4.3 Hydrophobic interactions

Due to its hydrophobic nature, graphene (and graphene oxide with high sp^2/sp^3 ratio) can interact with other hydrophobic substances. As a consequence, such materials can remain stable in organic solvents, macromolecules or even be stably embedded in hydrophobic polymers. Graphene can interact with the hydrophobic parts of ionic liquids, surfactants, and proteins. In such a way, this can be used as a strategy to stabilize it in hydrophilic liquids.[53,58,59]

On the other hand, graphene oxide has limited potential for such interactions since a proportion of the hydrophobic regions is replaced by polar groups (Figure 4c). Nevertheless, this partial gain of polarity makes the material have both natures: polar and nonpolar. Such property is denominated amphiphilic and can be taken advantage of in order to produce emulsion-patterned ultra-light materials.[36,60]

---

[1] Such geometrical effect was demonstrated when comparing graphene with carbon nanotubes. Both materials have the same chemical structure, however, due to the limited flat sp^2 areas of nanotubes it cannot be dissolved in the same aromatic compound.[267]

1.3 Research Scope

1.3.1 Research questions

This work can be viewed in several levels of analysis. Most fundamentally, it is under the general research questions posed by leading researchers in the field[61]:

- *Does graphene have a chance to become the next disruptive technology?*
- *Can graphene be the material of the 21st century?*

These inquiries[61] open a domain of more specific questions, and I pursued further knowledge more specifically in (i) the production of graphene-based coatings and (ii) using graphene oxide as a precursor to graphene. Such intention generated the question:

- *Are there advantages of processing graphene oxide instead of pure graphene in order to produce graphene-based coatings?*

This question was addressed in one or other way prior to this research[32,39–41,62–70], inspiring a more specific open question:

- *How can graphene oxide coatings be engineered in order to innovate in the field of coatings?*

The research question above was the ground zero for this thesis and led to a recent publication[46]. Alongside this question, further inspection followed:

- *What are the properties of these coatings?*
- *What are the phenomena behind the production of these coatings?*

The questions above are explored throughout chapter 2. With these results, I explored yet another question:

- *Could these coatings be used for a commercially relevant application? For which application?*

That last question can be briefly answered with "yes, as a hair cosmetic" and the intricacies of this observation are addressed in chapter 3 alongside with further research questions:

- *How does human hair change its properties by applying such coating on it?*
- *What is the performance of this material as a hair cosmetic?*
- *What are the phenomena guiding the interactions of hair and the coating?*
- *What are the safety considerations of using this material as a hair cosmetic?*

1.3.2 Research aim and approach

This research aims to report the process of the development of a new graphene-based coating. Throughout this report, several measurements were conducted using multiple machines; such effort was made to gain a better understanding of these graphene-based coatings. Alternatively, using the appropriate jargon for the field, the measurements intend to *characterize* the phenomenon pertaining to graphene-based coatings.

In materials science and engineering, characterization is viewed as the pathway to a holistic view of the relationship between structure, properties, processing, and performance, as represented in Figure 6.[71,72] In a recursive system, characterization facilitates the evolution of ideas and achievement of materials designed for specific purposes. This research aims to apply this view while tackling the core research question "How can graphene oxide coatings be engineered in order to innovate in the field of coatings?".
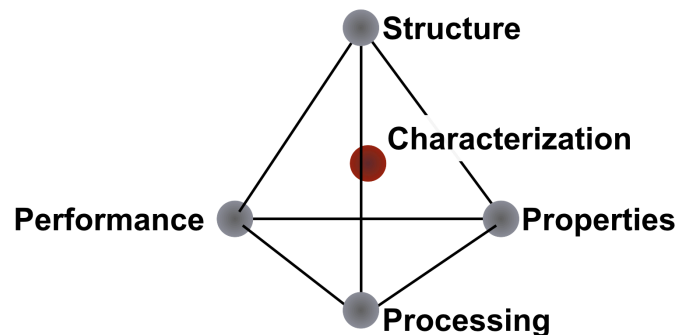
Figure 6 – Materials Science tetrahedron. Characterization is viewed as a core activity in order to unify the other aspects that are of concern for materials science and engineering.

More specifically, the research question was aimed at from two angles; (i) from the point of view of materials science and (ii) from the point of view of materials engineering. The distinction is that materials science aims to "develop or synthesize new materials"[72] and materials engineer aims to "create new products or systems using existing materials"[72]. Chapter 2 leans more towards materials science and chapter 3 leans more towards materials engineering.

In chapter 2, the aim is to explore the chemistry of graphene oxide in order to apply it as strongly attached coatings. The functional groups of graphene oxide were viewed as a hallmark for synergetic interaction with selected biomolecules. Such interaction was explored in water-based media through intercalated dip-coating deposition of biomolecules and graphene oxide. The phenomena guiding the assembly of this bio-composite was investigated using several techniques; traditional laboratory techniques and molecular dynamics were used to propose geometrical models for the graphene/bio-material interactions. Chapter 2 also investigates chemical transformations stemming from the thermal treatment of this material aiming to achieve graphene-like properties. Lastly in chapter 2, the robustness of the developed coating is put to test as a proxy for withstanding real-life applications.

In chapter 3, the aim is to apply the material developed in chapter 2 as a commercially relevant technology. It was identified that the technology from chapter 2 had potential when employed as a cosmetic for human hair. Besides assessing microstructural, thermal, and electrical measurements, other hair characterizations were conducted such as color effect and ease to comb. The wide range of characterizations were pointed towards having a comprehensive view of the application.

This work is concluded by a thorough discussion (chapter 4), which elaborates on the research questions and the results presented in chapters 2 and 3. Besides explaining general observations from this thesis, the aim of chapter 4 is to summarize the results in blocks of interconnected ideas and expose the bigger picture. Following that, one subchapter is dedicated to remark the final considerations of the case study. And finally, open questions and suggestions for future work are presented.

2 Development of graphene oxide nanometric coatings

2.1 Materials and methods

2.1.1 General overview and sample notation

The sketch overview of the process investigated in this research is shown in Figure 7b. The process requires (i) a substrate, (ii) a buffer solution with a bio-interfactant, and (iii) a graphene oxide (GO) dispersion. The coating assembly is made possible by dipping the substrate in the bio-interfactants, then in the GO dispersion. The intercalating process can be repeated, which characterizes it as a "layer-by-layer" process. The resulting material followed by this process (Figure 7b) is denominated GO-Bio$_{nanocoating}$. The process depicted in Figure 7a is a control experiment, without the use of bio-interfactants, and denominated GO$_{nanocoating}$. Both GO-Bio$_{nanocoating}$ and GO$_{nanocoating}$ can be thermally reduced (represented by "step 3" in Figure 7), in order to produce "thermally reduced" coatings.
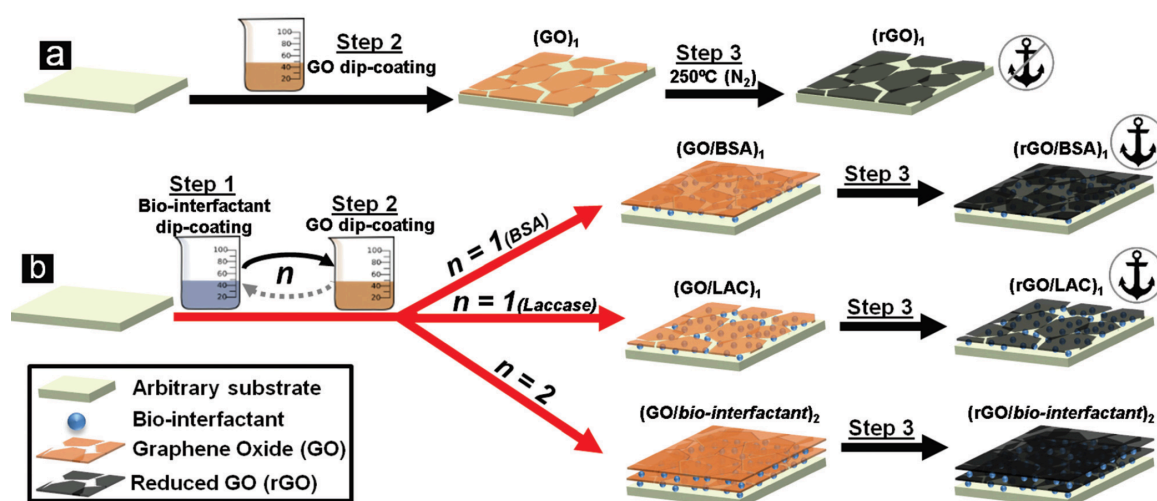
Figure 7 – Overview of processes. Extracted and adapted from Perez et al (Nanoscale, 2019,11, 4236-4247 - Published by The Royal Society of Chemistry). Overview of the processes used in this study. (a) Sequence of processes for coating an arbitrary substrate with rGO, by directly dipping in GO dispersion (step 2) followed by a thermal treatment process (step 3). (b) Process routes explored in this research, using a two-step process. In this strategy, step 1 and step 2 are iterative processes that can be repeated (first dipping in a liquid bio-interfactant formulation and later dipping in a GO dispersion), afterwards the material can be thermally treated (step 3). Anchor symbols represent adhesion quality of these coatings (characterized later in chapter 2.2.3)

The sample notations[46] and definitions are used as follows:

- "Substrate" refers to a flat material where the coating is deposited. Quartz, borosilicate, and polyimide are used as substrates.
- (GO)$_n$ is a coating made of GO where **n** is the number of combined dipping and rinsing processes in the GO dispersion, i.e. the number of step 2 repetitions (Figure 7a).
- (GO/LAC)$_n$ and (GO/BSA)$_n$ are referred to coatings based on bilayered repeating units where a bio-interfactant (LAC which refers to a mixture of

laccase and maltodextrin, or BSA which means Bovine Serum Albumin, respectively) is intercalated with GO in dipping processes for n times (always beginning with the bio-interfactant and ending with GO).

- After thermal reduction (step 3), the denominations above receive the letter "r" before "GO". For example, (GO/BSA)$_1$ becomes (rGO/BSA)$_1$ after step 3.

2.1.2 Protocols and characterization of starting materials

Extracted and adapted from Perez *et al.*[46]. Graphene oxide (GO) 4 mg/ml (purchased from Graphena, Spain) was diluted with deionized water (<0.1 µS cm−1 from arium® pro VF, Sartorius) to 1 mg/ml (reaching pH ~2.6). The addition of DI water in the dispersion produced the pH profile depicted in Figure 8.
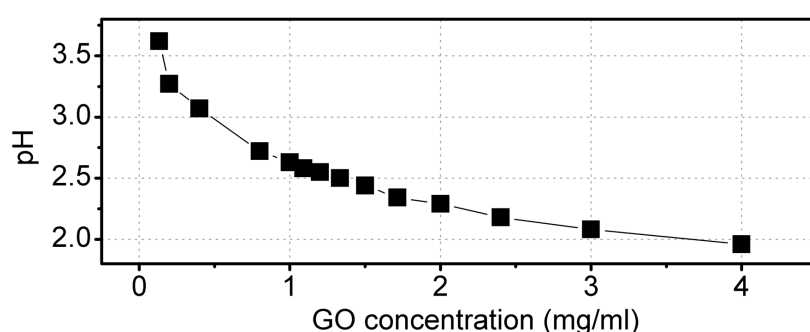
Figure 8 - Measurement of pH with increase of dilution of commercial GO dispersion. During the experiment the dispersion was constantly mixed with a stirring bar. Extracted and adapted from Perez et al (Nanoscale, 2019,11, 4236-4247 - Published by The Royal Society of Chemistry).

Bio-interfactants: LAC (laccase from *Trametes versicolor*, Sigma-Aldrich product number 38429, PDB code 1GYC), which in this commercial form has a concentration of ~6%$_w$ (Figure 9) or BSA (bovine serum albumin, Sigma-Aldrich product number A6003, PDB code 3V03) were diluted (0.2 g/L) in sodium acetate buffer solution. The acetate buffer solution (0.2 M at pH 4.75) was prepared with acetic acid and sodium acetate (reagent grade Sigma-Aldrich).

Absorbance @ 280 nm (1 cm path length)	Mixture concentration (mg/ml)	Molar absorption coefficient (for molecule 1GYC) $\varepsilon = n_w*5500 + n_y*1490 + n_c*125 = 61475$		
		n_w (# tryptophan)	n_y (#tyrosine)	n_c (#cysteine)
0.1434	2.1	7	15	5

Figure 9 – Light absorbance and molar absorption coefficient. Considering the theory and methods for estimating a polypeptide concentrations (details in[46], it was determined that the commercial mixture with LAC contains ~6.2% of enzymes and the remaining is assumed to be polysaccharides that have the function of stabilizing the enzyme. The equation that calculates the concentration is $A_\lambda = \varepsilon*c*L$, where A_λ is the light absorbance, ε is the molar absorption coefficient, c the concentration and L the path length. Extracted and adapted from Perez et al (Nanoscale, 2019,11, 4236-4247 - Published by The Royal Society of Chemistry). Substrates: Quartz glass (purchased from GVB, Germany) was cut in ~1×1, ~1.5×1.5 or ~1.5×8.0 cm with a diamond-coated saw blade. After being cut, the quartz was cleaned using a Piranha solution protocol. *Caution: piranha solution should be handled with great care.* Briefly, 1:5 ratio (H_2O_2 (30%) : H_2SO_4 (98%)) was prepared by pouring 75 mL of H_2SO_4 in a clean and dry beaker with a PTFE magnetic stirring bar. The beaker was placed in ice-bath glassware (bath temperature kept at 0 °C). Then 15 mL of H_2O_2 (30%) was added

slowly into the beaker (*caution for highly exothermic reaction*). The solution was mixed by the aid of the stirring bar. When a homogeneous phase is achieved, the solution is ready to be used. As the magnetic stirrer continues to mix, quartz was added in the solution where it remained for 10 minutes. After that, the quartz substrates were placed in a beaker with DI water for 5 minutes.

Next, the substrates were rinsed sequentially in two beakers with DI water and finally dried with a nitrogen gun. XPS confirmed the clean state of the quartz substrates (Figure 10). Borosilicate glass hydrolytic class 1 was acquired from Brand GmbH (product number 470-45). Polyimide film was purchased form Airtech (Termalimide film).

O 1s	Si 2p	C 1s	N 1s
59.27 ± 1.11	31.24 ± 0.71	9.26 ± 1.55	0.23 ± 0.06

Figure 10 - XPS evaluation of 14 positions on the total of 5 quartz samples treated with piranha solution protocol, showing the homogeneity of atomic concentrations inter and intra samples. The measurements are normalized atomic concentrations (%$_{at.}$, normalized for the content of O, Si, C and N). The carbon and nitrogen were considered impurities and subtracted from calculations of the coating atomic contents proportionally. Extracted and adapted from Perez et al (Nanoscale, 2019,11, 4236-4247 - Published by The Royal Society of Chemistry).

Gold coatings were applied at the edges of substrates (Figure 11) on samples where electrical conductivity was measured. The sputter procedure was conducted with EM ACE600 (Leica Microsystems, Germany) by adding 10 nm of Cr and then 100 nm of gold. The target substrates were tightly covered with aluminum foil on the areas that were not coated.
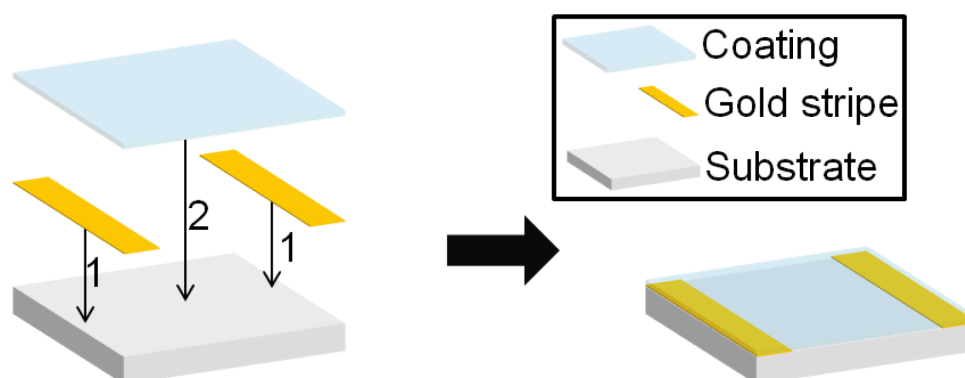
*Figure 11 - Sample preparation: Gold is sputtered on a substrate (1) before the coating process (2) for continuous electrical contact with the bottom part of the coating. Extracted and adapted from Perez et al (Nanoscale, 2019,11, 4236-4247 - Published by The Royal Society of Chemistry).*

Fabrication of layer-by-layer (LBL) films: step 1 (Figure 7) was performed by dipping the target substrate in a buffered dispersion of LAC or BSA for 1 h, followed by rinsing in DI water vigorously for about 5 seconds. Step 2 (Figure 7) was conducted by placing substrates in GO dispersion (1 mg/ml) for 15 min, followed by rinsing with DI water (5 seconds vigorously). The samples were then dried with a nitrogen gun until no apparent water drops were visible on the substrate.

The backside of the samples was cleaned immediately after the vigorous stirring with a delicate wipe towel in order to make sure that the layer was only formed on the top surface. For further layers depositions, steps 1 and step 2 were repeated (in the case of assembly with bio-interfactants). Films with multiple GO dipping (unassisted by bio-interfactants) were prepared performing consecutive repetitions of step 2.

Thermal reduction, step 3, was conducted in a chamber furnace with a feed of nitrogen. The cycle began with 90 min of nitrogen purge of the chamber at room temperature. Next, the heating started with the rate of 10 K/min until the target temperature (either 100°C, 180°C or 250°C). The temperature was kept at the target temperature for 10 minutes and finally let cool to room temperature (by turning off heat element).

2.1.3 Characterizations

Extracted and adapted from Perez *et al.*[46] (Nanoscale, 2019, 11, 4236-4247 - Published by The Royal Society of Chemistry). AFM images were obtained with NanoWizard 3 NanoScience (JPK Instruments AG, Germany) in tapping mode. X-ray photoelectron spectroscopy (XPS) was measured with a Kratos Ultra Facility using the following parameters: base pressure of 4×10^{-8} Pa, sample neutralization with <5 eV electrons. The element composition of the LBL systems is calculated by the total measured atomic concentration of the sample (which may also comprise the substrate) minus the proportion of species contained on the substrate, using Si as reference for proportion (it is assumed that GO does not contain Si). The background was corrected with Shirley method, and the curve fitting used GL(30). The layer thickness was calculated using signal attenuation form the quartz substrate.

It is assumed an exponential attenuation of the photoelectron Si 2p signal (which is attributed to the quartz), following the Beer–Lambert equation:[73]

$$I = I_0 \exp\left(-d/\lambda_{a,b}\right)$$

In the equation, d is the thickness of a continuous and homogeneous thin film, I is the intensity of electrons emitted from the coated substrate, I_0 is the intensity from the uniform substrate without coating. Symbol $\lambda_{a,b}$ is the inelastic mean free path (IMFP) from electron in species b (substrate) through material a (coating). The IMFP depends on the kinetic energy of the respective electrons in the coating, and it was assumed to be $\lambda_{org,Si2p}$ 3.95 nm[74] for Si 2p electrons which are characteristic for the substrate.

Light transmittance was measured with Specord 210 plus (Analytic Jena AG, Germany). Light absorbance was calculated by:

$$A = 2 - Log_{10}(T)$$

Where T is the transmittance measured by the device and A the absorbance. Samples measured with this technique were measured individually before dip coating in GO or bio-interfactants formulations in order to use a precise control reference. It was found that 90% of the signal contribution comes from a circular area with diameter a below 2 mm.
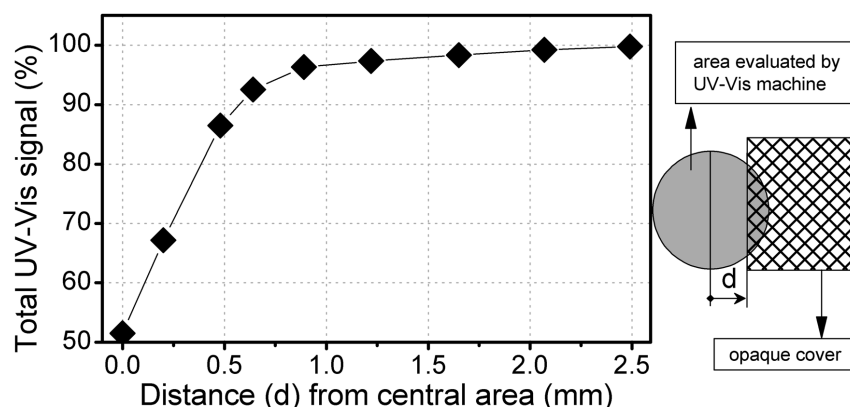
Figure 12 - Signal contribution of UV-Vis. This experiment was performed in order to measure the influence of coatings far from the center of the light spot. When d=0, that is, half the area of the measured spot is covered, only 50% of the light signal is detected. When the cover was 2.5 mm far from the central spot, over 99.7% of the signal was detected.

Electrical conductivity was measured with multimeter 15XL, Wavetek (sensitive up to 2 GOhm). Sheet resistance was calculated from the measured resistance and adjusted to the rectangular ratio of the films (Figure 11).

A universal mechanical testing machine (TA·XTplus 5 kg load cell) was used to peel the adhesive tape (tesafilm® transparent) with an angle of 180° at 5 mm/s. The pressure applied to the films beforehand had been 2.5 kg/cm^2 for 20 seconds. Molecules were graphically represented using Jmol or PyMol software (the PDB code of the represented BSA molecule was 3V03 and 1GYC for laccase from *Trametes Versicolor*). Endurance in ultrasonic bath was measured by the decay of the electrical conductivity of the coated samples. The results were also compared to commercial quartz coated with CVD graphene (Graphenea, Spain). The electrical conductivity was measured outside of the bath to avoid influence from the water. After measurement the samples were returned to the bath until the next measurement point. SEM characterizations were done with a Helios 600 machine at 5 kV.

Thermo-gravimetric analysis (TGA) was measured with TGA Q5000 (TA instruments, USA). Specific conditions are detailed with the experiments. Laser Scanning Confocal Microscopy was measured with VK9710 Keyence.

2.2 Results and Discussions

The next subchapters explore the interactions of the materials during the process depicted in Figure 7. These interactions are individually illustrated below in Figure 13.
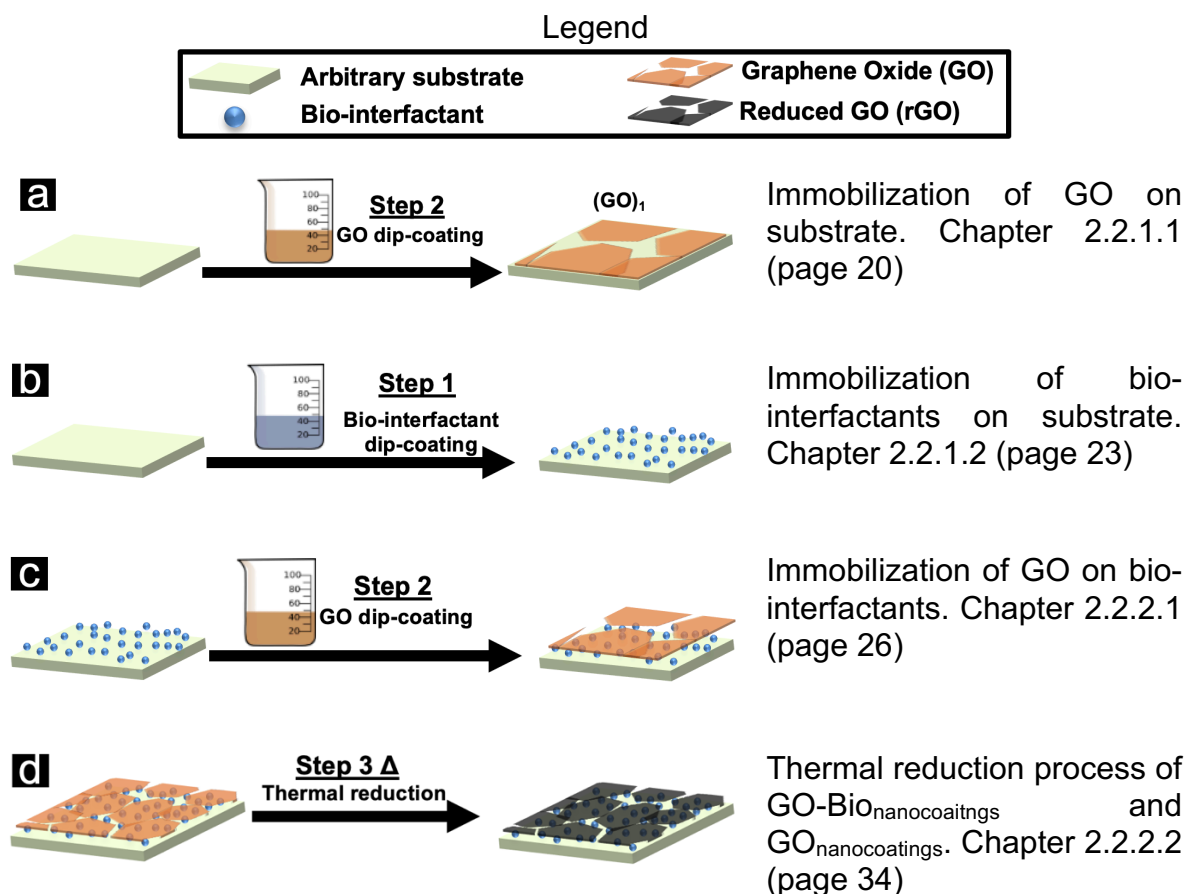
Figure 13 - Steps of the process illustrated individually, with the corresponding subchapter where the results and discussions are found (right column).

2.2.1 Immobilization of GO and bio-interactants individually

2.2.1.1 Immobilization of GO

As illustrated in Figure 13a, the attachment of GO on substrates was investigated. Substrates dipped in GO dispersion (following the protocol described in chapter 2.1.2) were investigated with UV-Vis, XPS, and AFM. The UV-Vis device was used in order to measure the mm-range reliability of the process, as it measures information from a ~3 mm^2 spot (more details in Figure 12). Seven individual samples were measured after dip-coating in GO, and the light absorbances are represented in Figure 14.
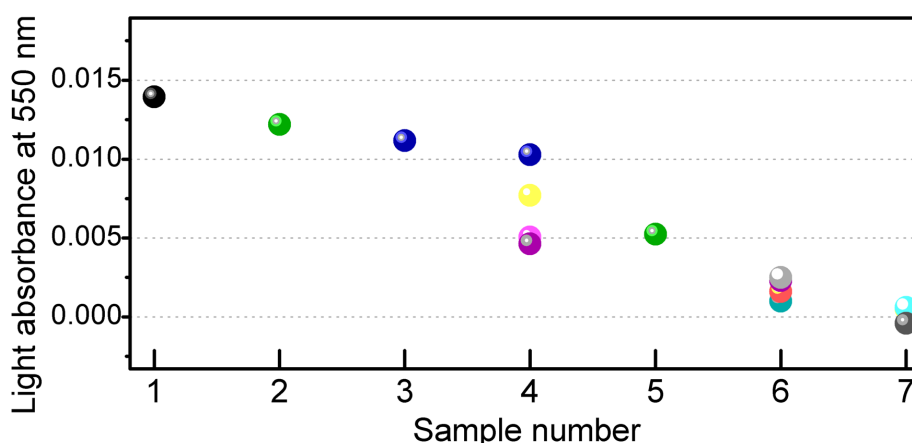
Figure 14 - Reproducibility of step 2 process on quartz glass measured by light absorbance at 550 nm. Different colors represent unique measurements conducted in different non-overlapping areas.

The reliability study indicated a high degree of variation of light absorbance among samples. Some samples were large enough for more than one measurement (samples 4, 6 and 7), and within them, too, a high degree of heterogeneity was observed. The broad range of values inter and intra samples indicate a high distinction of coverage even in the mm-scale.

This coverage variation was tested in two other substrates; polyimide and borosilicate. Alongside measuring inter and intra sample light absorbance, the substrates were tested for their surface tension with water. Figure 15 illustrates the relationship between light absorption values (and distributions) versus different substrates, distinct by their contact angle with water.

The relationship observed is that quartz displays a low water contact angle (high surface energy) and results in a relatively high degree of inhomogeneity of coverage (error in Y-axis). The other two substrates are more hydrophilic and have a relatively lower variation of coverage. However, the water contact angle is not directly associated with the light absorbance, hence no direct causality between water contact angle and GO adsorption.
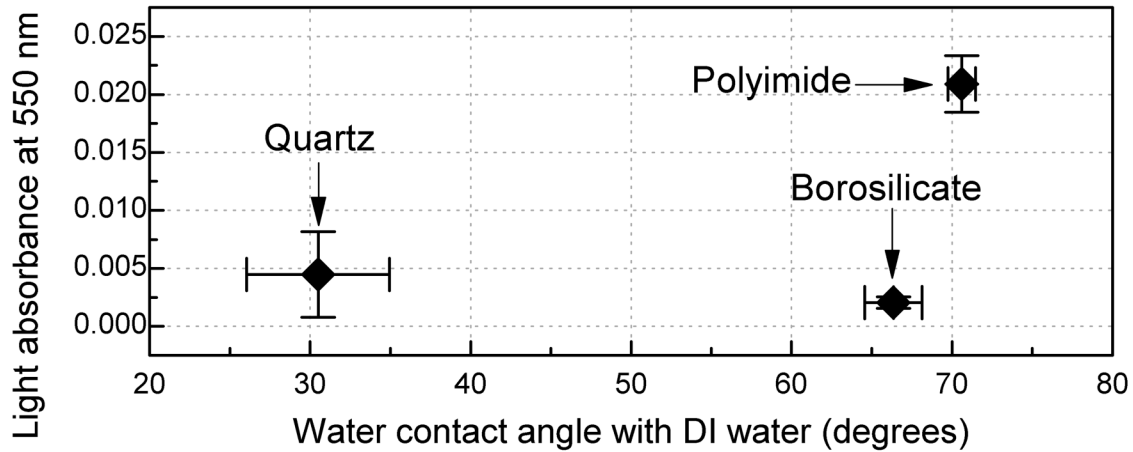
Figure 15 - Scatter plot of light absorbance of diverse substrates (as a result of GO dipping) versus water contact angle on the three bare substrates (indicated by arrows). (N≥ 7 for each sample). The distribution of values indicates that low water contact angle substrates (quartz samples) yield a low and vastly varied absorbance distributions as a result of dipping such substrate in GO. On the other hand, substrates with intrinsic high contact angle lead to more narrow distributions of light absorbance after they are dipped in GO.

Besides the absorbance measurements at 550 nm, also the light spectrum from 190 to 550 nm was acquired for the GO adsorbed on quartz. A typical result (Figure 16) shows features at 200, 235, and 300 nm. The shoulder observed at 300 nm is associated with the orbital transitions "n to π*" of the carbonyl groups, and the peak at 235 nm is manifested by the π- π* transitions of the C=C bonds[75,76]. As for the peak at ~200 nm, it is a transition related to supernatants of the commercial GO dispersion[46] (detailed in Figure 25). The light absorbance profile indicates successful adsorption of GO after step 2 process.
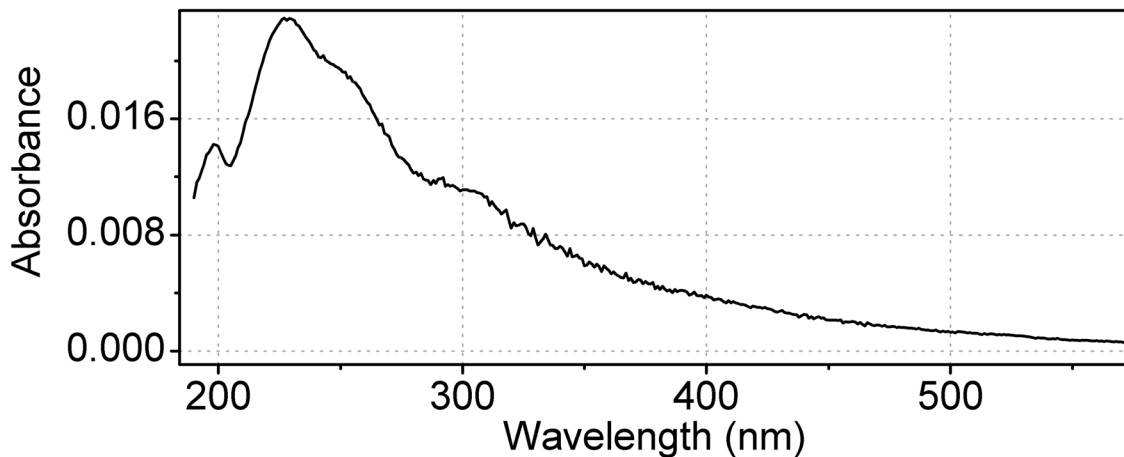
Figure 16 - Light absorbance for GO_1 coated on quartz substrate.

High resolution of C1s XPS measurement of the GO$_{nanocoating}$ result displayed in Figure 17. After taking into account the adventitious species on the surface of the substrate, it was found that the GO indicated a high degree of oxidation (also seen in[33,38,77–81]).
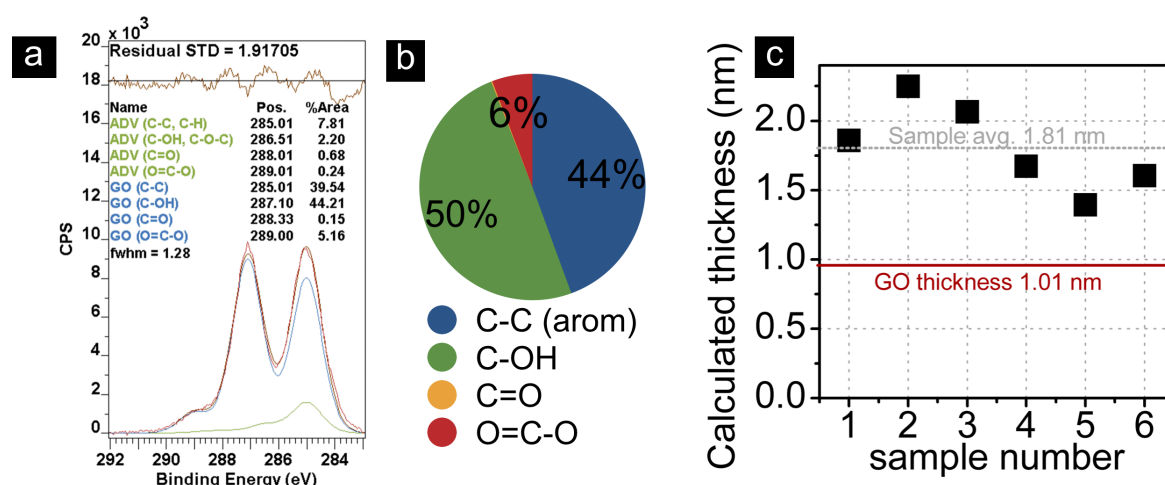
Figure 17 – XPS spectrum and homogeneity study. Extracted and adapted from Nanoscale, 2019,11, 4236-4247 - Published by The Royal Society of Chemistry. (a) C1s high resolution XPS spectrum of GO$_1$ with relative proportions of bonds represented in (b). (c) homogeneity study within one sample. Six measurements were conducted, and the thickness was calculated based on the substrate attenuation (detailed in Figure 18).

Besides the high-resolution spectra of 1-point measurement, another quartz substrate coated with (GO)$_1$ was measured in six points in order to measure the homogeneity of the coating (fast scanning, acquiring atomic concentrations). The resulting coating thicknesses are shown in Figure 17c. There is a relatively large variation among the six values, especially by considering that the evaluated area is 300 × 700 µm. As an average, the information indicates 1.8 nm of thickness, which corresponds to the thickness of almost two GO flakes. However, this technique has limitations, as it assumes homogeneous coverage.

AFM also confirmed the presence of graphene oxide flakes on a quartz substrate, as shown in Figure 18. The high degree of variation in terms of covered area (demonstrated in Figure 14) was also observed with AFM. Regions with typical 2D single GO flakes were observed (Figure 18c). The isolated flake in Figure 18c has a lateral size in the micrometer range, and the height to the substrate is 1.01 nm (evidenced in the histogram in Figure 18d). On the other hand, another sample (Figure 18a and b) showed a higher degree of coverage in the evaluated area. In Figure 18a it is possible to see an aggregation (center of the picture) laying on a relatively flat region (edges of the picture). This aggregation reaches over 10 nm of height (relative to the area around). Also, it is possible to draw more conclusions regarding the "flat region" on the edges of the picture. By evaluating the top-left corner of Figure 18a, highlighted with a green mark, one can see what appears to be two distinct continuous phases of materials. By evaluating the AFM-phase filter of the same region (Figure 18b), also green mark, the phase distinction is even more evident. Such distinction indicates the presence of two different phases, that is, a hard one (quartz substrate in darker tone) and a soft one (graphene oxide, lighter tones).
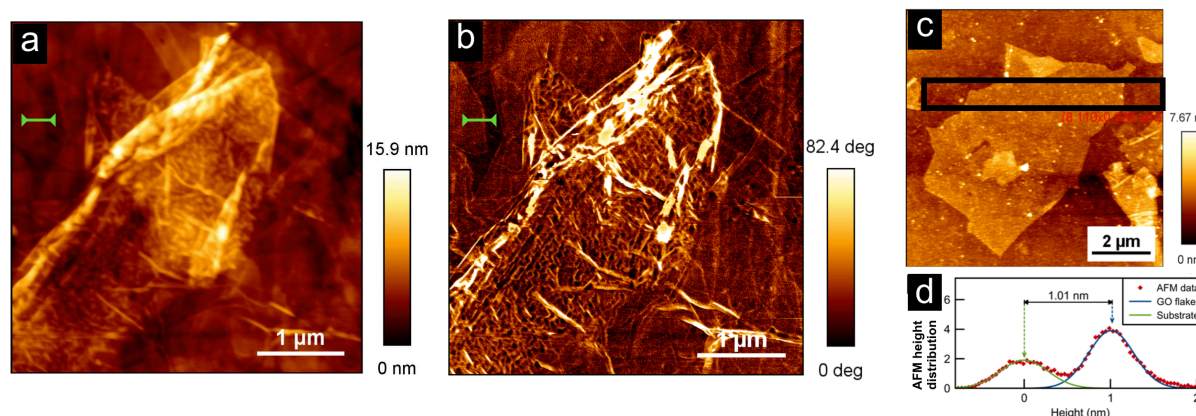
Figure 18 - AFM of (GO)₁ deposited on quartz. (a) AFM tapping mode revealing height information of a typical area on a typical film with higher coverage. (b) AFM phase mode of image (a), indicating the distinct mechanical properties within the coating (darker areas are likely the quartz substrate and lighter areas are likely the graphene oxide). The green marks in (a) and (b) highlight the distinct hard/soft phases. (c) AFM tapping mode height information of a (GO)₁ with lower coverage. (d) Height histogram information of area highlighted in (c), demonstrating the GO flake height of 1.01 nm. In (d), two Gaussians were fitted without any constraint. The resulting Gaussians widths indicate higher height homogeneity of GO than on quartz (sharper curve).

The three methods are complementary, as the areas investigated are in the nanometer- (AFM), micrometer- (XPS), and millimeter-scale (UV-Vis). In all methods, there was a significant degree of inhomogeneity of layer coverage. This indicates that GO assembles on the quartz substrate in multi-scale patched areas; including agglomerations in the few-micrometer scale (Figure 18a), continuous uncovered areas in the micrometer scale (Figure 18c) and overall less-covered areas in the micro- and millimeter-scale (Figure 14 and Figure 17c).

The spontaneous attachment of GO on substrates had been previously reported elsewhere.[48,66,82–84] Not only does GO adhere to diverse substrates, but it is possible to make films with overlapping flakes and controlled thickness, for example by changing the time[85] and number[48,66,82,86] of dipping coating, substrate functionalization[84,85] and temperature of the dipping process[66].

The experiments detailed in this subchapter confirmed the multi-substrate nature of graphene oxide attachment and also revealed the space inhomogeneity of applying "step 2" in the quartz substrate. These experiments are considered to be control experiments for the next subchapters, where a strategy for GO attachment is detailed.

2.2.1.2 Immobilization of bio-interfactants

The adsorption of two biological materials, denominated bio-interfactants[46], was investigated in this research (sketch represented in Figure 13b). The effect of dip coating substrates in a buffer solution containing such bio-interfactants (either BSA or LAC) was investigated with water contact angle, UV-Vis and XPS.

The substrates manifested some changes in surface wettability after the dip-coating in bio-interfactants. In Figure 19, control experiments support the evaluation of surface energy change after contact with each bio-interfactant. LAC reduced the contact angle of all substrates, but not significantly for quartz (which is already low). On the other hand, BSA transformed the quartz substrate to a more hydrophobic surface. It caused insignificant alteration in contact angle for borosilicate and reduced the hydrophobicity

of polyimide slightly. To a higher or lower degree, both bio-interfactants caused significant alterations to the substrates.
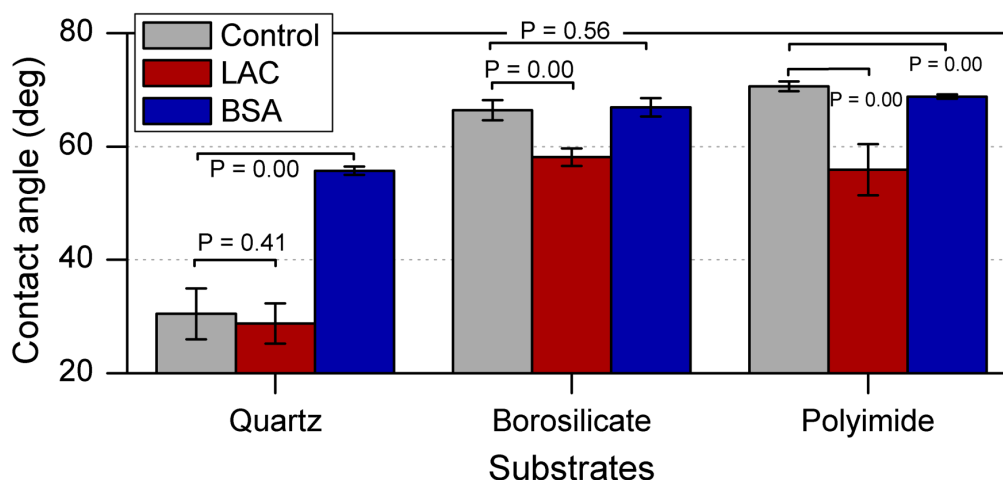
Figure 19 - Contact angle of water with diverse substrates (quartz, borosilicate and polyimide). Each substrate is measured in three conditions (control, after LAC adsorption and after BSA adsorption). P-values are indicated for each experiment (N=8).

UV-Vis light absorption of quartz with the bio-interfactants was measured, also showing absorption features from poly amino acids, particularly at ~195 nm[87,88] (results displayed in Figure 20). These samples demonstrate the difference in the overall shape of absorption of BSA and LAC. BSA shows a higher degree of light absorbance in the UV lights. Absorbance at 550 nm was close to zero for these adsorbates (inset in Figure 20).
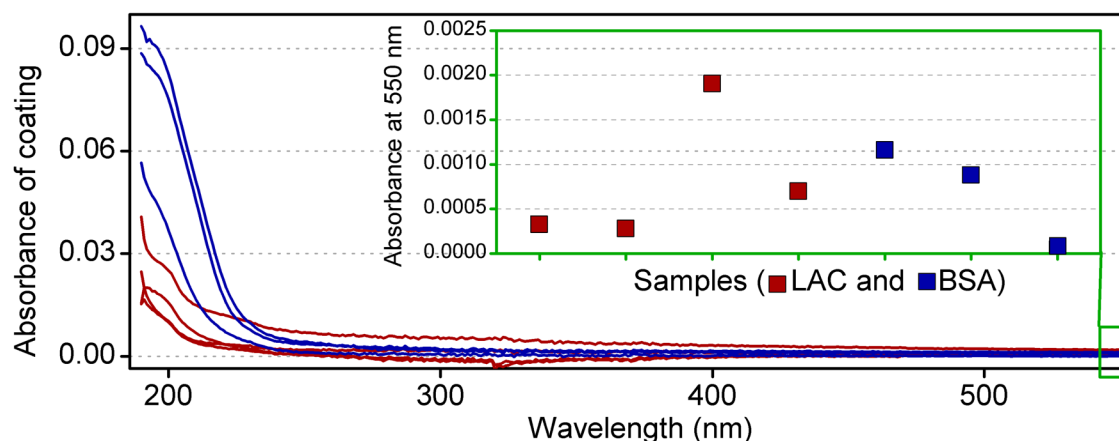
Figure 20 - UV-Vis spectroscopy of bio-interfactants adsorbed on quartz substrate. Absorbance values are calculated from the measured transmittance of each substrate before step 1 (as a reference).

XPS survey after "step 1" was conducted for the atomic species present on quartz substrates. The survey informed relative atomic concentration and also the signal from the substrate (Si2p). By evaluating the substrate attenuation after dip-coating, thickness could be calculated for both LAC and BSA (Figure 21a and b). The result is that LAC adsorbate is in the average 0.26 nm thick with a high standard deviation. In the case of BSA, the average is 2.01 nm with a standard deviation of 15% from the average. There are limitations to these thicknesses, as the calculation through signal attenuation assumes homogeneous thickness. However, it is possible to assert that the lateral distribution of the bio-interfactants deposited on the substrates differ

distinctly, even in the micrometer scale (XPS measures information in the spot size of ~450 μm in diameter). BSA adsorbs in thicker and more homogeneous (in the micrometer scale) layers than LAC.

The experiments of wettability are also connected to this result in Figure 19. LAC did not change the natural wettability of quartz substrate significantly, which is expected for a material that adsorbs poorly on a substrate. A relatively high degree of standard deviation is also in parallel with the observations in Figure 21a. On the other hand, BSA modifies the wettability of quartz and also maintains the standard deviation of that sample in a tight range. UV-Vis, which shows average information of a large ~2 mm area, substantiates that BSA adsorbs on quartz to a higher degree.
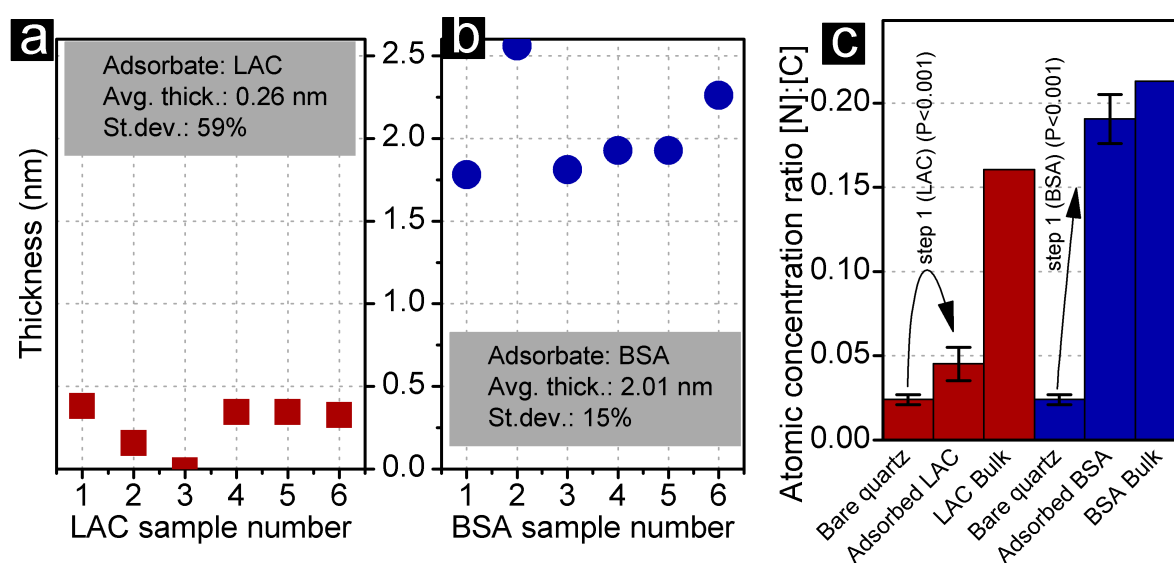
Figure 21 - (a) and (b) Thickness of LAC and BSA films, respectively, measured by Si2p XPS signal attenuation. Limitation to model should be considered since it assumes homogeneous layer coverage. In grey boxes in (a) and (b) further statistical information is provided. (c) Evolution of $[N]_{at}:[C]_{at}$ before and after step 1 for adsorption of LAC and BSA on quartz. Natively the quartz contains a low fraction of N:C ratio (0.025), which is substantially increased after step 1, indicating adsorption of the bio-interfactants LAC and BSA. The diminished increase of [N] for LAC adsorption is related to high adsorption of maltodextrin (free of nitrogen) that is present in the commercial mixture with Laccase from Trametes Versicolor. The ratio of the bio-interfactants (LAC and BSA) in bulk powder is also plotted as a reference (third and sixth columns). In (c) (N=14 for bare quartz and N=6 for adsorbed LAC and N=6 for adsorbed BSA). Image (c) adapted from Nanoscale, 2019,11, 4236-4247 - Published by The Royal Society of Chemistry.

Another way to check the adsorption of LAC and BSA was by evaluating the carbon to nitrogen ratio of the surface before and after the dip-coating (in Figure 21c). The quartz substrates are characterized by a small nitrogen/carbon concentration (resulting from contaminating agents on the atmosphere); however, LAC and BSA have a relatively high nitrogen/carbon atomic ratio (as amino acids build them). If these bio-interfactants are adsorbed on quartz, it is expected that the nitrogen/carbon ratio approaches that of their natural forms (since XPS depth information is ~10 nm). This is the result observed in Figure 21c, where the nitrogen proportion increases significantly when dip-coating occurs with bio-interfactants (step 1). The achieved proportions are also observed elsewhere.[89,90]

Homologous to all other results in this subchapter, BSA was the adsorbate that promoted the most significant change of quartz substrate. LAC also was observed to adsorb on quartz (but to a lower degree) and with inhomogeneous results. One must

consider that after the dip-coating, the substrates are embedded in DI water (pH 7), which probably desorbs these bio-interfactants to some extent. Otherwise, adsorption of these materials in multiple substrates have been observed elsewhere[87,89,91–100] and are typically studied for drug delivery, fundamental research, catalysis, sensors, calibration of devices, control experiments, biofuel cells and more.

2.2.2 Assembly of GO/bio-interfactant hybrid coatings

As discussed in previous subchapters, bio-interfactants and GO can spontaneously attach to diverse substrates. The next subchapters assess the intercalation between these materials (chapter 2.2.2.1). Then, thermal reductions of these systems are explored (chapter 2.2.2.2) and finally, in chapter 2.2.2.3, further experiments on the multiple intercalations of these systems are presented.

2.2.2.1 Immobilization of GO on bio-interfactants

Quartz substrates freshly functionalized with bio-interfactants (theme of chapter 2.2.1.2) were dipped in GO and compared to unfunctionalized quartz (control experiment chapter 2.2.1.1). The resulting properties were evaluated with multiple techniques.

First, optical properties were evaluated with UV-Vis (light absorbance at 550 nm). Figure 22 shows these results measured across several samples and in several areas. The non-functionalized quartz and the quartz treated with LAC dipped in GO dispersion (samples $(GO)_1$ and $(GO/LAC)_1$, respectively) resulted in absorbances near 0.005, and there is no significant statistical difference between them (P-value = 0.63). Substrates treated with BSA yielded superior GO adsorption when compared to control and LAC experiments. The higher light absorbance of samples with bio-interfactants is a result of GO adsorption, necessarily, and not from the bio-interfactants themselves[1].

---

[1] See the average of absorbance resulting from bio-interfactants (no GO) in dashed orange lines at the bottom of the second and third charts.
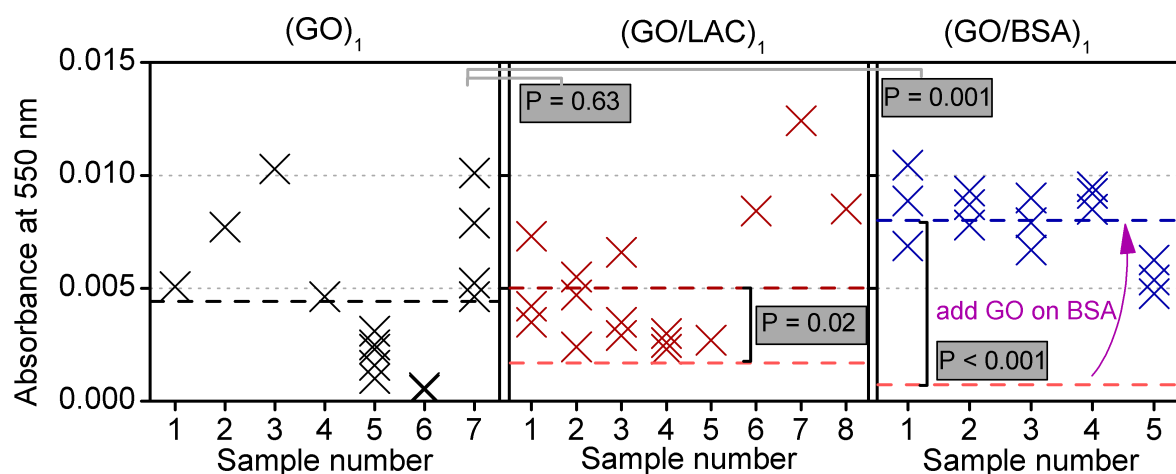
Figure 22 - Reproducibility of LBL systems evaluated using light absorption on several samples (coatings deposited on fused quartz). The (GO)$_1$ system showed low reproducibility among seven samples tested (average of values represented in bold dashed line just below absorbance 0.005). (GO/LAC)$_1$ display absorbance with scattered results, however no values close to zero (compared to GO$_1$). There is no significant statistical difference between adding and not adding LAC on the absorbance of coatings dipped on GO. On the second chart, the orange/pink dashed line at the bottom indicates the average of absorbance for LAC alone. (GO/BSA)$_1$ shows the lowest spread of values within and among samples. On the (GO/BSA)$_1$ chart, the orange/pink dashed line at the bottom indicates the average of absorbance for BSA alone (after step 1).

As for the broad absorbance spectra, typical[1] samples show how the absorbance is changed for each step of the process, after "step 1" (red curves) and next after "step 2". The light absorbance of (GO/LAC)$_1$ (in green, Figure 23b) is relatively similar to the control experiment (Figure 23a) (GO)$_1$: both curves possess similar shapes and intensities. However, there is a distinct selection of the attached GO. The insets of the charts in Figure 23 indicate the contribution of the GO to the absorbance profile, and among (GO)$_1$ and (GO/LAC)$_1$ there is a clear shape distinction. At ~200 nm there is a prominent peak on the GO adsorbed without bio-interfactants aid (blue arrow in inset charts). As for the bio-interfactants, LAC selects GO that manifests such peak mildly (Figure 23c inset), and BSA selects GO with such peak at the lowest degree (Figure 23c). More details on this peak is explored in experiments described later and illustrated in Figure 25).

---

[1] Meaning the samples in which the absorbance spectra were nearest to the average of absorbance among several samples.
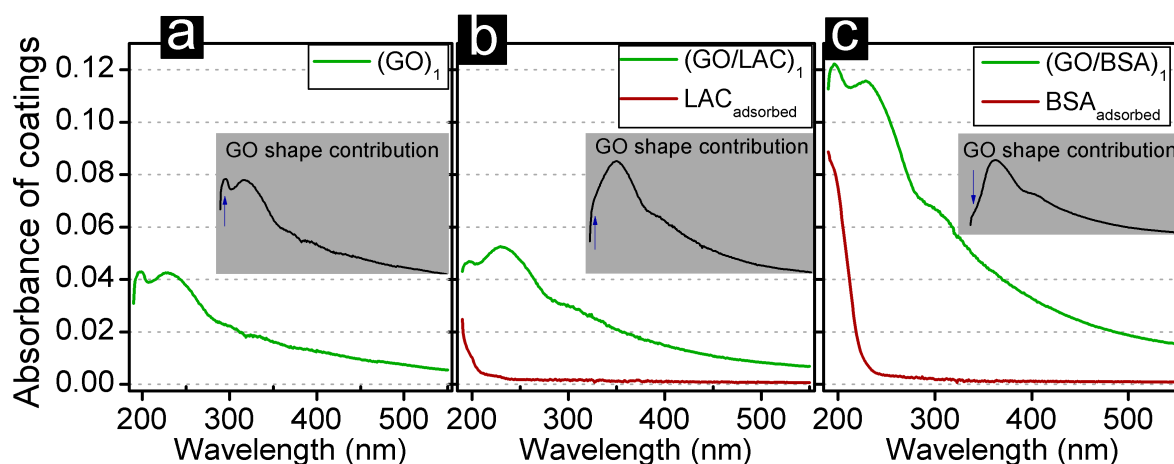
Figure 23 - Absorbance spectra of coatings relative to their individual quartz references. From 190 to 550 nm.

The overall absorbances of the coatings in Figure 23 (green curves, from 190 to 550 nm) are well related to the absorbance values at 550 nm, in other words, the spectra have similar shapes, and the total intensity is proportional to the absorbance observed at 550 nm. The material $(GO/BSA)_1$ showed an overall spectrum roughly 2.5 times higher than $(GO)_1$ and $(GO/LAC)_1$, which relates to having more GO deposited.

Next, XPS survey was conducted on the three coatings systems. Two types of investigations were done with XPS; (i) substrate signal attenuation and (ii) high resolution of C1s signal. Unfortunately, for test (i) the samples were not selected on the base of being "typical" [1] and after later inspection it was found that the coating $(GO/LAC)_1$ was abnormally high in light absorbance. The other samples, on the other hand, were found to be representatives of the processes $(GO)_1$ and $(GO/BSA)_1$. Also, representative samples were used in the set of experiments (ii).
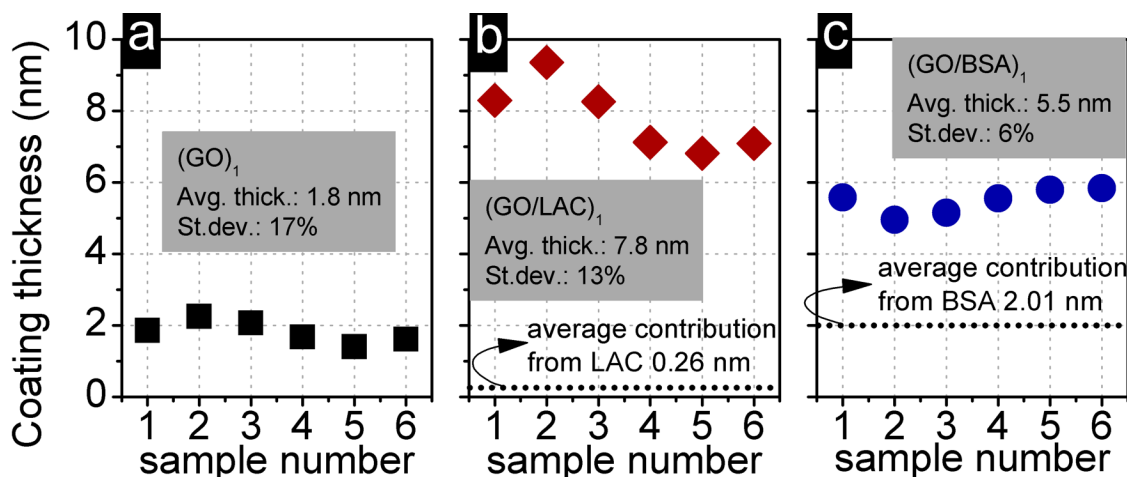
Figure 24 - Calculated thickness of coating using XPS signal attenuation from the substrate (Si2p).

---

[1] Meaning that the sample was not chosen with previous care that it had an absorbance spectrum near the average of absorbance spectra of several samples. For samples with LAC this can be critical, as high degree of inhomogeneity was observed when using such bio-interfactant.

The signal attenuation allows for layer thickness calculation, and such values are plotted in Figure 24. The thickness values form GO_1, which is the control experiment without bio-interfactants, results in 1.8 nm thick coatings, with a high degree of thickness variation. The coatings produced using assistance from LAC and BSA yielded thicker samples, as represented by red and blue symbols. All coatings are ultra-thin[1] (<10 nm) and the coating with BSA has a higher homogeneity among the points investigated.

The starting thickness contribution from the interfactants[2] (dotted black lines in Figure 24b and c) has an interesting effect on the overall thickness: For $(GO/BSA)_1$ it appears that the 2 nm layer of BSA attracts between 3 and 4 layers of GO. A reservation must be stated for the general interpretation of $(GO/LAC)_1$, as it is not a typical sample. Nevertheless, the final material originated from the sequence of step 1 followed by step 2. A possible interpretation is that in this particular sample more LAC than usual was adsorbed[3] prior to the GO dipping. Then, during the GO dipping the weakly adsorbed LAC could have desorbed[101] and interacted with the GO particles near the surface. The interaction could have formed a complex (since LAC and GO are charged oppositely in step 2) and then reabsorbed in higher amounts resulting in this particular sample[4].

Detailed chemical information on $(GO/BSA)_1$ was further assessed by high-resolution analysis of the C1s signals (and compared to the control experiment, $(GO)_1$, and slightly changed experiment $(upGO/BSA)_1$). The resulting spectra (Figure 25a-c) were fitted with the species expected to be on the substrate. Adventitious carbon profile was measured previously and added to the plot (in green). BSA C1s profile respected the ratios published elsewhere[102], and the total intensity was not constrained. The peak components of GO were constrained to a range broadly accepted on the literature[33,34,65,103–108] and fitted to minimize the total fitting error. The resulting intensities of peaks are displayed in text inside each spectrum. The residual error is plotted on the top of the spectra.

The resulting GO subcomponents are presented in pie-charts in Figure 25e-g. By comparing $(GO/BSA)_1$ with the control experiment $(GO)_1$ in terms of the adsorbed GO (Figure 25e and f), it is clear that there is a distinct selection of GO (evidenced by the two highest peaks and their proportions in images a and b). When BSA is previously adsorbed on the substrate, it results in the selection of less oxidized graphene, possibly with more aromatic rings. Since BSA does not possess such peak at 287 eV,

---

[1] Assuming homogeneous coverage, as discussed in materials and methods.

[2] Results presented in Figure 21

[3] Possibly because the rinsing process of step 1 was not strong enough. One example of higher LAC adsorption is observed among the LAC adsorption samples in Figure 20 (highest red curve).

[4] This interpretation is probably incomplete. However, the experiment opened ideas discussed in the last chapter for future experiments. This hypothesis of forming a "LAC-GO complex" could be substantiated also because GO-GO interactions tend to be repulsive[82].

it can be concluded that the contribution does not arise from BSA, but from GO interaction with BSA.

The spectrum in Figure 25c results from a slight modification in the process $(GO/BSA)_1$. This alternative protocol used GO present in the supernatant liquid after centrifuging the standard GO dispersion (see Figure 25d inset). Such supernatant is here named "upGO". The coating resulting from this procedure is named $(upGO/BSA)_1$ and its XPS spectrum is presented in Figure 25c. Comparing to the standard coating $(GO/BSA)_1$, the collected GO in the upGO supernatant is more oxidized (Figure 25g), and also substantially more GO is adsorbed when exposed to upGO supernatant.
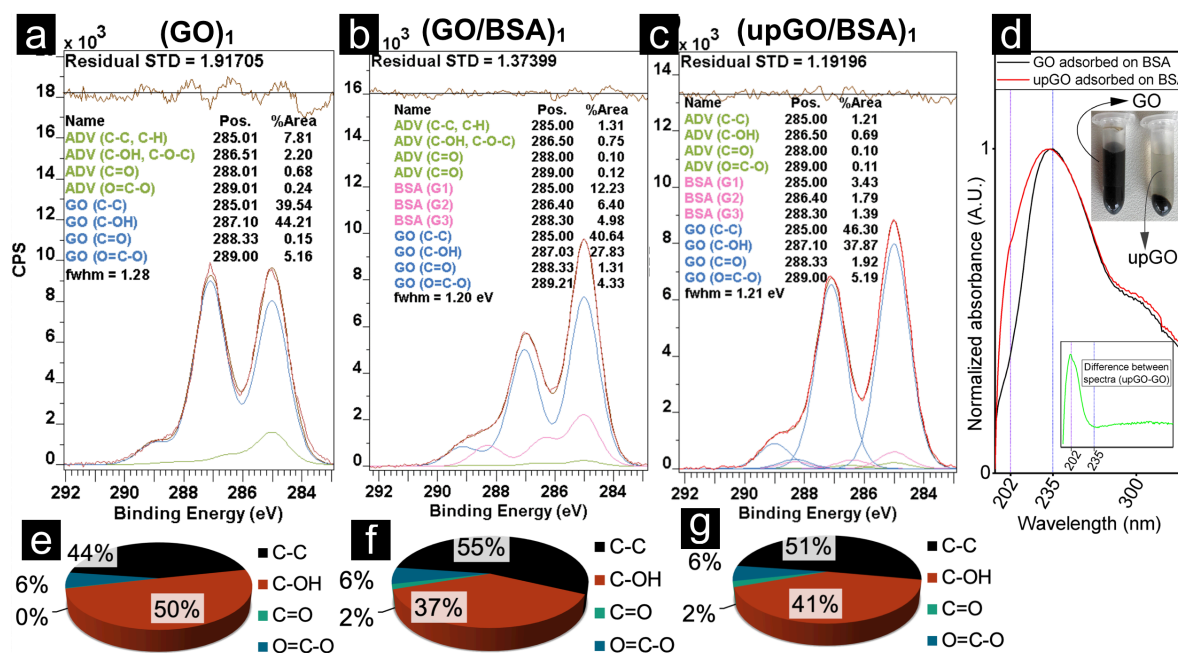
Figure 25 – Images adapted from Nanoscale, 2019,11, 4236-4247 - Published by The Royal Society of Chemistry. (a to c) C1s high resolution spectra of coatings $(GO)_1$, $(GO/BSA)_1$ and $(upGO/BSA)_1$. (e to g) corresponding GO chemical groups in the coatings $(GO)_1$, $(GO/BSA)_1$ and $(upGO/BSA)_1$. (d) Distinction between GO and upGO. Both materials arise from the same commercial GO dispersion, however "upGO" is the supernatant from a centrifuge of the commercial product (see inset picture). In terms of light absorbance, upGO manifests a peak at 202 nm, detailed in inset picture (green spectrum).

The experiments with the supernatant upGO shed light on conclusions from Figure 23a and c. By measuring the light absorbance of coatings $(GO/BSA)_1$ and $(upGO/BSA)_1$, it is clear that $(upGO/BSA)_1$ has a significant peak contribution at ~200nm (inset with green spectrum in Figure 25d). Such peak was found to be associated with highly oxidized GO and/or debris, present in higher concentration in the supernatant[109,110] fraction upGO. And since the bare quartz adsorbed GO flakes with this peak (Figure 23a), it is possible to assert that the oxidized debris have high attraction towards quartz substrate. On the other hand, such oxidized GO debris are not preferentially attached on BSA (comparing Figure 25f with Figure 25g).

To complete the characterizations, AFM was employed to observe the deposition of GO (step 2) on samples with and without bio-interfactant functionalization (depicted in Figure 26). Images a to c indicate the relatively flat topography of the GO coatings, with heights and valleys within 10 nm of vertical distance apart. Images d to e are AFM-phase mode filter, which indicates the mechanical properties of materials. In such images it is possible to observe two-phase distinction on coatings $(GO)_1$ and

(GO/LAC)$_1$: The darker regions in images d and e are likely uncovered areas revealing the hard quartz substrate and the lighter tones are likely the soft GO flakes. Figure 26f shows a typical (GO/BSA)$_1$ coating evaluated with the AFM-phase mode where no double phase distinction was observed[1]. Such information goes in the direction of the other experiments in this subchapter, indicating high coverage and homogeneity of (GO/BSA)$_1$. The observation of gaps on GO coatings unassisted by bio-interfactants was also reported elsewhere.[48,82]
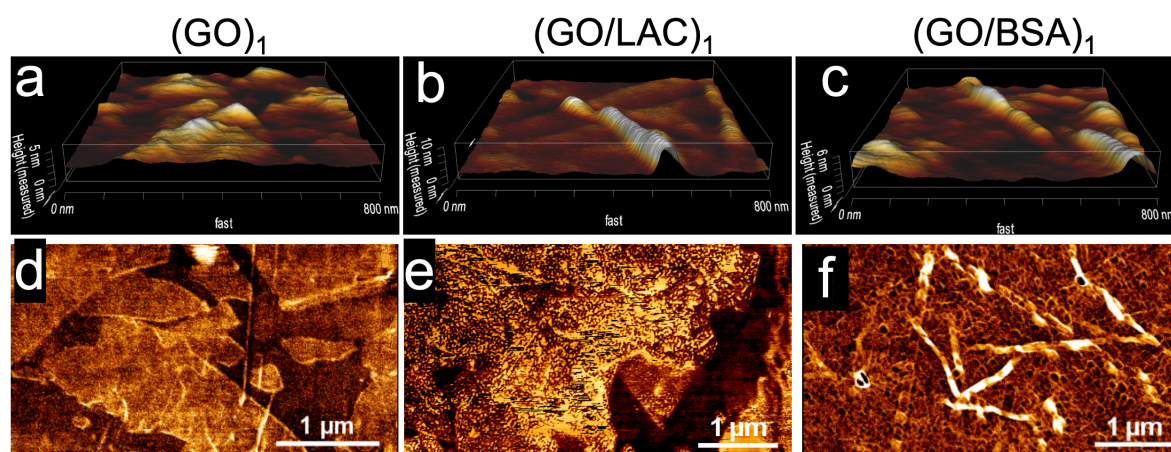
Figure 26 - Images adapted from Perez et al [46] (Nanoscale, 2019,11, 4236-4247 - Published by The Royal Society of Chemistry). (a-c) Microstructure of the three investigated coatings (GO)$_1$, (GO/LAC)$_1$ and (GO/BSA)$_1$, respectively. (d-f) Selected AFM phase images of (GO)$_1$ and (GO/LAC)$_1$ and (GO/BSA)$_1$ respectively reduced at 180 °C; on (GO)$_1$ and (GO/LAC)$_1$ it was observed a high contrast of regions (illustrated in images (d) and (e)), which were linked to quartz substrate (hard phase), such contrasting phases were not observed in coatings with BSA, illustrated by (f). Regarding (GO/BSA)$_1$, no AFM image was found to have the distinct 2-phase characteristic upon inspection of total 23 positions on five individual samples which included the four investigated temperatures, indicating high coverage of substrate independent of temperature of reduction when using BSA as bio-interfactant.

A further AFM image from a (GO/LAC)$_1$ coating was captured in high-resolution and high-area in order to further study the topographic features influenced by GO flakes. As shown in Figure 18d, a GO flake is in the average 1.01 nm above[2] the substrate; the same histogram procedure was conducted with (GO/LAC)$_1$. The AFM of the large area (Figure 27a) was scanned in its central part (Figure 27b), which was evaluated in terms of height frequency (Figure 27c). The histogram was fitted with three Gaussians (free of constraints), and the model had a good fit. The interpretation of this result is that the topography of this sample has three levels, the lowest to the middle are separated by 0.88 nm, and the middle to the highest one separated by 1.18 nm. Possibly the shorter distance gap is associated with stronger interaction (short range forces) between flakes and the substrate. The last layer, being 1.18 nm from the previous one indicates weaker GO-GO interaction[82]. The width of these gaussians is ~ 0.5 nm and the width of the Gaussian for a GO flake is ~0.3 nm (Figure 18d). The

---

[1] In the total, 23 distinct positions were evaluated within five individual samples, totaling ~90 µm^2. (GO)$_1$ and (GO/BSA)$_1$ were evaluated for "hard" phases in over 63 µm^2 and showed 6% and 11% of such areas (assumed to be the substrate quartz).

[2] Comparing the outermost surface, detected by the AFM.

broader width of heights on $(GO/LAC)_1$ is probably the result of accumulated unevenness far from the flat quartz substrate.
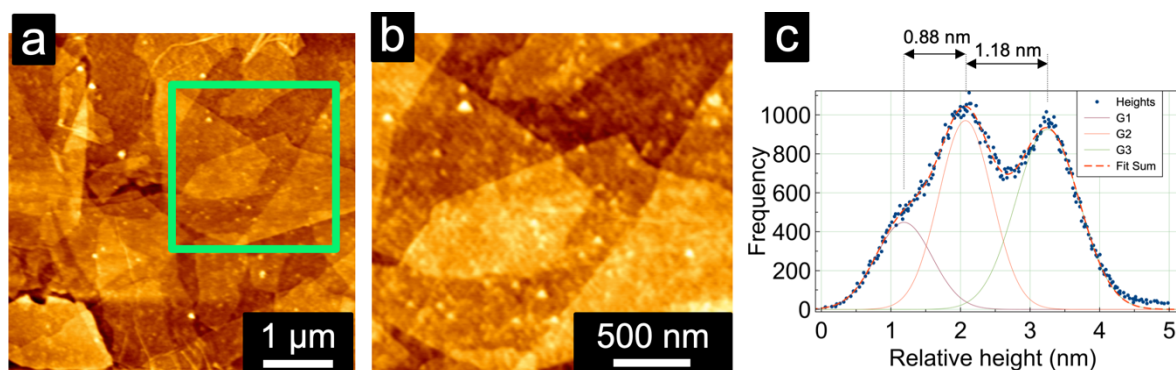
Figure 27 - (a) AFM of $(GO/LAC)_1$ and (b) magnified part of (a, highlighted in green). (c) height histogram from image (b), including three gaussian curves fitting the data with accuracy. The X distance between the gaussians roughly characterize the height of a GO flake (~1 nm). The similar width of the gaussians characterize similar topographic features between the three surfaces heights. The three gaussians were fit disregarded of any constrains, just minimizing the total error.

AFM height histogram evaluation was also conducted on $(GO/BSA)_1$ (Figure 28), however, the model described above (with deconvoluted Gaussians) could not be implemented.
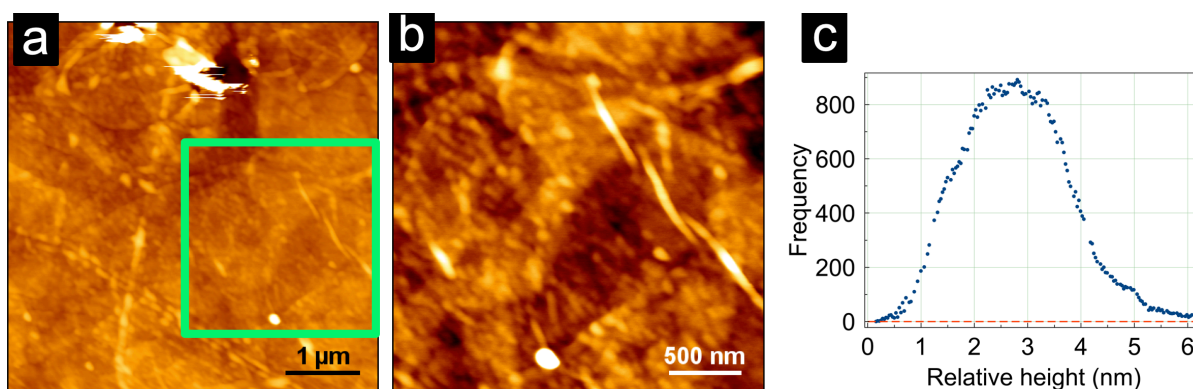
Figure 28 - (a) AFM of $(GO/BSA)_1$. (b) magnified part of (a, highlighted in green). (c) Height histogram from image (b). This image could not be deconvoluted using the procedure in Figure 27 and Figure 18.

The results presented above are from experiments conducted in the laboratory and assessed by characterizations on multiple scales, from millimeter average information (UV-Vis) to nanometric features (AFM). Yet, the experiments were also evaluated with molecular dynamics (detailed in Perez *et al.*[46]).

In the published work[46], it was found that the amino acid residues play a key role in the anchoring towards the substrate and later priming the surface to interact with GO. The dipole direction of LAC drives it to orient itself towards the negatively charged silica surface. The other bio-interfactant, BSA, attaches on quartz driven by hydrophobic residues, leaving the side with more hydrophilic groups facing outwards; but still being strongly attached on the substrate.[111]

These behaviors result in LAC and BSA being attached in preferential orientation on silica, leaving a particular group of amino acids exposed to outside of the substrate's surface. The affinity of amino acids towards GO and silica have been measured[52,111],

resulting in arginine, lysine and histidine having the highest adsorption forces, to both GO and quartz. These three amino acids compose ~10% of the solvent-accessible surface area of both in bio-interfactants[46]. However, such groups are spread differently in Laccase and BSA (Figure 29).
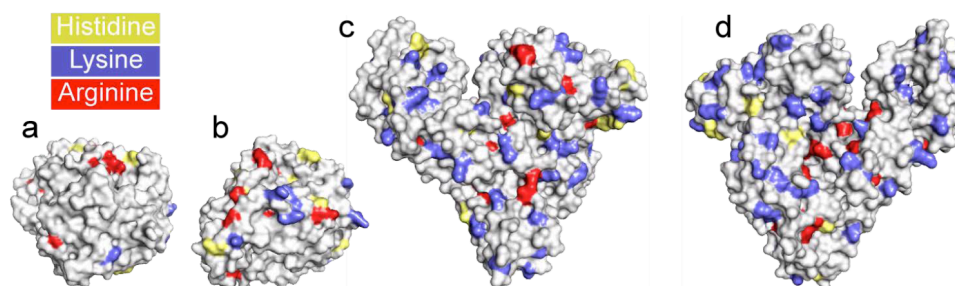
Figure 29 - Extracted from Nanoscale, 2019,11, 4236-4247 - Published by The Royal Society of Chemistry. Representation of polypeptide models; (a) and (b) are opposite sides of Laccase (PDB code:1GYC). (c) and (d) are two sides of BSA molecule (PDB code: 3V03). Key amino acids are highlighted with different colors. BSA displays more homogeneous distribution of these sites comparing to Laccase.

On BSA all the three anchoring sites (highlighted in yellow, purple and red) are well spread around the molecule.[95,112] On Laccase, however, one side is vastly more concentrated in such amino acids (highlighted colors in a compared to b in Figure 29). This uneven amino acid distribution in LAC leads to a binary condition; either the strong attachment sites are mostly facing GO or the substrate, but not both simultaneously. When BSA is used, it faces both quartz and GO with strong anchoring sites.[46] An illustrative analogy is that LAC works as scotch tape between a desk and a paper sheet, whereas BSA works like a double-sided tape between a desk and a paper sheet. In the case of LAC, the scotch tape is well attached to only one of the flat materials.

Furthermore, in the experiment depicted in Figure 19, it was demonstrated that BSA transforms quartz towards a more hydrophobic surface. This allows yet another possibility of interaction between BSA and GO: hydrophobic interactions[113,114]. This idea is strongly substantiated with Figure 25, where it was demonstrated with XPS that BSA selects GO flakes that have less oxygenated groups (hence probably more aromatic rings, which are hydrophobic).

As a summary, a simplified model is proposed for the formation of (GO/BSA)$_1$ (Figure 30). In the first stage (step 1), the system is embedded in a buffer solution with pH 4.75. At such pH, the silica substrate is negatively charged, and the BSA molecules are positively charged. The opposite charges are the main[1] driver for adsorption. Next, in step 2, the BSA-on-silica system is embedded in a lower pH media in the presence of GO. At such pH, the substrate materials are expected to be positively charged[111,115], and the GO is negatively charged[116]. Once again, the system favors attraction of the natant particle towards the substrate.

---

[1] However, a significant contribution stems from hydrophobic interactions at such pH.[111]
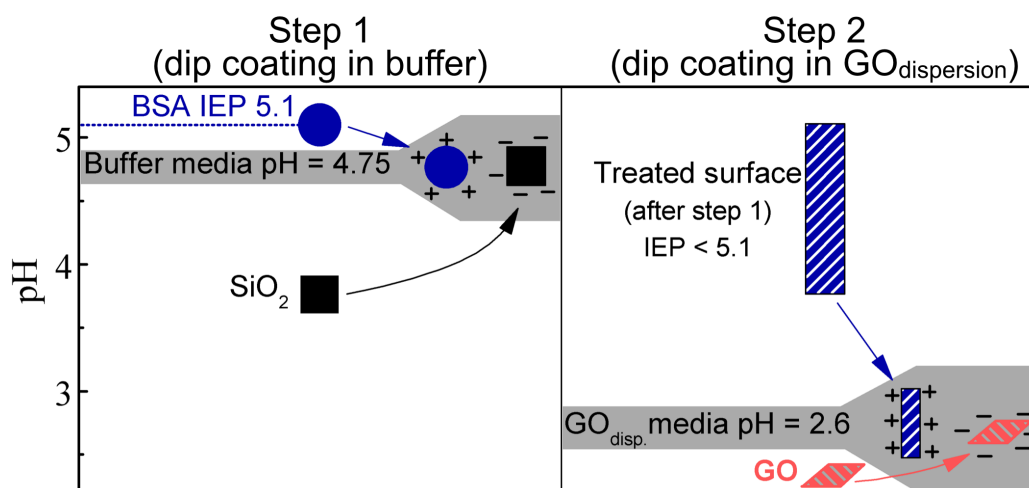
Figure 30 - Schematic model for the formation of (GO/BSA)₁. The first step exposes BSA (in liquid buffer) to a pH lower than its isoelectric point. At such pH, BSA is positively charged and the substrate is negatively charged, causing a positive diving force between them. On step 2, a similar strategy is employed: the pH of the media allows the substrate and GO to have opposite net charges, hence a positive driving force.

The process was designed in a way to optimize BSA adsorption at the right pH and allow such particle to be kept adsorbed even at low pH during step 2. If step 2 was merely an acidic (pH ~2.6) solution without GO, BSA would have probably desorbed slowly over time[117,118], but GO entered the system and stabilized the adsorbed BSA by assembling itself on top of it.

2.2.2.2 Thermal reduction of GO_{bio-nanocoatings}

As discussed in chapter 1.2.3, GO is used as a key precursor for graphene. Several techniques can be used to achieve graphene-like properties. In this subchapter, only reduction through low temperature is reported (referred as "step 3", reaching 250°C). The chemical, electrical, optical, and structural properties that ensued from thermal treatment are characterized by XPS, multimeter, UV-Vis and AFM.

The before/after UV-Vis absorbance spectroscopy of coatings is represented in Figure 31. Coatings "before reduction" are represented in green and "after reduction" in blue. All coatings manifested a peak transition from ~230 nm to ~270 nm as a result of the thermal reduction. This transition corresponds to the restoring of the electronic conjugation of graphene[119]. The shoulders at ~300 nm apparent in the unreduced curves are related to C=O[1] bonds[120–122], which vanishes after the thermal reduction (indicating deoxygenation). The sharp peak at ~200 nm (explored in Figure 25d) was only slightly altered with the reduction (to lower values).

Among the three coatings, the ones with bio-interfactants resulted in higher overall absorbance, and the coating with BSA absorbed more than double of light (at 550 nm) when compared to the use of LAC.

---

[1] Referent to n to π* electronic states.
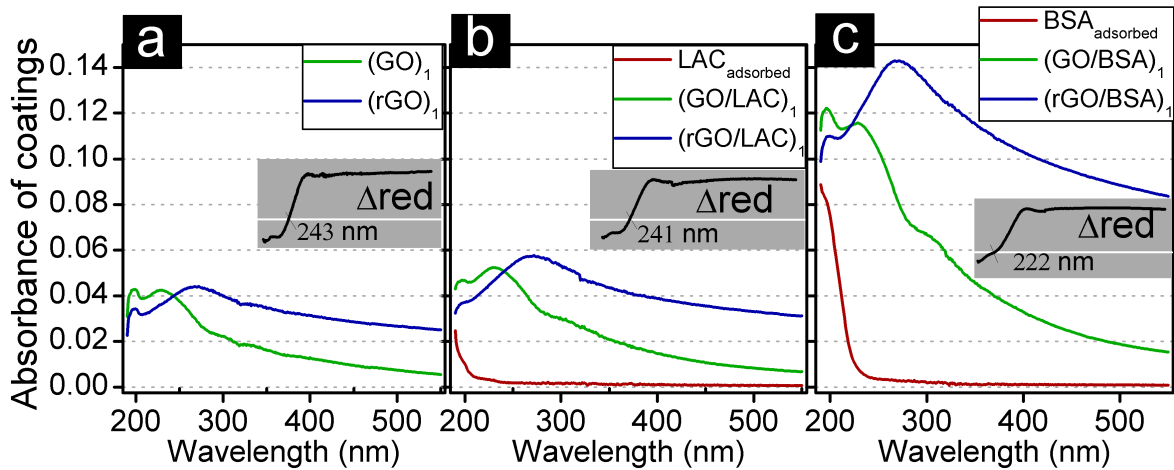
Figure 31 – UV-Vis spectra of freshly produced (green curves) and thermally reduced (blue curves) coatings: control experiment (a), with LAC (b), and with BSA (c). Red curves on (b) and (c) show the spectra of bio interfactants (prior to GO adsorption). Inset pictures indicate spectra change resulting from the thermal reduction process. In the inset pictures, the white horizontal lines indicate Y = 0 and the numbers indicate the wavelength absorbance not affected by the thermal reduction.

The change in light absorbance can be viewed in relative terms, too. The charts plotted in grey insets on Figure 31 show the relative contribution in light absorbance that is caused by the thermal reduction (blue minus green spectrum). By evaluating these curves, it is clear that thermal reduction causes a general increase in light absorbance in most of the spectrum (Y=0 in white). However, towards low UV-wavelengths there is a transition making light absorbance lower and even negative (meaning that in such wavelength, the sample becomes more transparent). This beginning and intensity of this transition were precisely characterized by differentiating the inset pictures of Figure 31. As supported by the literature[119,123,124], the shift from 230 to 270 nm reveals information about the chemical groups of graphene oxide.
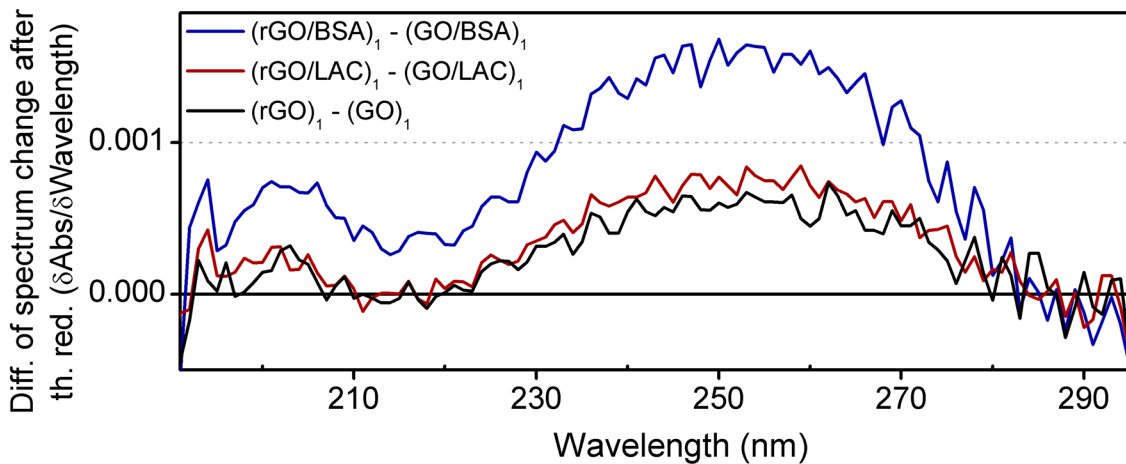
Figure 32 - Differentiation of the curves associated with the thermal reduction effect. The differentiated data (from inset pictures of Figure 31) indicate change in curve position at any given wavelength. At 220 nm the absorbance resulting from the thermal reduction of (GO/BSA)₁ is already positive; meaning that the red-shift transition of this sample initiates in earlier stages than the two other coatings.

The result, in Figure 32, shows that the reduction of (GO/BSA)$_1$ shifts the peak to the right (red-shift) earlier and more intensely than the other two coatings[1]. Since this shifting is observed in the exact ranges of reduction towards graphene[119,123,124], it is possible to substantiate that the thermal reduction with BSA leads to a higher reduction of the GO (compared to control and LAC experiments).

As a control experiment, the bio-interfactants were thermally reduced when adsorbed on the quartz substrate (no GO was added). The result (Figure 33) shows minimal change in the absorbance spectrum (plotted in LOG to accentuate). Other studies support the high thermal stability of these adsorbates[125–128].
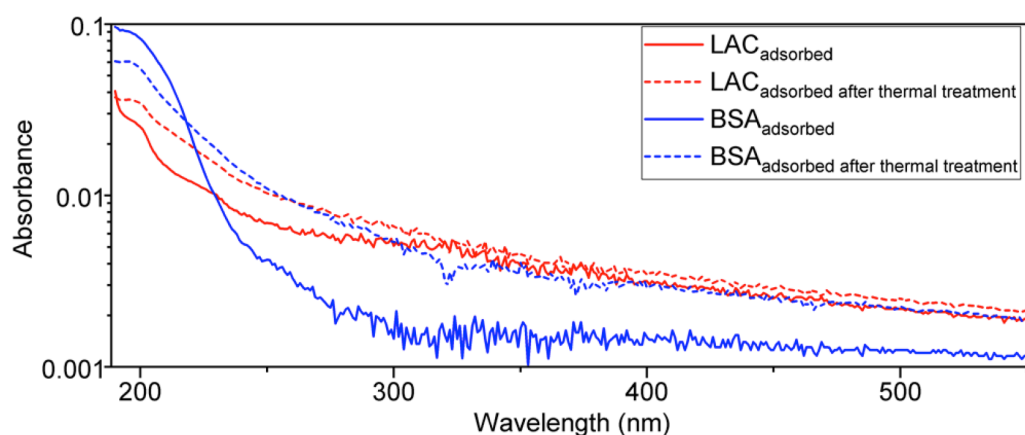
Figure 33 – Extracted from Nanoscale, 2019,11, 4236-4247 - Published by The Royal Society of Chemistry. UV-Vis of thermal reduction of adsorbed BSA and LAC. Control experiment indicated minimal changes in absorbance spectra, at the same time demonstrated that the biological materials are still in some form on the quartz substrate (not removed by the thermal reduction).

High resolution of C1s XPS spectra of the reduced coatings was conducted and is depicted in Figure 34. The thermal reduction of (GO)$_1$ towards (rGO)$_1$ results in a sharp and asymmetric component with a peak ~185 eV. Such transition characterizes the thermal reduction of GO where removal of oxygen (vanish of peaks > 285 eV) and restoration of sp^2 sites occurs, even at 250°C.[30,105,129] The coating with bio-interfactants were deconvoluted to account for the bio-interfactants, contamination, and GO. The final proportion associated with the GO is shown in Figure 34e-h. Judging by the proportions, there was a chemical reduction of the GO, however in a lower degree than compared to GO in (rGO)$_1$. Among (rGO/BSA)$_1$ and (rGO/LAC)$_1$, it was the use of BSA that resulted in higher conversion of GO towards graphene (higher proportion of the aromatic component at 285 eV).

---

[1] Consider that positive "hills" in differentiated curves represent an "s curve" in real data. In Figure 32 at 220 nm, the blue curve is already positive, meaning that the curve shift started earlier than the other two curves.
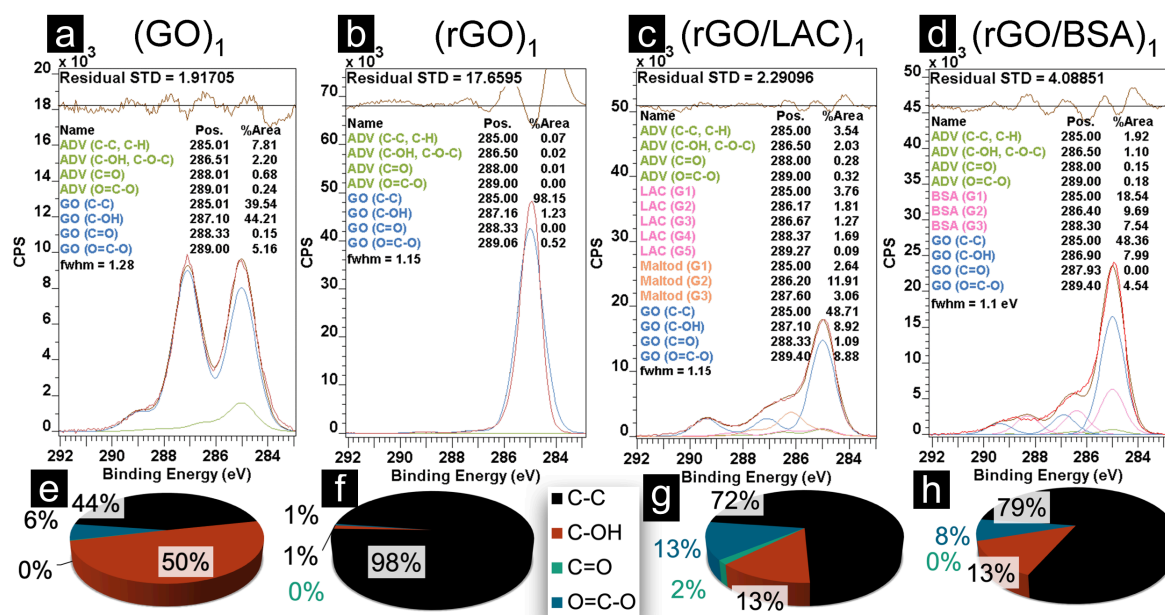
Figure 34 - Extracted and adapted from Nanoscale, 2019,11, 4236-4247 - Published by The Royal Society of Chemistry. C1s high resolution XPS spectra of (from left to right) $(GO)_1$, $(rGO)_1$, $(rGO/LAC)_1$ and $(rGO/BSA)_1$. The first spectrum is the only one with the high peak ~2 eV higher than the reference peak at 285 eV, which is a feature of highly oxidized GO[38]. The reduced forms of the three coatings; $(rGO)_1$, $(rGO/LAC)_1$ and $(rGO/BSA)_1$ show the peak at ~287eV with a substantially low contribution to the spectra. Green area is attributed to adventitious carbon from the quartz substrate, which was corrected by Si 2p attenuation. Spectra from $(rGO)_1$ is a region unusually thick, which stems from the low reproducibility of the process when unassisted by bio-interfactants.

Furthermore, in this series of experiments on thermally reduced coatings, XPS was also employed in order to measure the atomic composition of the coating and the coating thickness. This series of experiments was conducted with two other intermediate temperatures for more in-depth clarifications.

The atomic composition of these coatings in several temperatures is displayed in Figure 35. In $(GO)_1$, nitrogen is expected to be only residual and remains in low values for all the temperatures. The samples did not have a continuous trend for carbon and oxygen concentrations. This is probably related to the low coverage and unreliability of the process (as discusses previously along with results in Figure 22 and Figure 26). Samples with bio-interfactants, Figure 35b and c, showed a general increase of carbon and decrease of oxygen and nitrogen, but in an interesting fashion; as Figure 35d portrays, the proportion between carbon and nitrogen remains constant for $(GO/BSA)_1$ in all temperatures, but for $(GO/LAC)_1$ there is a sudden increase in the proportion when the coating is exposed to 250°C.

The carbon to oxygen proportions in coatings with bio-interfactants (Figure 36b) reveal that the starting proportion is the same (C:O ~ 3:1), but after thermal reduction, the proportion is increased for $(GO/BSA)_1$, which means that more oxygen than carbon is removed when a coating uses BSA instead of LAC.
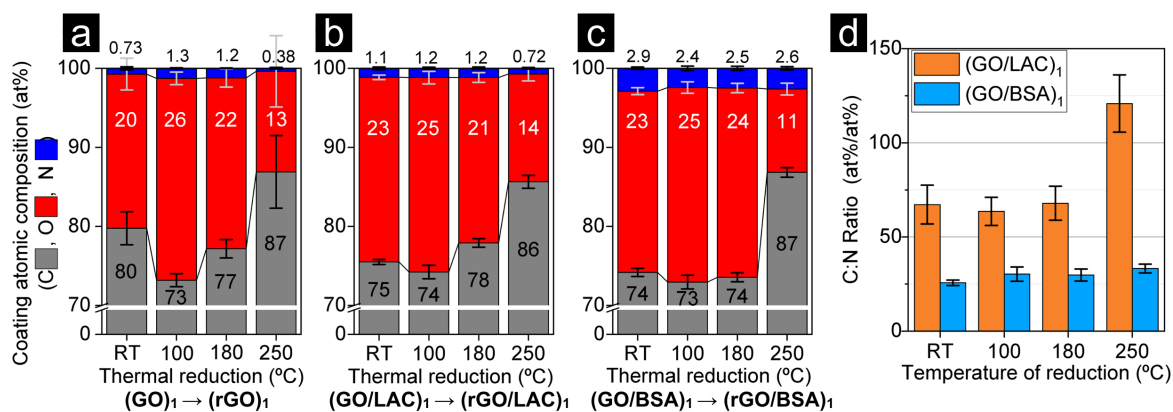
Figure 35 - Extracted and adapted from Nanoscale, 2019,11, 4236-4247 - Published by The Royal Society of Chemistry. (a–c) XPS elemental analysis of layer composition (substrate content is subtracted) for four conditions of thermal reduction for the layer systems: (a) $(GO)_1$, (b) $(GO/LAC)_1$ and (c) $(GO/BSA)_1$. The relative composition shows only the additional C, N, and O elements added to the quartz substrate. $(GO)_1$ was found to contain 0.75% atomic of N, which is attributed to be residual nitrogen expected to be found from Hummers process[79,130] (d) atomic concentration ratio [C]:[N] in the coatings (from (a–b)) with bio-interfactants $(GO/LAC)_1$ and $(GO/BSA)_1$ for all conditioning temperatures

Since in $(GO/BSA)_1$ most of the nitrogen of the system belongs to BSA[46] and most of the carbon belongs to GO, it is probably the case that the fixed [N]:[C] proportion is explained by the anchoring effect that BSA has on GO (also supported on previous experiments and molecular dynamics). In the case of LAC, an independent reduction between the species is observed, facilitating more the removal of LAC (because C:N is increased, and N is a marker for LAC).

With the atomic concentrations (now including atoms from the substrate), the thicknesses of the coatings[1] could also be calculated. As plotted in Figure 36a, the coating with BSA displays constant range between 5 and 6 nm at all 4 temperature conditions. For coatings starting with $(GO/LAC)_1$, it appears that the temperature has an effect on material removal until 180°C. However, there are limitations to the experiment with LAC, since it was conducted on samples which were not necessarily representative in terms of thickness (estimated by the average light absorbance). Such a lack of reference measurement later proved to be critical since the process reliability is not high (demonstrated in Figure 22 and also manifested in Figure 24b).

Another limitation for the $(GO/LAC)_1$ thickness through XPS signal attenuation is the fact that the coating was demonstrated not to be homogeneous, with ~11% of its area being exposed to the substrate without GO flakes[46].

---

[1] Same physical samples as in Figure 35b and c.
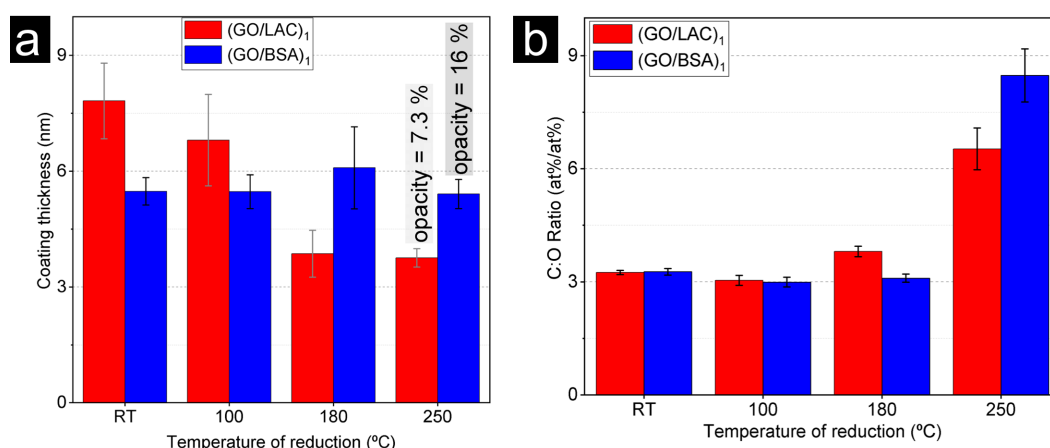
Figure 36 - Extracted and adapted from Nanoscale, 2019,11, 4236-4247 a) Coating thickness of films with bio-interfactants and the relationship with higher temperatures of thermal reduction. (b) Atomic concentration ratio [C]:[O] of bio-interfactant assisted coatings throughout temperatures of reduction.

Lastly, AFM images of the untreated and thermally treated samples were acquired. The samples are displayed in Figure 37 and show diverse degrees of topographies evolutions as a result of the thermal reduction. The control sample $(GO)_1$, kept a high degree of nanometric flatness but displayed 1D corrugations along the sample after thermal treatment (comparing Figure 37a and d). In the literature, similar results are explained by the weak attachment to the substrate SiO_2, leading to delamination.[131]

On samples with LAC and BSA, the starting topographies were flat with long-range features (near 100 nanometers, as in Figure 37b and c). After the thermal reduction, however, there was a development of dome-like corrugations (sizes <100 nanometers) and not the tunnel-like structure manifested in the control experiment.
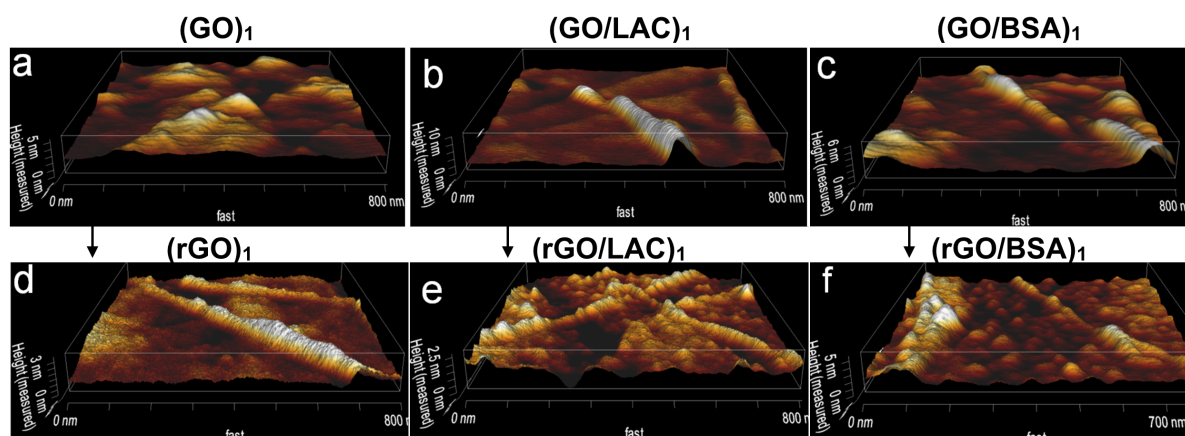
Figure 37 - Extracted and adapted from Nanoscale, 2019,11, 4236-4247 (a–c) Microstructure of the three investigated coatings $(GO)_1$, $(GO/LAC)_1$, and $(GO/BSA)_1$ respectively, scanned with AFM after having been freshly prepared. (d–f) AFM images of thermally reduced coatings at 250 °C coatings $(GO)_1$, $(GO/LAC)_1$, and $(GO/BSA)_1$ respectively.

These distinct domes were further characterized in detail with topographic measurements (Figure 38). The control sample $(rGO)_1$ and LAC-containing sample $(rGO/LAC)_1$ revealed to have shallow peak-to-valley features, below 0.5 nm. The sample with BSA, in contrast, resulted in high peak-to-valley heights; above 0.5 nm. These profiles and roughness values can be seen in Figure 38a-c and g-i.

The images were also characterized for their relative mechanical properties with the AFM-phase filter. In Figure 38g-i some correlation can be observed between low heights and low phase degrees. The overall view with this filter (Figure 38d-f) revealed that the samples have two high contrasting phases; bright clusters surrounded by darker regions. This fact alludes to the interpretation that these darker regions are anchoring points with the substrate, due to the harder[1] mechanical nature of such anchoring point with quartz.

These clusters, which are the topographic domes, are smaller and more concentrated on materials $(rGO)_1$ and $(rGO/LAC)_1$, with 824 and 918 peaks per μm^2, respectively. The sampled region in $(rGO/BSA)_1$ showed 492 peaks/μm^2.
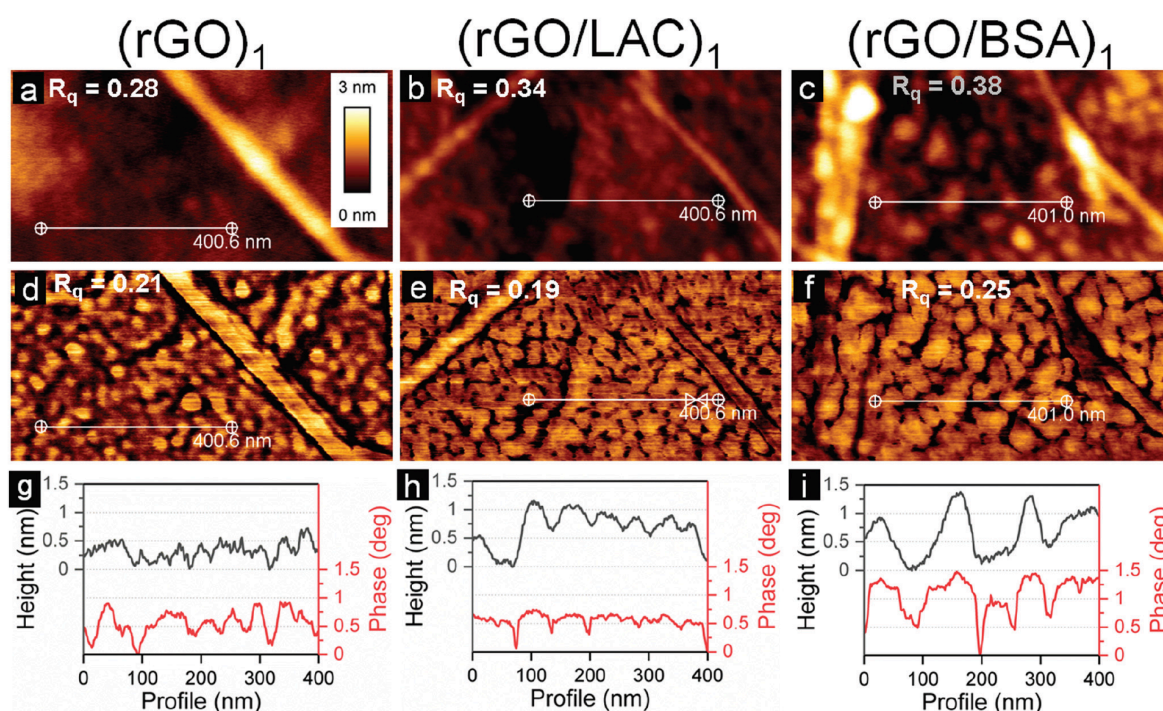
Figure 38 - Extracted and adapted from Nanoscale, 2019,11, 4236-4247. Height and phase images of the coating systems obtained by AFM. Sequence of columns (left to right) corresponds to $(rGO)_1$, $(rGO/LAC)_1$ and $(rGO/BSA)_1$ on fused quartz glass substrates, respectively. a–c, AFM height image of the three coating systems reduced at 250 °C. Rq values are in nm and are measured on the flat regions of the scanned area. Images scaled to relative height values from 0 to 3 nm. d–f AFM phase image of the same locations from images a–c. Rq values are in degrees and referent to flat regions of the scanned area. (g–i) Height and phase values extracted from the marked region (white line) on pictures a–f.

In the literature, several sources report the development of GO corrugations[40,131,132]. These topographic features were attributed to the formation of new bonds at the epoxide rings of GO[133], mismatch of the substrate thermal expansion[134], trapped solvent[134], and strong anchorage to the substrate[134]. These effects may cause stress on the coating and cause rippling.[135] Gas trapping was ruled out, as it was observed only when over seven layers of GO constituted the coating[105].

---

[1] As discussed in results from Figure 18b, these darker regions are associated with mechanically harder materials.

The final experiment in this subchapter is the electrical conductivity measurement of the thermally reduced coatings (at 250°C). Eight unique samples for each condition were prepared on quartz, resulting in data presented in Figure 39. The values of the measurements varied drastically between and within coatings. The logarithmic plot was used in order to compare the general trend of the three materials. In (rGO)$_1$ five out of eight samples had undetectable conductivity. The spread of values was higher for coatings with higher sheet resistances[1]. This high spread of values for (rGO)$_1$ and (rGO/LAC)$_1$ indicates that electrical conductivity is on the verge of being detected, which characterized the percolation point. Nevertheless, all samples with bio-interfactants resulted in measurable electrical conductivity in this set of experiments.
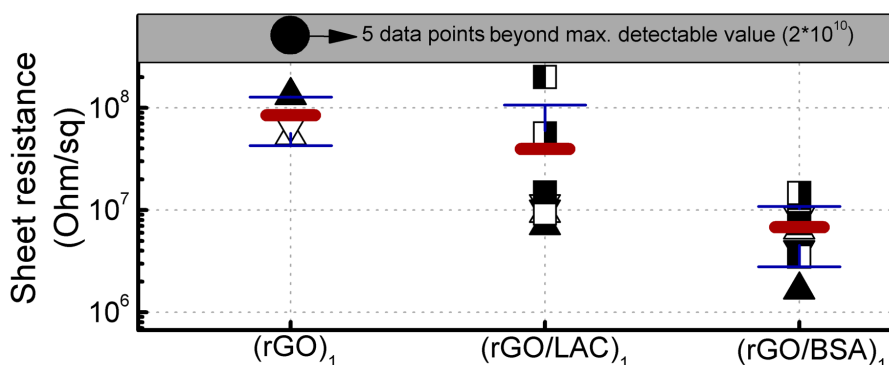
Figure 39 - Electrical conductivity of thermally reduced coatings. (N = 8 for each condition). Sample (rGO)$_1$ had five measurements that were undetectable by the instrument. The other 19 measurements were inside the detectable range.

The thermal reduction of GO provokes reactions that form paths for electrons. The initiation of the reduction is catalyzed by trapped water[136] (naturally arising from the GO dispersion and bio-interfactants[137]). Several reactions paths are possible: decarboxylation, attack on hydroxyls and/or ring-opening epoxides.[136] The reactions result in the release of O_2 and/or other O-containing species on GO (in which case, consuming the carbon backbone of GO).[30] These reactions develop new sp^2 sites and form percolation paths between them and original sp^2 clusters[105], resulting in a permanent acquisition of electron conductivity over a large area.

Mattevi *et al.*[105] also asserted that the electrical conductivity is not hindered by the overlapping flake junctions, but by the sp^3 within GO flakes which disrupt the graphene-like structure. Such experiment was demonstrated by comparing measurements of conductivity within one flake and across several overlapping flakes.

2.2.2.3 Further assembly and structure

Previous subchapters (2.2.1.1, 2.2.1.2 and 2.2.2.1) investigated the building blocks behind the assembly of GO-Bio$_{nanocoatings}$; it consists of surface functionalization ("step 1") and GO attachment ("step 2"). Also, the thermal reduction of these systems was explored in chapter 2.2.2.2. This subchapter explores the materials that arise from

---

[1] For (rGO)$_1$, 5 samples resulted in at least $2x10^{10}$ Ohm/square resistance, meaning that the average and standard deviation would be higher than that of (rGO/LAC)$_1$.

repeating the building blocks (step 1 + step 2) up to 10 times. Also, their thermally reduced counterparts were investigated.

The UV-Vis transmittance at 550 nm of these coatings, including the control experiment bereft of bio-interfactants, is plotted in Figure 40a. The control experiment $(GO)_n$ showed a tendency of gathering GO with each process repetition. $(GO/LAC)_n$ and $(GO/BSA)_n$ showed a stronger light attenuation along with n process repetitions. These changes of transmittance at 550 nm ($T_{550\,nm}$) were fitted with an exponential attenuation curve according to Lambert-Beer law.[138] The function applied was:

$$T_{550\,nm} = e^{-\alpha \times n}$$

The assumption for this plotting is that the transmittance exponential attenuation coefficient (α) is constant and that each process repetition n has an equal addition contribution to light attenuation.

This model fitted $(GO)_n$ poorly, judging by the low coefficient of determination. On the other hand, the model fitted light attenuation of $(GO/LAC)_n$ and $(GO/BSA)_n$ with high precision. The good fitting allows the interpretation that bio-interfactants facilitate assembly of "identical blocks"[1] of material for each process repetition n. The use of BSA yielded light attenuation coefficient (α) three times higher than that of LAC throughout the 10 layers of depositions: -3.9%/layer vs. -1.3%/layer. The three-fold difference indicates three times higher[39,139–142] capture of GO when BSA is used instead of LAC.[2]

Figure 40 - Extracted and adapted from Nanoscale, 2019,11, 4236-4247 - Published by The Royal Society of Chemistry. (a and b) Light transmittance (wavelength = 550 nm) for ten levels of depositions (n = 1 to 10) and for the three different coating systems in two states, (a) freshly prepared on quartz ((GO)$_n$, (GO/LAC)$_n$ and (GO/BSA)$_n$) and the same samples thermally reduced on (b) ((rGO)$_n$, (rGO/LAC)$_n$ and (rGO/BSA)$_n$). For each condition and each coating an exponential curve was fitted (intersection in Y=100%), the fitting parameters are indicated by color to each coating.

---

[1] Identical in terms of optical properties. A fixed light attenuation coefficient (α) is escalated along with the number of process repetitions n.

[2] It can be ruled out that the bio-interfactants play a role at the adsorptions at 550 nm (Figure 33).

The samples mentioned above were then thermally reduced and also evaluated for the transmittance (Figure 40b). The result is a decrease in light transmission for all samples along all levels of deposition. The exponential model was applied for these materials, too. The fitting was satisfactory for coatings with bio-interfactants and unsatisfactory for $(rGO)_n$. This supports the idea that thicker films still reduce in a similar fashion as the thinner films.

Electrical properties of the thermally reduced samples were also characterized (measured as sheet conductivity). The sheet conductivities of these coatings according to the number of deposition *n* are plotted in Figure 41. The range of values of these experiments is vastly different, therefore plotted in three separate charts. There was an increase of conductivity for higher process depositions in all samples.

The conductivities of these materials had some linear correlation with the number of depositions employed. Control experiment $(rGO)_n$ showed weak correlation for low *n* values probably due to percolation effects (supported by experiments in Figure 39). Coatings prepared with bio-interfactants demonstrated reliable linear scalability of electrical conductivity along with process repetitions *n*. This fact supports the idea that each layer of deposition can be seen as a similar building block in terms of electrical conductivity.
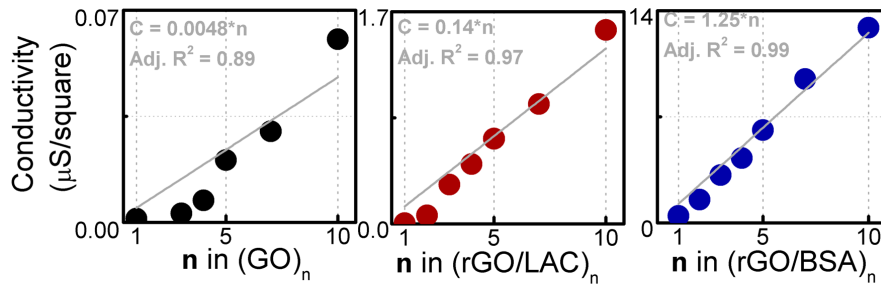
Figure 41 - Electrical conductivity (measured as the inverse of sheet resistance) of samples dependent on the levels of process repetition (n). The data in each chart was plotted with a linear fit intersecting at y=0.

By combining equations in Figure 41 and Figure 40b and isolating *n*, it is possible to obtain fundamental relationships between transmittance (T) and conductivity (C) for the coatings[143]; resulting in the following equations for each coating:

$$(rGO)_n: \qquad \log(T^{-1}) = 3.13 \times C$$

$$(rGO/LAC)_n: \qquad \log(T^{-1}) = 0.50 \times C$$

$$(rGO/BSA)_n: \qquad \log(T^{-1}) = 0.19 \times C$$

These equations tell us that for a given[1] transmittance *T* the coating with BSA manifests a superior electrical conductivity. It may be tempting to suggest that BSA (and LAC to a lower degree) promotes more overlapping of GO sheets facilitating

---

[1] That means distinct number of repetitions. For example, in order to achieve T = 50% the levels of depositions (n) would be $(rGO)_{49}$, $(rGO/LAC)_{10}$ and $(rGO/BSA)_3$. Also, since 0<T<1, log(1/T) is necessarily positive.

electron mobility, however, such overlapping could not be higher than in pure stacks of GO (free from the bio-interfactants). Moreover, the limiting factor of conductivity is not the overlapping, but the base of the flakes[105].

And since the amount of stacked GO flakes determine the light transmittance[39,139–142], it is the case that for the same light transmittance, there is at least[1] the same amount of GO on (GO)n as GO on (GO/LAC)n or (GO/BSA)n. That brings to the unequivocal conclusion that GO is reduced differently according to the surface it adheres to (bare quartz, quartz treated with LAC, or quartz treated with BSA).

The distribution of sheet resistances can also be used to estimate other film properties of these coatings. When taking percolation effect into account, the sheet resistance is expected to evolve as:[143]

$$R_s = \frac{1}{\sigma_{DC,B} \, t \, (\frac{t}{t_{min}})^{n_p}}$$

Where R_s is sheet resistance, t is the coating thickness, t_{min} is the critical thickness, $\sigma_{DC,B}$ is the bulk direct current conductivity of the film, and n_p is the percolation exponent. Thickness is the independent variable, and the other three parameters are fixed for each coating system. The optimization[2] of the model yielded the following results:

Coating system	$\sigma_{DC,B}$ (μS/cm)	t_{min} (nm)	n_p
(rGO)n	0.046	6.44	0.85
(rGO/LAC)n	0.19	5.65	0.52
(rGO/BSA)n	8.52	6.30	0.19

These results show that the conductivity is highest for assemblies with BSA, medium for LAC, and lowest for GO (for the same thickness). The critical thickness t_{min} is in the same range for the three materials, and it indicates latent effects on conductivity for higher thicknesses. Higher percolation exponent n_p indicates how abrupt is the percolation transition, highest for (rGO)n.

The calculated thicknesses (only based on the spread of sheet resistances) were compared to the light absorbances of these same samples and plotted in Figure 42. The choosing of absorbance versus thickness was based on the fact that the thickness escalates linearly with the absorbance values, following the Lambert-Beer law[138].

---

[1] It was demonstrated in Figure 33 that bio-interfactants contribute slightly, but positively, to light absorbance (reduction in transmittance).

[2] The boundary conditions were: thicknesses are increasingly higher for higher n, the first level of deposition is < 10 nm, the tenth layer of deposition is < 300 nm. 10 > t_min > 0.01, 10^-5 > $\sigma_{DC,B}$ > 10^-10. In the first optimization, the thicknesses known from other techniques were fixed in order to find the right order of magnitude of the other parameters. After this first optimization, all parameters and thicknesses were simultaneously fitted and did not reach any limit for the boundary conditions.

A satisfactory linear fitting of these thicknesses versus absorbance would indicate that the percolation effects were adequately taken into account and that estimated thicknesses would translate linearly into light absorbance. The coatings $(rGO/LAC)_n$ and $(rGO/BSA)_n$ fit in this model accounting for a broad range of thicknesses (from few nanometers to hundreds of nanometers). However, the model is limited when fitting a straight line for $(rGO)_n$ (Figure 42a).
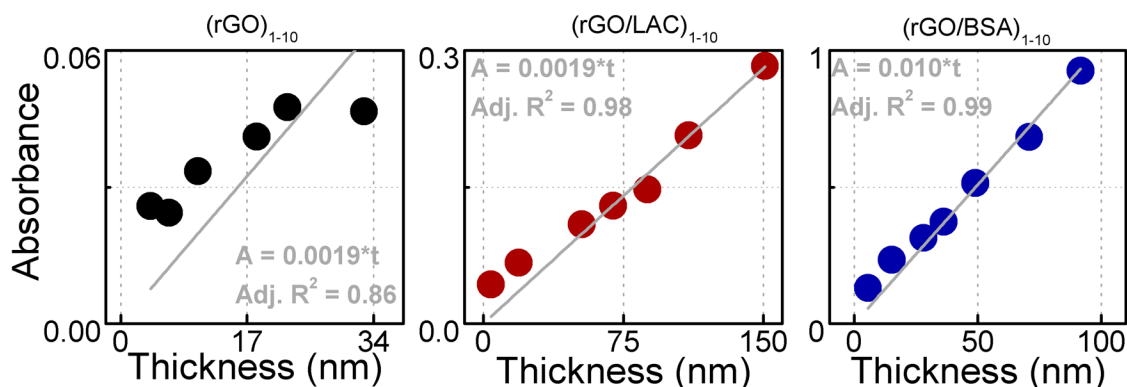
Figure 42 – Thickness of reduced coatings calculated by percolation model (X-axis) versus the absorbance measured for these materials (Y-axis). On these plots, a linear curve is fitted since absorbance linearly increases with the thickness of a given homogeneous material.

XPS was additionally employed to investigate multiple coating depositions of $(rGO/LAC)_n$. Since XPS is a highly surface-sensitive technique, only 1,2 and 4 layers or deposition were investigated and observed for the substrate attenuation. The plot of the high-resolution C1s spectra and the calculated thickness are displayed in Figure 43. Linear scaling of thickness was observed for such material; roughly 4 nanometers of material is the size of one (rGO/LAC) block (Figure 43d).
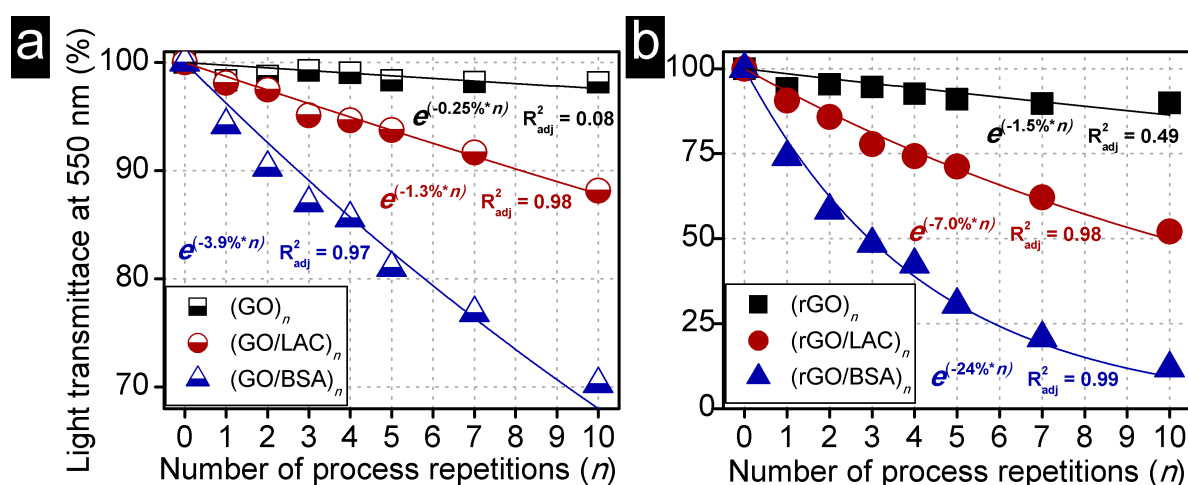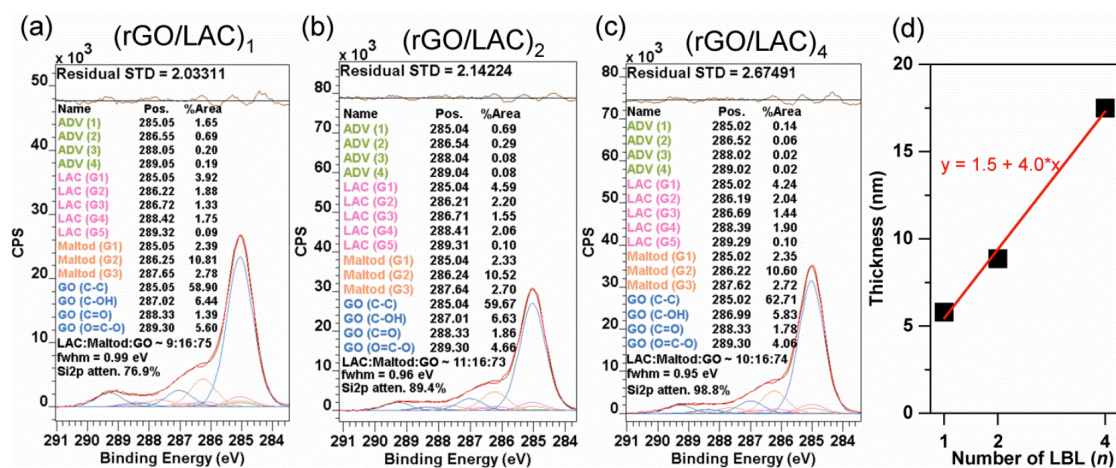

Figure 43 - Extracted and adapted from Nanoscale, 2019,11, 4236-4247 - Published by The Royal Society of Chemistry. C1s high resolution XPS spectra of 1, 2 and 4 LBL of process using LAC as bio-interfactant (images a to c). The deconvolution of the spectra was corrected by adventitious species from the substrate and plotted using components from the substances used in the process (LAC27, Maltodextrine27, and BSA28), the best fitting indicated that the ratios among these substances do not change substantially. From the substrate attenuation, it was also possible to plot the layer thickness in (d). (d) linear fit indicates that the coating increases approximately 4 nm for every process repetition.

The XPS also allowed deconvolution of the contributing signals from the coating. It was found that the three samples with different number of process repetition, *n*, had similar proportion of GO and bio-interfactant. Also, the level of oxidation of the GO

inside these three coatings is similar, with ~82% of the carbons being identified as sp^2 (binding energy ~285 eV).

Another way to measure the thickness in a micrometric scale (area evaluated ~400 times smaller than XPS) is with a laser scanning confocal microscope (LSCM). An indent can be made on the sample surface with a sharp scalpel knife. LSCM has enough resolution to evaluate the thicker films and measure the disruption caused by the scalpel on the topography. Two coating systems and two levels of depositions were assessed: n = 5 and 10 for both $(rGO/LAC)_n$ and $(rGO/LAC)_n$.

The resulting topography in Figure 44 shows the areas averaged for height comparison. The substrate relative height average (C_{height}) was assumed to be the height averages inside the white markers, and the coating height average (C_{height}) was assumed to be the average points inside the black shapes. The coating depth was calculated to be "$\Delta h = C_{height} - C_{height}$".
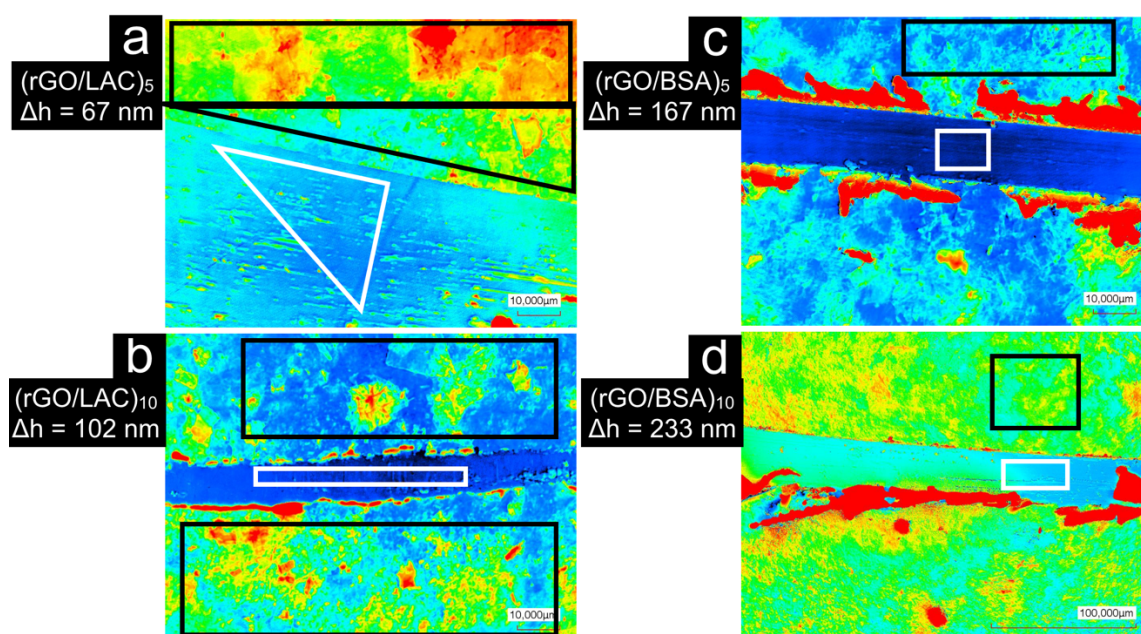
Figure 44 – LSCM (Laser Scanning Confocal Microscopy) of coatings with bio-interfactants at 5 and 10 levels of depositions. On all samples, a sharp scalpel was employed to cut the coating all the way to the substrate. The height of the coating was defined by the average height difference between the substrate (areas inside white shapes) and the coating surface (areas demarked in black). Color tone (blue to red) indicates the depth of the scanned area; from deeper (blue) to more superficial (red). (a), (b), (c), and (d) are, respectively: $(rGO/LAC)_5$, $(rGO/LAC)_{10}$, $(rGO/BSA)_5$, and $(rGO/BSA)_{10}$.

As the last method to measure thickness, AFM was employed. The area assessed is nearly 200 times smaller than that for LCSM, and the height resolution is sub-nanometer. Areas were scanned for showing the substrate at the same time as the

coating, which was easily found for (rGO/LAC)$_1$, but for (rGO/BSA)$_1$ it took scanning of numerous distinct areas in order to identify such condition (Figure 45).[1]

The same procedure as for LSCM was taken in order to measure the height thickness. In Figure 45 substrate height (values inside the green perimeter) and coating height (values inside the blue perimeter) were individually averaged for their heights, and the difference characterized the coating height, depicted on the shapes in Figure 45.

Figure 45 – Extracted and adapted from Nanoscale, 2019,11, 4236-4247 - Published by The Royal Society of Chemistry. AFM of coatings (rGO/LAC)$_1$ (a-b) and (rGO/LAC)$_1$ (c-d), images (b) and (d) being the 3D projection of the left images. The height of the coating (average of areas in blue perimeter) was compared to the height of the quartz glass substrate (highlighted with green perimeter).

To summarize these measurements, the values are compiled and plotted in Figure 46 and Figure 47, for (rGO/LAC)$_n$ and (rGO/BSA)$_n$, respectively. The techniques XPS, AFM, LSCM, and the percolation model[2] are techniques independent of each other and are represented in symbols in Figure 46 and Figure 47. The measurements from these four techniques were from samples also measured with the UV-Vis. With these measurements, calibrations could be conducted (and plotted as lines Figure 46 and Figure 47). For example, a "UV-VIS/AFM-calibrated thickness" of (rGO/BSA)$_1$ was acquired by the following procedure: AFM measured 5.75 nm of thickness and UV-

---

[1] The lengthy process of scanning for uncovered areas in (GO/BSA)$_1$ films is in parallel with the previous observations that coatings with BSA have a higher coverage.

[2] Detailed after Figure 41

VIS measured 0.13 of absorbance; meaning that the ratio of 0.13/5.75 (or 1/44) is fixed (1 unity of absorbance corresponds to 44 nanometers of thickness). In that scenario, for example an absorbance of 0.26 would correspond to 11.5 nm.

For $(rGO/LAC)_1$ (lines Figure 46) there is a good agreement between XPS and the percolation model (5.8 vs. 4.2 nm, respectively). However, as discussed above, XPS measurements assumed homogeneous coating and were found not to be so with AFM [1] and LSCM [2] measurements. This means that the XPS technique is underestimating the thicknesses (and calibrating the UV-Vis for lower values).
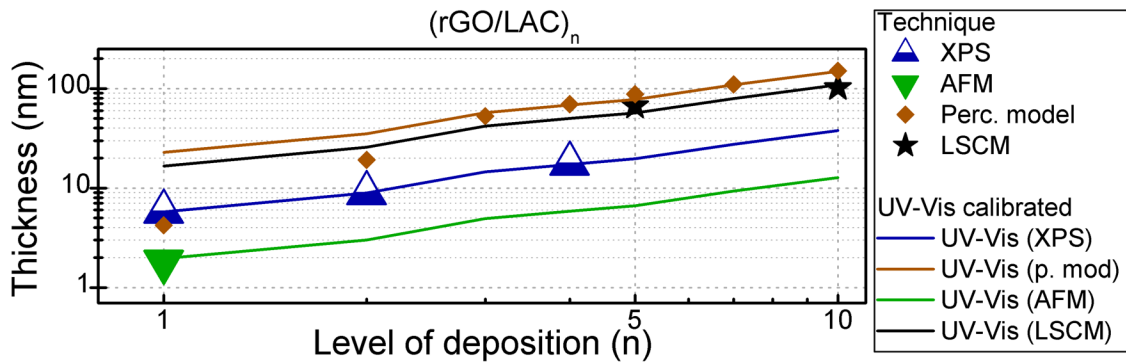
Figure 46 – Levels of process repetition n vs. thicknesses values for $(rGO/LAC)_n$. Scales are in logarithm in order to show details along all ranges of depositions. Table on the right indicates the methods employed to estimate the thicknesses; either by a technique (marks on the charts) or by calibrated method (lines on the chart).

In $(rGO/LAC)_1$ the AFM measures a thickness still below all the other methods. This incongruence is probably because the measurement was highly localized, not taking into account rougher areas of the $(rGO/LAC)_1$ coating (Figure 48). Such a bigger area revealed that the sample is mostly flat, but there are agglomerations and several-nanometer range variations in thickness (for example in Figure 48b from X = 5 to 10 µm), which could explain the localized thin thickness observed in AFM (Figure 45a). The single-observation value calibrates the UV-Vis (green curve) necessarily to underestimated values.

On the other hand, the percolation model for $(rGO/LAC)_n$ and its UV-Vis derivation (brown line and brown symbols) are estimating the thickness of the coating to be the highest. The estimation exceeds the measured values in the LSCM, for example, it estimates ~150 nm of thickness for $(rGO/LAC)_{10}$ and LSCM measured ~100 nm. The substantial difference invalidates the percolation model (and therefore the UV-Vis calibrated curve).

The UV-Vis estimations from XPS (blue line) are substantiated by three points (blue symbols), indicating that the thickness for $(rGO/LAC)_{10}$ would be ~40 nm (blue curve). However, the thickness was instead measured to be ~100 nm. This result can be explained by a "puffing" effect from the thermal reduction. Such expansion could be a

---

[1] One level of deposition showed to have ~11% of areas exposed to quartz.[46]

[2] The pictures in Figure 44 show that the topography homogeneity is higher for coatings with BSA than for LAC judging by the homogeneity of colors.

result of gas trapping, a phenomenon particularly observed when GO coatings are thicker than 7 layers of GO[105]. In that hypothesis, LCSM shows that coatings $(rGO/LAC)_{5 \text{ and } 10}$ are not densely packed. The discrepancy between measurements of XPS and LSCM on thicknesses of $(rGO/LAC)_4$ to $(rGO/LAC)_5$ could be explained by (i) the puffing effect happens for n > 4 and/or (ii) XPS attenuation signal is only defined by the amount of material, not its spacing (for example in case the material is puffed).
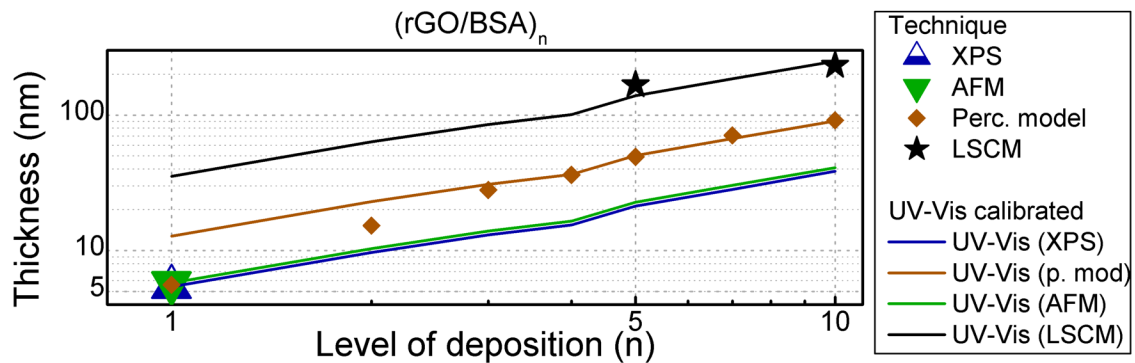
Figure 47 - Levels of process repetition n vs. thicknesses values for $(rGO/BSA)_n$. Scales are in logarithm in order to show details along all ranges of depositions. Table on the right indicates the methods employed to estimate the thicknesses; either by a technique (marks on the charts) or by calibrated method (lines on the chart).

The measured thickness of $(rGO/BSA)_n$ for *n* = 1, that is, with XPS, AFM, and the percolation model, have good agreement with each other (5.4, 5.8 and 5.6 nm respectively). Such similarity among all three independent methods strongly supports that the methods themselves probably rely on correct premises. Also, therefore, the UV-Vis calibration from these models (XPS, AFM, and percolation model) relies on at least one precise value.

In the highest extreme (Figure 47), these methods predicted $(rGO/BSA)_{10}$ to have the thickness between ~40 and ~90 nm. However, when considering the actual observation of the material through LCSM, a vastly thicker layer was encountered. The device scanned a thickness of 233 nm (Figure 44d). A similar trend is observed for n = 5, with an expected thickness between ~20 and ~50 nm, but found to be 167 nm with the LSCM. These results also show that probably there is a puffing effect on high levels of deposition on $(rGO/BSA)_n$. This suggests that the UV-Vis/LSCM-calibrated model (higher black curve) is probably an appropriate technique for estimating the coating thickness for high numbers of deposition *n* (the model takes the puffing into account).

As mentioned above, in the case of $(rGO/LAC)_n$ the percolation model was ruled out because it overestimated the thickness of the coatings.[1] However, in the case with BSA, the percolation is not immediately ruled out, because the puffed material may still contain the amount of material required for the electrical conductivity predicted by the percolation model. The divergence between the percolation model and the models

---

[1] The percolation model considers the physical matter of the material in bulk form, that means that if it predicts a thicker material than the actual observed thickness (due to high electrical conductivity), the model necessarily fails to consider other relevant factors.

based on AFM and XPS is unexpected and would require more experiments in order to assert which model is more precise.

An intriguing observation of these puffed materials (in both cases, with BSA and LAC) was that among levels 5 and 10 the conductivity and absorbance properties were approximately duplicated (as expected). However, the thickness between n = 5 and n = 10 only escalated ~1.5 times. That means that the puffing phenomenon is relatively more expressed on level 5 than on level 10.
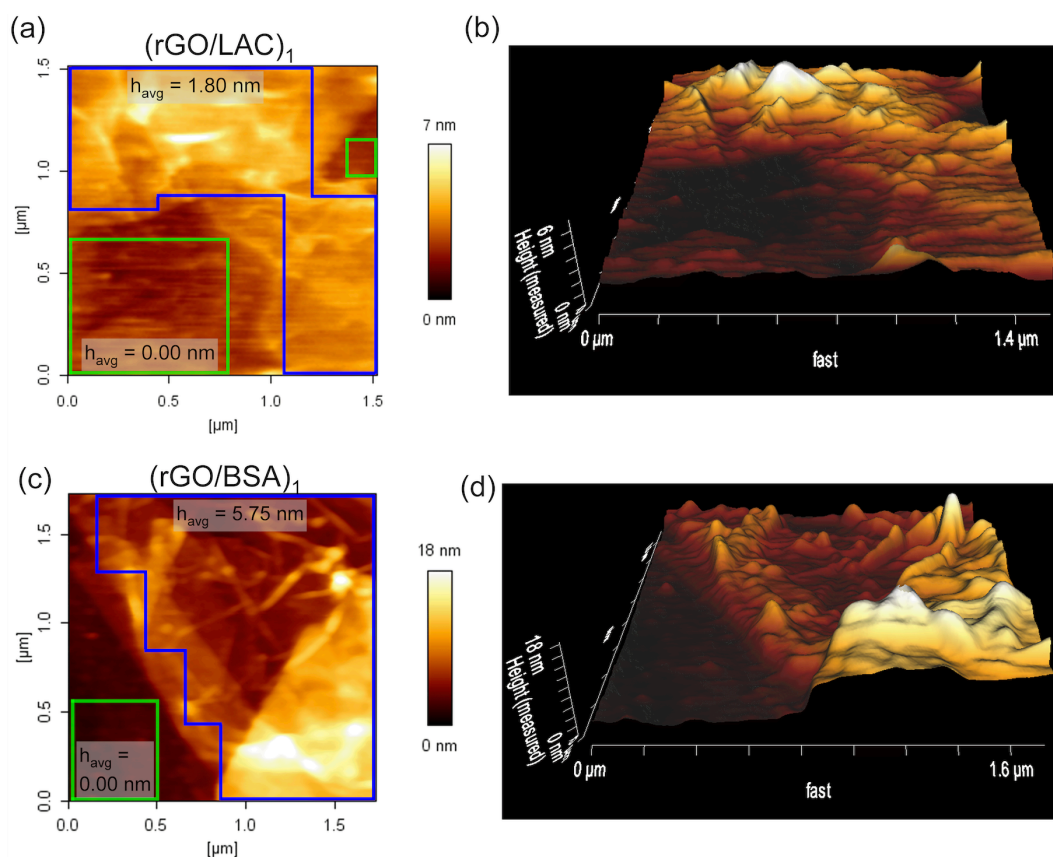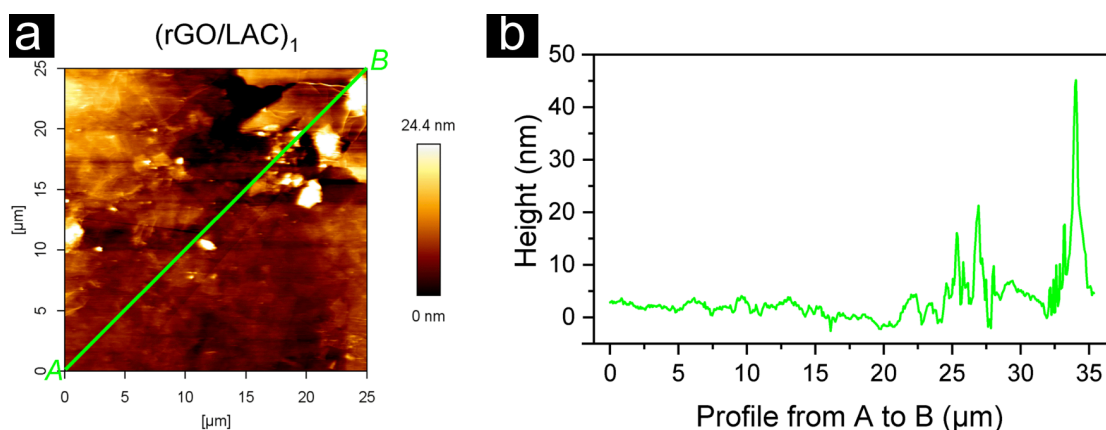

Figure 48 – Extracted and adapted from Nanoscale, 2019,11, 4236-4247 - Published by The Royal Society of Chemistry (a) Large AFM scanning of (rGO/LAC)$_1$, showing mostly flat areas and rough features. Profile of heights A to B (green line in (a)) is depicted in image (b).

2.2.3 Robustness of coating

Extracted and adapted from Nanoscale, 2019,11, 4236-4247 - Published by The Royal Society of Chemistry.

The capability of a coating to strongly adhere to a substrate is vital for applications where there is direct interaction with the medium, for example in wearables, sensors that have to endure exposure to tribological loadings or contact with liquids. In real-world applications, graphene needs to be supported (and kept) on a substrate to perform its function.[1]

In order to test and compare the robustness of the thermally reduced coatings studied here, they were exposed to ultra-sound bath in deionized (DI) water in order to induce coating destabilization or destruction by cavitation. The corresponding decay of electrical conductivity was measured during the time of the experiment as a form to assess the durability of the coatings (Figure 49a). Additionally, a commercially available transferred CVD graphene on quartz (Graphenea) was also exposed to this test for comparison. The values are relative to the first measurement at 0 minutes (when each relative conductivity is 100%). After only 7 minutes inside the ultrasound bath, there was no more detectable electrical conductivity on the commercial transferred CVD graphene film. Our own three other coatings derived from GO showed a slower decay in electrical conductivity. The ones prepared on previously adsorbed bio-interfactants, in particular with BSA, kept a high relative conductivity for a longer time.
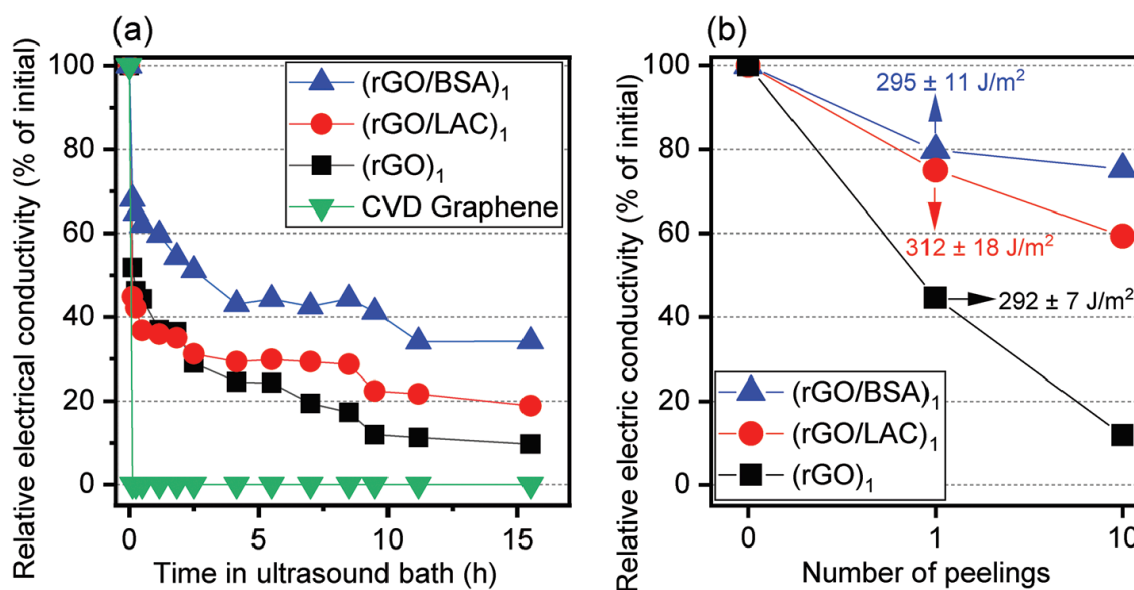
Figure 49 - Extracted and adapted from Nanoscale, 2019,11, 4236-4247 - Published by The Royal Society of Chemistry. (a) Evolution of relative electrical conductivity decay when samples were exposed to ultrasonic water bath. The samples (rGO/BSA)₁, (rGO/ LAC)₁ and (rGO)₁ were reduced at 250 °C. (b) Change of electrical conductivity of coatings after 180° peeling test with conventional tape; further peelings on the same sample were conducted with new parts of the tape. Numerical values in the (b) indicate the peeling resistance energy measured in the first peeling.

A peeling test (Figure 49b) with conventional pressure-sensitive tape was carried out on the three coatings to determine the changes of the film proprieties. The force from the tape peeling was also measured and resulted in values in the same range for the three coatings (Figure 49b). However, the reduction in electrical conductivity was more dramatic for the $(rGO)_1$ film. Further peelings had the same effect, and BSA in this case acted as a component key for higher resistance as well. Light transmittance (at 550 nm) was measured before and after the sequence of ten peelings; the three coatings suffered minor changes in light transmittance (< 3%).

In a recent study,[48] it was observed that the peeling work (from nano-scratch techniques) of a GO film on glass decrease dramatically (from ~350 J/m² to 38 J/m²) after thermal reduction due to the removal of oxygen-containing groups, which were associated to be the main contributor to the van der Waals forces with the substrate. In parallel to these findings, our macroscale peeling tests indicated that the average energy of ~300 J/m² is enough to cause severe disruption in the conductivity of the rGO film. However, when assisted by the bio-interfactants, the electrical conductivity was sustained to near-original values through the ten peelings. As a comparison, CVD transferred graphene was found to adhere to SiO_x with energies between 3 and 20 J/m².[144]

Both enduring tests support the model of strong anchoring when using bio-interfactants, especially BSA, as observed with other techniques. The destruction induced by both techniques indicates higher durability both at the nanoscale and at the macroscale when bio-interfactants are employed.

2.3 Summary

In summary, chapter 2 detailed a new process route to produce nanometrically-thin coatings with graphene oxide, here denominated GO-Bio$_{nanocoatings}$. The subchapters explored specific mechanisms at work, allowing the formation of these coatings.

It was found that GO can spontaneously attach to substrates when these are exposed to a GO dispersion. However, a high degree of inhomogeneity was found when quartz is used as a substrate[1]. This inhomogeneity was observed even among large evaluated areas, on millimeter and centimeter range.

On a parallel study, two other materials were also assessed for their adsorption; these materials are "LAC" and "BSA"[2], which are denominated "bio-interfactants". These materials can readily be adsorbed on several substrates and change their surfaces energies. LAC was found to show varying degrees of adsorption on quartz samples. In contrast, BSA was found to be adsorbed with higher homogeneity on quartz.

The two parallel studies (on GO and on bio-interfactants) were strategically united. Substrates were firstly dipped in bio-interfactants mixtures and then dipped in GO dispersion. Even with vigorous rinsing after both dipping, this route was found to result in deposition of a more homogeneous GO coating (when compared to not conducting the bio-interfactant dipping). It was also found that the type of bio-interfactant played a role in the final deposited material. Compared to LAC, BSA (i) gathered more stacked GO flakes in the average, (ii) showed a higher degree of quartz coverage, (iii) resulted in coating with higher dimensional homogeneity, from nano- to millimeter scale and (iv) attracted less-oxidized GO flakes when dipped in a GO dispersion. These differences were attributed to the distinct amino acid distribution of these bio-interfactants.

The GO-containing materials mentioned above can then be thermally reduced in very mild conditions (250°C) and echo desirable properties from graphene, like electrical conductivity. When BSA was used in combination with GO in the thermal reduction, it demonstrated to anchor strongly to GO and to the substrate, leading to a chemical selectivity that produced more graphene-like properties as compared to the use of LAC or with the control experiment.

The bio-interfactants and GO can also be used in alternating sequential dipping, also known as layer-by-layer depositions. Both LAC and BSA allowed the coating properties to scale linearly with the number of process repetitions, even after thermal reduction. For example, ten layers of deposition produce a material ten times more conductive than the one layer or deposition. However, the typically conflicting properties "high transparency vs. high conductivity" favor coatings with BSA, which

---

[1] GO can be more easily adsorbed on polyimide films.

[2] Both are commercially available biomolecules. LAC is a mixture of the enzyme Laccase from Trametes Versicolor and BSA is the protein Bovine Serum Albumin.

shows that the chemical selectivity (of GO flakes and their reduction paths) is also scalable.

The thicknesses of the layer-by-layer coatings with bio-interfactants were extensively evaluated using five methods. Evidence was presented showing that these materials "puff" as a result of thermal reduction as long as at least 5 levels of deposition are applied. Nevertheless, scalable thicknesses from few-nanometers to hundreds of nanometers can be achieved with these materials.

As a final "real world" proof of concept, the ultra-thin coatings were exposed to harsh conditions (dipped in water with ultrasonic vibration and scotch tape peeling) and proved to endure the tests while holding their electric properties. Coatings with BSA and LAC held their properties to a higher degree than coatings without bio-interfactants and even outperforming a pure form of graphene (CVD).
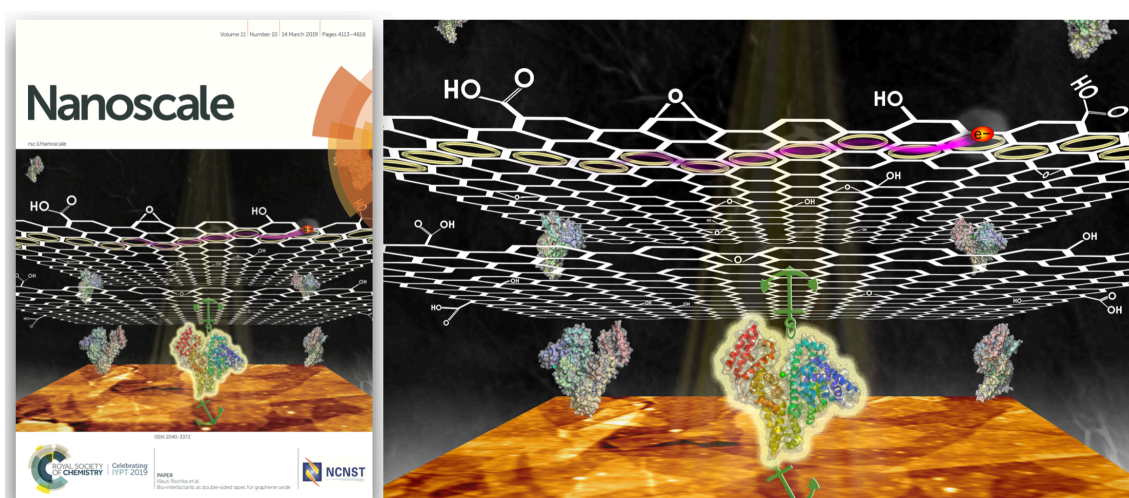
Figure 50 – - Front Cover featured in Nanoscale. Extracted and adapted from Nanoscale, 2019,11, 4236-4247 - Published by The Royal Society of Chemistry.

Finally, the characteristics discussed above were portrayed in a concept visualization (Figure 50, which was featured as a front cover at *Nanoscale*). The picture depicts a bio-interfactant (BSA) anchored to the substrate and to a graphene-like structure, functioning as a double-sided tape. Other properties are also represented there: electrical conductivity, transparency, and further layer assembly.

3   Study case for industrial application

Considering that scientific innovations are building blocks of imminent technological achievements, the graphene-based material detailed on the previous section was explored as a potential new formulation for the hair care industry. Many aspects have to be considered when developing a new hair cosmetic for example human safety and its environmental impacts. Even aspects that are not objectively scientific are relevant for launching a new hair cosmetic, for example: demands across different cultures, costs associated with regulations from different geopolitical areas and marketing strategy of new technologies. However, this chapter focuses on measuring and discussing the effects of applying rGOBio$_{nanocoating}$ on human hair, addressing the research question "What are the cosmetic benefits of adding graphene-like thin coating on human hair?".

In the cosmetic industry there is a constant demand for innovation and discovery of new materials that can bring benefit to consumers. Graphene is not outside of the radar of research, Luo *et al.* [145] for example have explored the benefits that graphene-based materials can bring when applied as a hair cosmetic. They have investigated a graphene-in-polymer coating (2 µm thick) on human hair. Their coating echoes electrical, thermal and optical properties of graphene, which are explored to achieve compelling effects like anti-static, heat dissipation and black dyeing, respectively. However, the cosmetic benefits of a truly nanometric coating of a graphene-like material remained to be characterized and added to the state of the art.

Typically, each cosmetic effect (anti-staticity, ease to comb, dyeing, UV-protection, etc.) is delivered by individual chemicals and/or processes that are tailored to specifically address these demands. For example, in the formulation of "Windle and Moodie – Invisible day and night cream" (Annex 2) the formulation combines, Distearoylethyl Dimonium Chloride (CAS: 67846-68-8) and Ethylhexyl methoxycinnamate (CAS: 5466-77-3) in order to provide conditioning effects[146] and UV protection[147], respectively. Also, fewer chemicals can offer multipurpose desirable effects, for instance in the product "Living Proof – Nourishing Styling Cream" (Annex 3), where it is claimed that Octafluoropentyl methacrylate (CAS: 355-93-1) "does three things: blocks humidity, smooths hair and helps repel dirt and oil to keep hair cleaner" (Annex 3). Discovering single ingredients that combine multiple desirable properties is relevant for simplification of registration and avoids further tests to certify product shelf stability. The results presented in this chapter explore multi-purpose cosmetic benefits of rGOBio$_{nanocoating}$ on human hair.

Besides investigating those benefits, it was also of interest to measure the durability of the attained effects. There is a demand for products that can deliver over longer periods of time without reapplication or maintenance[148,149]. Furthermore, it is also preferable that less cosmetic waste end up in water systems (like sewage or natural bodies), which justifies the development of long-lasting-effect products.

The fundamental knowledge of human hair is relevant for discussing the results achieved in this research, therefore a brief summary of the relevant literature is presented in the next section. Following that, the results of the interaction of the nanometric continuous graphene-like coating (rGO-Bio$_{nanocoating}$) on human hair are shown.

3.1 Fundamental aspects of human hair

3.1.1 Human hair fiber structure

Having hair on bodies is a common characteristic of mammals and similarly to these animals, the human hair is an evolutionary feature that provides protective, sensory, and sexual attractiveness functions[150]. Humans have been exposed to a variety of environments, resulting in diverse evolution strategies to cope with external demands.

The early humans from Africa were exposed to high UV radiation, and mainly due to their upright position, highly coiled and long hair were evolutionary adaptations[151]. It is speculated that the evolution of straight hair in Europe was a strategy to cope with colder climates, resulting in selection of hair covering the ears and neck. Another thermal insulation strategy is having a high density of hair (number of hairs per area of skin), which prevents heat loss by evaporation. The natural curvature of a grown human hair (varying from coyly to straight) is a consequence of the cross-section of the hair, from being close to a circle (low elliptical ratio) to having a cross-section shape similar to an ellipse (Figure 51).
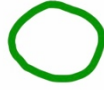
Figure 51 - Schematics of human hair axial shapes in relationship to cross-sections. Typical values of elliptical ratio (e) and diameter (⌀) given in the right part of the table. Adapted from[152].

Under microscopic inspection, the human hair is assembled by a central structure (the cortex) surrounded by several enclosing layers of cuticles (Figure 52). The cuticle is of particular interest in this research since it is the surface that directly interacts with the external world (and hence, where the graphene-like coating is formed). The cuticle is structured by several organic layers and the outermost structure is the cell membrane (named epicuticle) which measures ~14 nm and also encompasses a layer of lipids. Such lipidic coverage is the 18-methyl-eicosanoic acid (18-MEA)[150,153], also detailed in Figure 52.

The 18-MEA layer is covalently bond (via thioester linkage) to the cysteine-rich epicuticle[154] and provides surface properties that are typically advantageous (hydrophobicity, softness, shininess and more aligned fibers)[155–157]. It is of interest to preserve this natural layer of lipid, since it is covalently bound. It can be damaged by exposure to chemicals (ex; dyeing processes)[158,159] and to mechanical loads (for example, by combing)[159].

Some investigations claim replenishment of the lipid layer ([160,161]), also with covalently attached groups [162–164]. However, no literature reference was found where a new covalently bond 18-MEA lipid layer could be applied to restore the natural surface of the hair.
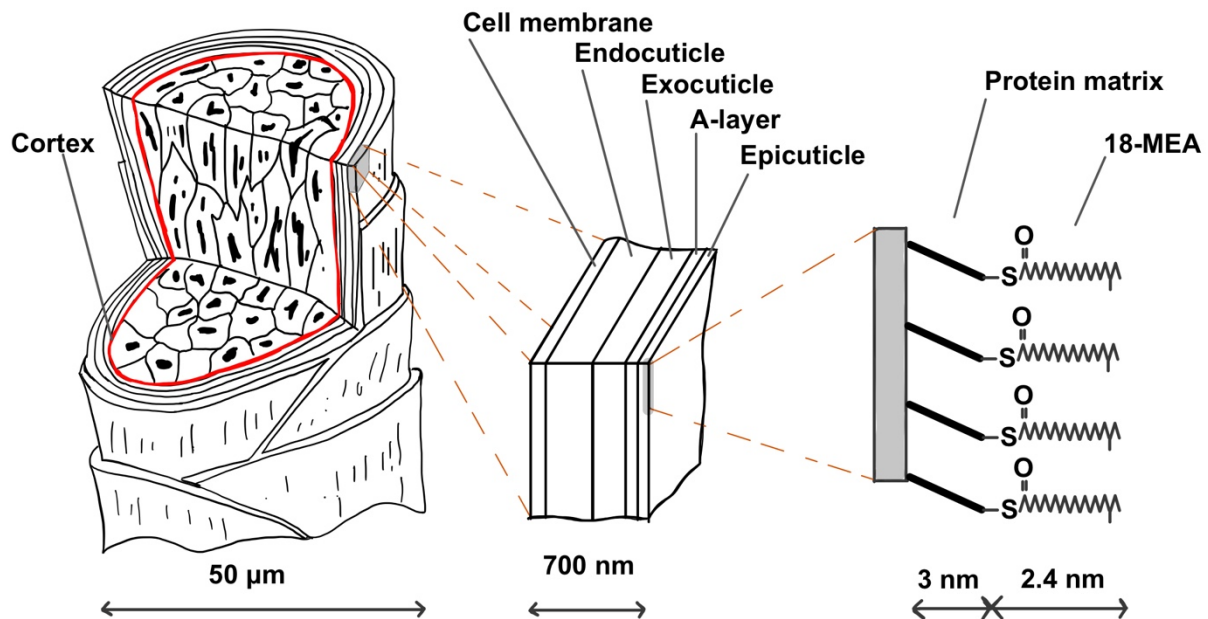
Figure 52 - Model representation of human hair, from micro- to nanometric scale

3.1.2 Human hair natural color and hair dyeing

The color of natural human hair is a consequence of how different types of melanin manifest themselves in the hair cortex. These pigments can be of two types, eumelanin (brown/black) or pheomelanin (yellow/red). Their agglomeration size, ratio, distribution, and total concentration are determinant factors to the color that is perceived[151].

Humans may also look for procedures that alter their hair color, and the earliest observation of dyed hair is over 2000 years old[165]. The techniques evolved substantially, from using natural pigments to complex chemical processes that bleach and add color in the hair. Typically, the coloring processes are divided into four groups;

1- Permanent (or oxidation dyes): consist of chemicals that lift the hair scales and add color inside the hair shaft (with or without bleaching colors that were previously present). This process deposits pigments that are not removable with shampoo, hence "permanent dyes".
2- Semipermanent dyes: consist of chemicals that are also diffused into the hair but do not bind firmly and do not use hydrogen peroxide to develop the hair color. Such semipermanent solution lasts less than 6 washes typically.
3- Temporary dyes (or color rinsers): are similar to semipermanent solutions, but with even weaker binding properties, lasting until the next wash.
4- Other dyes: This group is less commercially relevant as the other categories, containing groups like metallic dyes and vegetable dyes.

In literature reviews[152,166–169] no mention was found of nanometrically thin continuous films that are used as a hair cosmetic. Typically, the approaches to color hair are guided by oxidation and/or diffusion processes, not external surface modification.

3.2 Materials and methods

For the investigations, several types of human hair were used, with varying color and texture. The samples were provided from volunteers and from Kerling International. Samples from Kerling International were provided in tied and glued bundles prepared prior to cutting. Free length of 13 cm and a mass of 1 g. The state of the hair samples was cleaned with neutral shampoo and had not been previously treated with chemicals (hence, virgin hair). Hair samples were treated with the layer-by-layer process described in the previous section of this work. As a rule, the process $(rGO/BSA)_1$ was applied by the following steps:

1. A water-based formulation with the following three ingredients was freshly prepared: 0.2 mg/ml of BSA (CAS: 9048-46), 6 mg/ml of Acetic Acid (CAS: 64-19-7) and 13.7 mg/ml of Sodium Acetate (CAS: 127-09-3). Hair is embedded in this formulation for 45 minutes, followed by short rinsing in DI water (using a low flow stream for around 4 seconds).
2. The hair sample from step 1, drenched with water, is embedded in a 1 mg/ml of water-based Graphene Oxide for 30 minutes, followed by short rinsing in DI water (using a low flow stream for around 4 seconds).
3. Hair from step 2 is gently combed and let to dry under laboratory conditions (20°C and 50 %$_{RH}$). It is then placed in an atmosphere-controlled oven, which is fed N_2 gas during the thermal reduction process. The temperature cycle is as follows: heating from 20 °C to 225°C at 10 K/min, temperature is kept at 225 °C for 5 minutes and lastly the sample is removed from oven. The value of 225°C was chosen based on the operating temperature of typical hair straighteners.

The shampoo washing procedure was conducted by wetting the entire hair sample in tap running water at approximately 30°C. Next, a drop of shampoo is spread evenly on the wet hair and rubbed 5 times from top to bottom with pinching fingers. Finally, the hair sample is placed on the running water and with 10 pinching movements the shampoo is removed from the hair.

Electrical conductivity of hair was measured with the multimeter 15XL, Wavetek (sensitive up to 2 GOhm). In the experiment set-up, 16 stings of parallel hair were gold coated leaving a gap of 5 mm not coated with gold. Electrical resistance of the gap was measured by probing the gold-coated regions separated by the 5 mm gap. Samples in the following conditions were measured with this set-up: $(GO/BSA)_1$, $(rGO/BSA)_1$, virgin hair and virgin 225°C-reduced hair. This set-up has the limit of measuring $10^{-10.2}$ S/(hair.cm) (or $10^{9.1}$ Ohm/sq assuming average diameter of 60 μm for the hair sample and assuming that transport happens on surface).

Hair color characterization was done by acquiring images of the hair in a document scanner (Konica Minolta C364) in order to ensure the same light conditions. The image acquisition rendered *.pdf* files with resolution of 600 pixels/inch and 3 color channels; red, green and blue (RGB), each with 256 color tones. The image of the scanned hair

was characterized with Photoshop and evaluated with RGB channels. For the color characterization the median values of each RGB channel were used in order to convert[170] to HSL (hue, saturation and lightness) color codes. This single HSL color code is considered here to be the characteristic color. More details of this procedure is presented in 3.3.4.

3.3 Results & Discussions

3.3.1 Microstructure

Different from other traditional methods where diffusion-guided chemicals deliver the cosmetic, the process used in this research is expected to play a role in the hair nanoarchitecture since it is based on the attachment of a continuous layer of graphene-like material. In order to characterize the microstructural surface of human hair treated by $(rGO/BSA)_1$, a set of samples was prepared for SEM in the following three conditions;

1- Virgin Caucasian hair cut at 20 cm from the roots
2- Hair from condition *1* treated with $(GO/BSA)_1$
3- Hair from condition *2* thermally reduced (215^oC) and washed with shampoo 16 times
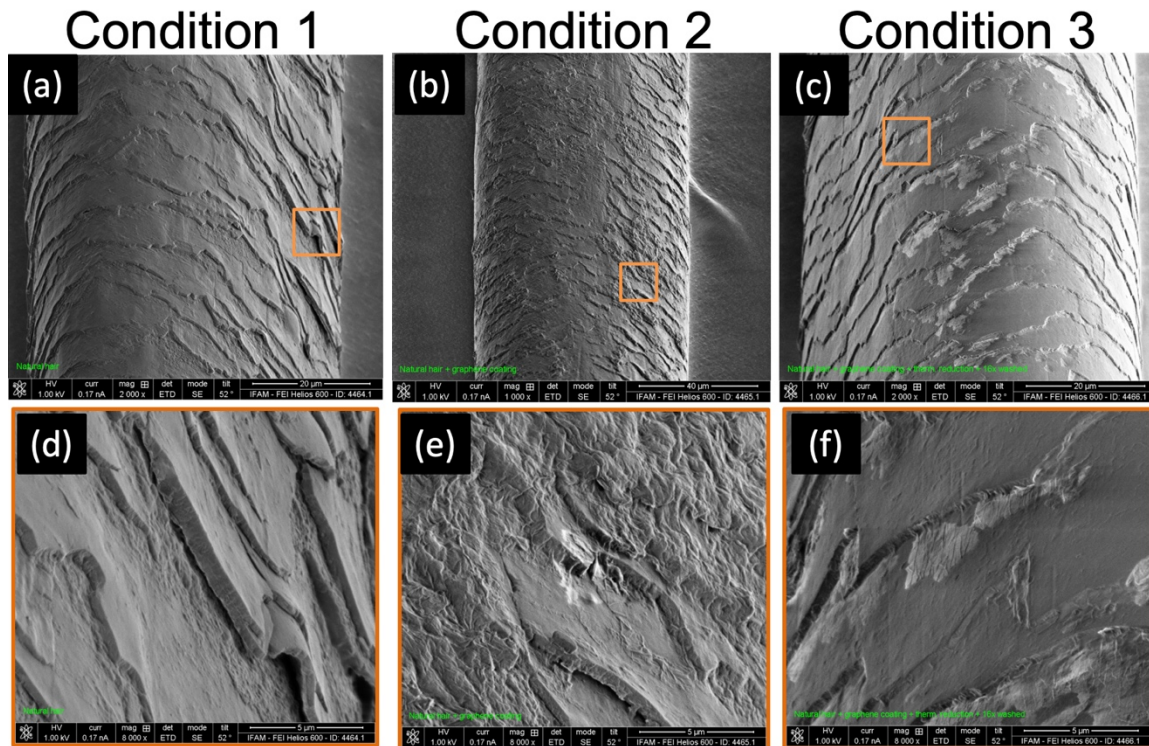
Figure 53 - SEM images of human hair in three conditions; (a, b and c represent conditions 1 to 3, respectively). Condition 1 is virgin hair, condition 2 is virgin hair treated with $(GO/BSA)_1$, and Condition 3 is virgin hair treated with $(rGO/BSA)_1$ and washed with shampoo for 16 times. Figures d, e and f are augmented areas of a, b and c, respectively.

In the augmented scanned areas (Figure 53d-f) it is observed that the hair scales have different microstructures between the three conditions. In condition 1, it can be

observed that occasionally a scale arranges itself with a gap to the lower scale (evidenced in the center of Figure 53d). These gaps are more common in worn hair[159], which is consistent with the evaluated region (approximately 1.4 years old, for hair 20 cm from the root[150]). Besides these gaps, there are also rough areas observed near the scale edges, probably being remnant parts from the upper scale after wearing[171].

After the coating process (Figure 53e), it is observed that some regions of the surface receive a coating with a roughed aspect (upper right part of Figure 53e). In other regions (lower part of Figure 53e) lower roughness is found. It is not clear if on that region (GO/BSA)$_1$ coating is present, however typical 2D aspects of rGO are observed in the center of the smooth area. The third aspect of condition 2 is the fact that the coating appears[1] to be bridging gaps from the scale edges (center of Figure 53e, bright area).

The third condition (Figure 53c and f), depicts effects from the thermal reduction and the extensive series of washing procedures. Overall the hair appears to be smoother, similar to condition 1. The effect of the coating forming "bridges" (covering the gaps between two scales) is still apparent. Lastly, the third visible distinction in condition 3 is that some brighter areas are observed immediately below the scale edges.

SEM characterization is sensitive to electrical conductivity, and more conductive areas are revealed with higher brightness. The samples for this SEM characterization were not prepared with conductive metal coatings; therefore, the brightness contrasts stem from the own surface electrical properties. High contrasts regions are not typically found on conditions 1 and 2; such result is expected, since in these conditions only organic matter and GO should be present (such materials are natural insulators). However, in the case of condition 3, it is expected that the SEM detects high contrast areas, assuming that some areas still contain the electrically conductive (rGO/BSA)$_1$ layer. Those areas of high contrast are indeed found, but immediately below the scale edges (Figure 53f); hence, it appears that the (rGO/BSA)$_1$ coating has a higher proclivity to attach and remaining on such areas next to the scales.

The bright areas where (rGO/BSA)$_1$ is detected coincide with the fractured regions of the scales, where the endocuticle is exposed. Differently from the lipidic surface of new hair, the composition of the endocuticle is largely proteinaceous[171]. This observation points to the fact that (rGO/BSA)$_1$, when used as hair cosmetic, tends to remain on the damaged areas of the hair, changing the surface from proteinaceous towards a graphene-like surface.

3.3.2 Combability (combing ease)

An important characterization to consider when developing a new hair cosmetic is the difference in the force required to comb the hair after the cosmetic treatment. Such

---

[1] Opinion endorsed by specialists in the area. The evaluation of the "scale bridging effect" requires extensive experience on hair cosmetics, therefore the author also considered feedback from professional cosmeticians with expertise on hair characterization to claim such statement.

characterization is objectively measured by a technique named Combing Ease. The test measures the forces required to align hair strands. The most common treatment that reduces the friction of hair is the use of conditioners; commonly, such products may reduce combing forces of dry hair by half[152,172–174]. The main factors driving the total force required to comb an assembly of hair are curvature (C), friction (F) and stiffness (S) of the hair[175]. The empirical model[175,176] that reliably (r^2=0.96) predicts peak combing load (PCL) among several types of hair is:

$$\log(PCL) = 0.0057 \times C^2 + 1.48 \times F - 0.05 \times S + 1.66$$

For this test, a 13 cm, 1 g weft of straight Caucasian hair was used to measure the changes in friction after its treatment with (rGO/BSA)$_1$. The test was conducted after a standardized shampoo washing and subsequent natural drying (the control sample was also washed and dried in same conditions). The hair was held perpendicular to the ground with its ends downwards. The comb used had 25 teeth in a 2 cm wide space where the hair was evenly distributed. The universal mechanical testing machine (TA·XTplus 5 kg load cell) pulled the hair up with a rate of 5 mm/s. The first and second combing passes were recorded. The results and summary are displayed on Figure 54.
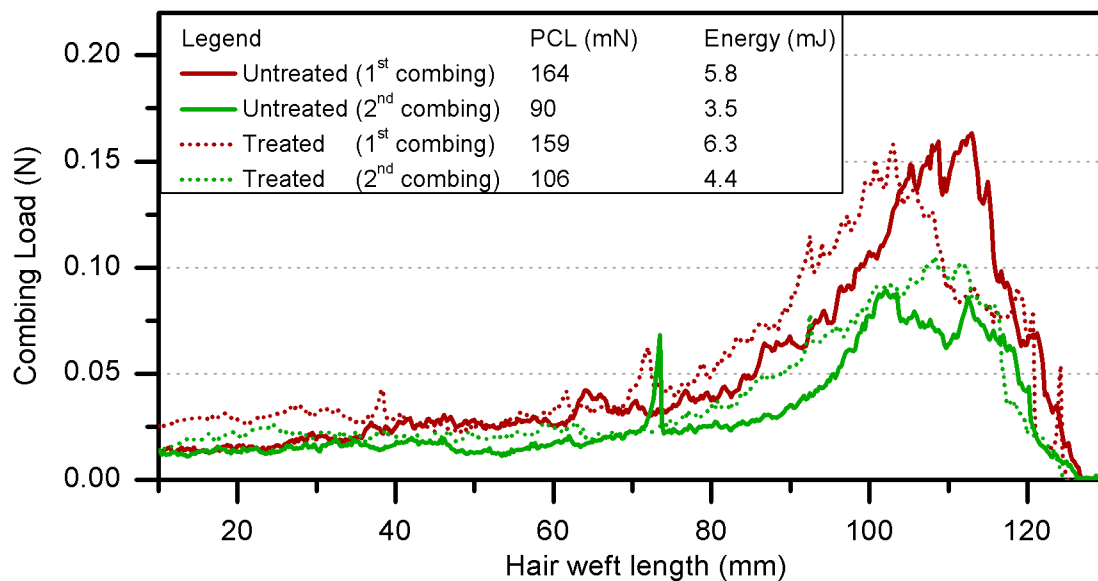
Figure 54 - Combing force loads of hair samples in two conditions; untreated and treated with (rGO/BSA)$_1$. The first combings are represented in red, and second combings in green. Dotted lines represent treated sample, and full lines represent untreated virgin hair. Both treated and untreated samples were washed and dried using the same procedure before the testing.

The results indicate that more forces are required to comb the hair after the treatment, both on first and second combing passes. The energies necessary to overcome the combing resistance are higher, it is required an extra 8.6 % of energy to comb the same hair in the first pass, and the second pass requires extra 26 % as when compared to a second pass without the hair treatment. Given that the treatment with

(rGO/BSA)$_1$ does not introduce changes to hair curvature[1] nor to stiffness[2], this combing test reveals mainly the changes on the hair surface friction (*F* as depicted on the previous equation above in this subchapter).

The combing ease after the application of (rGO/BSA)$_1$ may be reduced as a result of the excess of coating on the hair, which presents itself in a rough topography as indicated in Figure 53e. However, following the conjecture from the previous section[3], it is expected that the combing forces may ultimately lead to a reduction of combing forces over further washing procedures, as the graphene-like coatings end up replacing more specifically the areas of endocuticles debris. The friction of both materials (endocuticle and rGO) have been characterized in other studies using AFM nanoscratching[4]. The coefficient of friction of the endocuticle is roughly three times higher[177] than that of rGO[85], with $\mu_{endocuticle} = 0.072$ and $\mu_{rGO} = 0.026$.

3.3.3 Electrical conductivity and the flyaway effect

Human hair is an electrically insulating material[178]; its core consists of keratin-rich structures, and its surface consists of a thin monolayer of a lipid (18-MEA). Both parts ensure the high impedance property of hair. However, upon higher humidity, human hair swells and incorporates water in its structure, allowing higher carrier mobility[179]. The electrical behavior of human hair is described as a universal AC conductor[179,180], characterized by (i) low dependence of conductance in low frequencies regime and, (ii) unclear carrier contribution ratio of ionic/electronic conduction[180]. A recent study[181] further clarified that the organic structures of hair (namely proteins and carbohydrates) allow adsorbed water to mediate polaron-like complexes that can transport electrons.

Besides having a high electrical impedance, the surface of human hair has a high bias towards being positively charged upon rubbing against other materials, in fact, it is often ranked among the materials with the highest positive triboelectricity bias[182–184]. Recently, researchers[183] took advantage of this characteristic and demonstrated that human hair can be dissolved into a mixture and applied as films in order to produce cheap, efficient, positive tribo-materials for electric nanogenerators.

However, a mundane consequence of this surface property is that hair becomes electrically charged when rubbed against other materials, like neighboring hairs,

---

[1] Hair after treatment remained straight, no curvature before nor after.

[2] By supporting a 5 cm piece of hair in a single point, no change in deflection was observed in hair before and after treatment. Hence the same stiffness values for the samples were assumed.

[3] It was conjectured, evaluating results from Figure 53 SEM images, that after numerous washing procedures the coating treatment remains particularly well on areas where debris of cuticles are found.

[4] For hair endocuticle[177], the indentation was done with 40 nm Si$_3$N$_4$ ball with loads up to 40 nN. For rGO[85] the indentations was done with a 60 nm Si$_3$N$_4$ ball with loads up to 40 nN.

combs, and fabrics. Moreover, combined with high electric insulation, such charges tend to remain on the hair fibers and repeal each other, resulting in "flyaway" hair. In the field of hair cosmetics often new products and inventions claim to offer "antistatic" effects to address this phenomenon, this effect is achieved by changing the characteristics on the hair surface. Such solutions either (i) add lubricating materials on hair, thereby reducing friction and generation of charges when rubbed against other materials[175,185] and/or (ii) add electrically conductive materials on hair, like long-chain quaternary ammonium salts, PDMS silicone or amino silicone.[175,185–187]

Typically, researchers may employ several methods to measure the change in the triboelectricity of hair. Local measurements of surface charge can be detected with Kelvin Probe[185,188,189] and Scanning Ion Conductance Microscopy[188]. In the macroscopic scale, hair triboelectricity can be measured with specials combs[175] and alternatively, one can infer the change in triboelectricity by visual inspection of images where hair manifests flyaway effect after controlled rubbing. Upon extensive literature and patent review, no simple quantification of hair electrical conductivity was reported (S/cm/hair). Due to limited access to the devices mentioned above, and aiming for a straight-forward measurement, here it is reported the direct electrical properties of hair that can be measured with a universal multimeter (details of the experiment in materials and methods section).

Caucasian human hair's electrical conductivity was measured before and after treatment with (rGO/BSA)$_1$. The electrical resistance of virgin hair exceeded the sensitive range in the experiment set up and was assumed to be in the range between $10^{-14.8}$ to $10^{-15.5}$ S/(hair.cm) as measured by Abie *et al.*[179]. Hair treated by (rGO/BSA)$_1$ renders an electrical conductivity of $10^{-8.0}$ S/(hair.cm), seven orders of magnitude higher than virgin hair. This extreme change in electrical conductivity is ascribed solely to the rGO now present on the hair, as the effect of temperature alone did not render electrical conductivity on temperature-treated virgin hair. The treatment with (rGO/BSA)$_1$ is, therefore, acting as a thin film with conductive characteristics on human hair.

In the field of antistatic coatings, it is adopted[190] a specific nomenclature in order to qualify a coating as "antistatic", "static dissipative" or "conductive", as detailed in the right axis of Figure 55. The relevant unity to consider is sheet resistance, given in Ohm/square. Considering an average diameter of 60 µm for each hair fiber, the figure of $10^{-8.0}$ S/(hair.cm) converts into the sheet resistance value of $10^{6.8}$ Ohm/square. For the interest of better discussing the results, other key materials were plotted as a reference.

The result qualifies (rGO/BSA)$_1$ as a "static dissipative" coating when used on hair. Such a range of value suffices not only to avoid concentration of charges but also it does allow for quick charge dissipation. In contrast, a commercial anti-static

component (3,4-polyethylene-dioxythiophene) used in antistatic conditioners is expected[1] to deliver conductivities that qualifies it as an antistatic coating.

There is, however, a deterioration in electrical conductivity when $(rGO/BSA)_1$ is deposited on human hair instead of quartz. The conductivity of the coating $(rGO/BSA)_1$ is lower on hair by a factor of 3.6; such result is probably due to the lower temperature of reduction and shorter time of reduction (225ºC for 5 minutes on human hair and 250ºC on quartz, for 20 minutes). The sheet resistance of pure graphene indicates the range of theoretical limit that could be achieved for $(GO/BSA)_1$ in a perfect chemical healing and conversion towards graphene, however, compromises for safety reasons and practicality probably play a role.
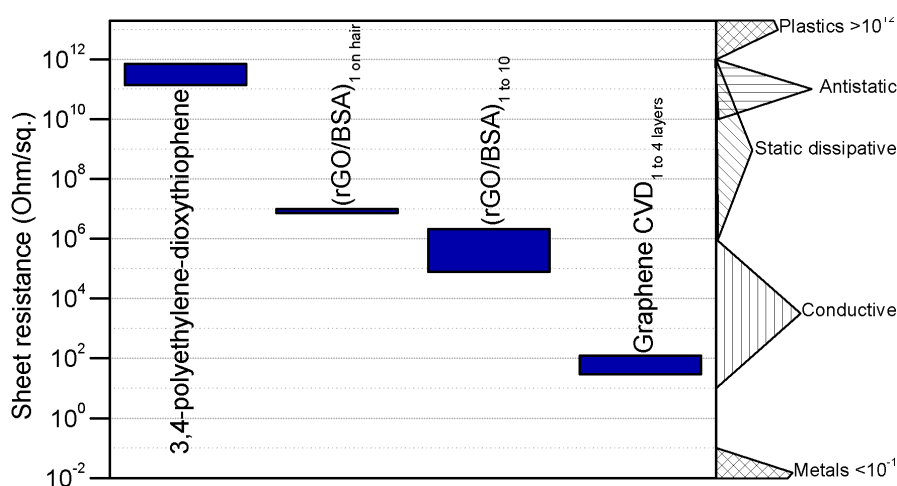
Figure 55 - Electrical property (sheet resistance) of different coatings, including the coatings investigated in this research and reference values. From left to right: the first component is an antistatic compound used in cosmetics, the second is the actual measurement of electrical resistivity of hair after the application of $(rGO/BSA)_1$. The third range of values is from the samples where the coating is deposited on quartz (more details in chapter 2). Lastly, it is plotted the values of sheet resistance in the case pure graphene was applied on human hair.

As mentioned before, the interest in electrical properties of hair is due to its implications in hair manageability. In practical terms, the low sheet resistance translates into less hair that flies away after being rubbed in a controlled way, i.e. after a triboelectric test. Samples of human hair (virgin and treated with $(rGO/BSA)_1$), were tested for the tendency of building electric charges upon rubbing against a rubber balloon.

---

[1] From the literature[268], it is provided that the conductivity of such component is 10^{-5} S/cm and it was assumed[269] that the typical thickness of conditioner deposition on hair is between 1.4 and 7.2 nm.
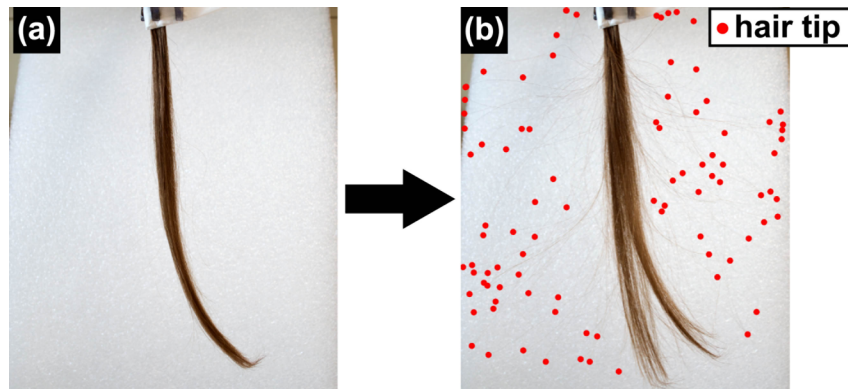
Figure 56 – Manifestation of flyaway hair. (a) virgin hair (washed and naturally dried under 50%RH) slowly combed does not manifest flyaway effect and (b) same sample as (a) but rubbed against a balloon. In (b) the red dots highlight the location of hair tips (distal ends).

The triboelectric test of virgin human hair (Figure 56) results in the vast spread of the hair tips from the main body ("hair ballooning" effect), as depicted with red dots in Figure 56b.

That very sample from Figure 56 was further treated with $(rGO/BSA)_1$ and tested with the triboelectric procedure. In Figure 57 a sequence of pictures from the sample in five advancing states is shown: from virgin (a), to treated (b) and tested for fly away effect (c to e). The triboelectric test in the "just treated" sample (Figure 57c) yielded substantially less flyaway effect in comparison to virgin hair (Figure 56b). Interestingly, washing the sample further resulted in less hair flyaway (Figure 57d and e). The simple justification for Figure 57c showing more flyaway effect than Figure 57e is that the $(rGO/BSA)_1$ treatment is executed in extremely dry conditions (closed atmosphere with N_2 feed) and at high temperature (215^oC), priming the hair to have less adsorbed water on the condition "just treated". Under such dry conditions, hair tends to build electric charges more easily upon rubbing[175].
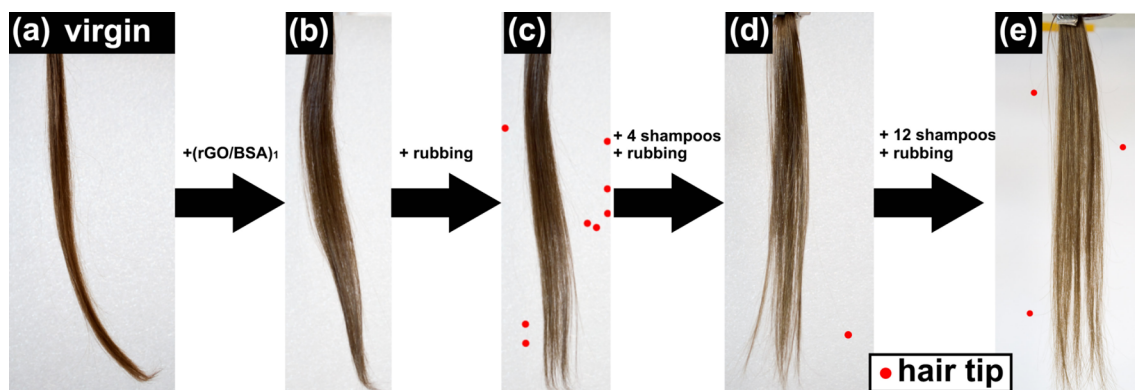
Figure 57 - (a) Virgin hair, (b) sample shown on (a) after treatment with $(rGO/BSA)_1$. (c-e) Hair ballooning as a result of controlled triboelectric exposure of hair (rubbing) in three conditions, following descriptions above arrows. (c) Hair treated with $(rGO/BSA)_1$ exposed to rubbing test. (d) shows sample in (c) after 4 washing procedures (shampoos) and rubbing procedure. (e) shows sample in (d) washed further 12 times and after rubbing procedure. The red dots in images (c-e) represent the location of hair tips that are not parallel to the hair group.

The absolute change in terms of the number of unruly flyaway single hair strands changed from 90 (virgin state Figure 56b) to 8 (just treated state Figure 57c). The count is further lowered to 1 and 3, after 4 and 16 washes, respectively. This result

alludes to the fact that after the washing processes, there is still enough conductive material on the hair allowing discharge of electrons after the rubbing test. This result is in line with the observation of rGO structures on the microscope images (Figure 53f).

3.3.4 Color effect

One of the most important aspects of hair is its color. The market size worldwide for hair coloring is over 18 BU\$D[191] and tends to grow due to the aging population[165]. The field of hair coloring is categorized by the duration of coloring effect; permanent (not removed in normal conditions), semi-permanent (lasts over 6 shampoos) and temporary (not shampoo resistant)[165].

As it was characterized in the first part of this work (subchapter 2.2.2), rGOBio$_{nanocoating}$ does play a role in the light transmission in the visible spectrum; therefore, it is necessary to quantify in detail the color change it brings about among different hair colors. Also, it is fundamental to characterize the persistence of coloring effect throughout shampooing processes and therefore classify the treatment as permanent, semi-permanent, or temporary.

The color acquisition was made by using a scanner (further details are described in materials and methods), which outputs an RGB color map. However, for color characterization in the cosmetic field an RGB is replaced by a color scheme named CIE*L*a*b**[192]. The CIE*L*a*b** model is used as a proxy for the human color perception, allowing a more linear color characterization. The CIE*L*a*b** has three color dimensions (*L**, *a**, and *b**) which are commensurate with the logarithmic response of light to the rods and cones from the human eye[192,193]; *L** is the color lightness and scales from 0 to 100, a* and b* parameters are independent and range from -100 to +100. Another useful information from this system is that any unity change on any of these three dimensions approaches the limit of color distinction for the human eye[192].

In order to represent the three dimensions color aspect of the hair and its distribution, two 2D-projections are plotted as it is an adequate approach for the print form. The overall methodology is depicted in Figure 58 and described in more detail at the materials and methods section. Briefly, a hair sample is scanned, and after color calibration, the pixels are measured in the CIE*L*a*b** system, where 2D-plots of *L** vs *a** and *L** vs *b** are employed to show the color distribution.
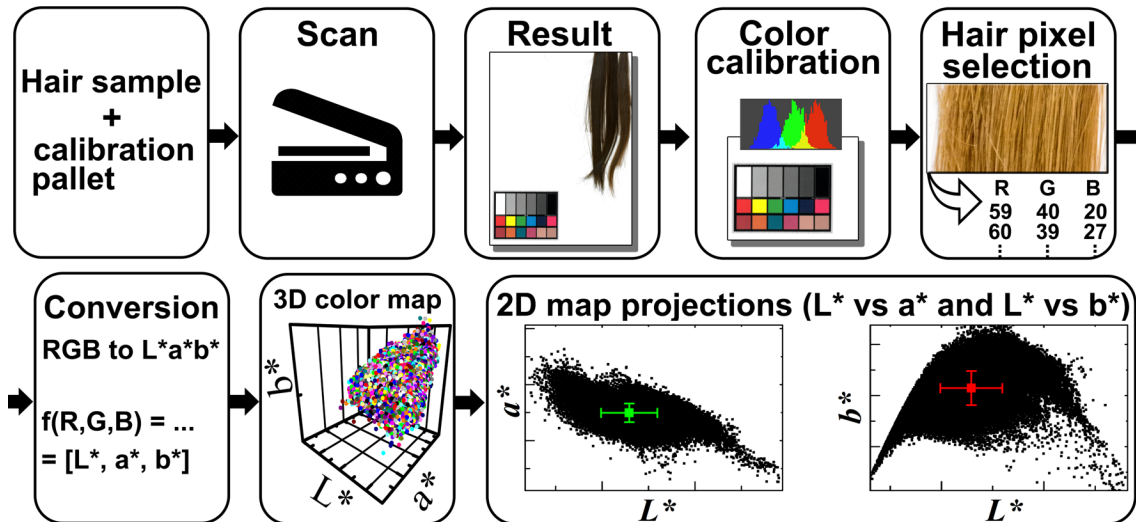
Figure 58 - Methodology for acquiring color information of human hair. First, hair is scanned in the presence of a calibration color pallet. The picture is color corrected using the standard pallet. Then, the RGB pixel values of the sample area are acquired and considered to be the hair colors. The data from the RGB map is converted to CIEL*a*b* dimensions and plotted in two 2D plots of L* vs. a* and L* vs. b*. Average and standard deviations (here represented in green and red on the last block) are plotted to represent the distribution of colors for each sample.

Four different hair colors were characterized (using the above-mentioned procedure) in their virgin state and after treatment with (rGO/BSA)$_1$. The images of such samples are depicted in Figure 59. Upon simple visual inspection, the color transformation is pronounced on white and blonde hair in contrast to a modest to invisible difference in the brown and the black hair. Yet another observation is that the process (rGO/BSA)$_1$ transforms the hair colors into natural-looking shades (except for the white hair).

Figure 59 - Images of four different hair colors in their virgin and treated state. (a-d) On the left the virgin sample and followed by an arrow, the coloring effect. The length of free hair is 13 cm and each sample weights 0.4g (+/- 0.05g of tolerance). The color codes were provided by the supplier of these samples (Kerling International).

Besides the visual inspection, Figure 60 shows the measurement of color distribution of such samples using the CIE*L*a*b** system. The three-color dimensions *L**, *a** and *b**, undergo a different transformation for the four samples, such transition is represented by arrows. The *L** (lightness) changes dramatically in the white hair, where it lowers 48 unities in the 0 to 100 scale. For the blonde hair, there is a significant intersection of *L** values; however, the average *L** is lowered by approximately 9 units.

66

The *L** dimension in brown and black hairs is not significantly changed, undergoing less than 1 unity in the *L** scale.

The parameter *a** (transition from green to red) shows only minute changes in all four samples, below 2 unities (in the scale from -100 to +100). Lastly, the parameter *b** (transition from blue to yellow) changes 13 unities in white hair; for the other colors the change in b* is below 4 units (in the scale from -100 to +100). As these numbers are linear to the human perception and +-1 is the limit of distinction, it can be stated that the treatment with (rGO/BSA)$_1$ plays an essential role in the L* dimension, but not in *a** and *b** dimensions.
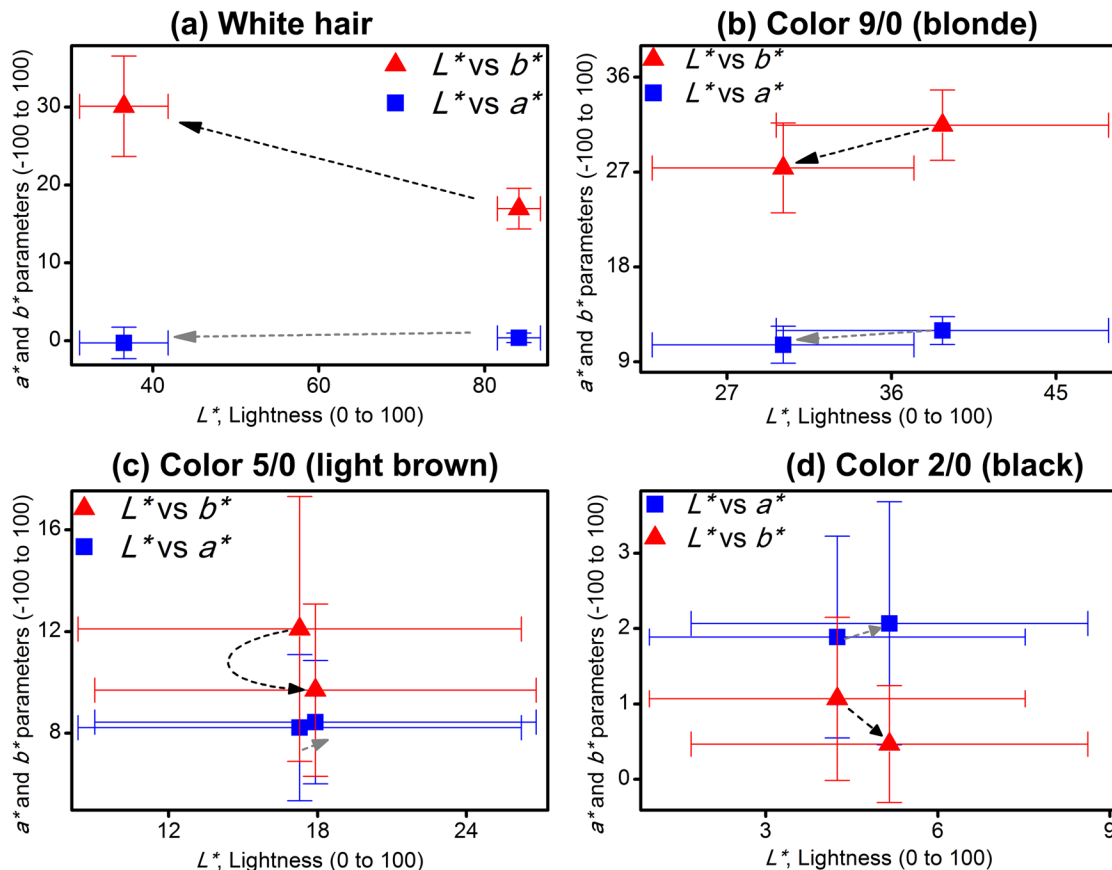
Figure 60 - Hair color change after the application of (rGO/BSA)$_1$, following the methodology described in materials and methods. (a-d) The distribution of colors is represented by average (triangles and squares) and their standard deviations. The black dashed arrow represents the transition in the L* vs. b* space from the virgin hair towards the treated hair. The grey dashed arrows represent the transition in the L* vs. a* space from virgin hair towards the treated hair. Note that only in white hair there is no overlapping of colors after the treatment; for the 3 darker samples there is a large intersection of colors comparing the before and after treatment state.

These transitions from different hair colors can also be represented as vectors in a *L** vs. *a** and *L** vs *b** color spaces, as depicted in Figure 61. This representation is useful to describe the overall trend and predict outcomes from intermediate hair colors. As evident in Figure 61a, the vectors tend to transition towards lower L* and lower a*. It can also be interpreted that the green-red color aspect of the hair undergoes little change in the green-red color characteristic (*a**), but rather these colors undergo a greater change in their lightness aspect, particularly if starting from a higher lightness. As for the vectors in the *L** vs *b** space (Figure 61b), it can be described that the blue to the yellow color aspect (*b**) is increased for white hair exclusively but undergoes a modest reduction for all other samples investigated (blonde and darker).

Since most human hair colors are darker than the blonde investigated here (color 9/0)[194], it may be predicted that intermediate hair colors (form blonde to black) undergo color change towards lower lightness (*L**), but not higher than 10 units. As for *a** and *b** color aspects, no significant changes are to be expected.
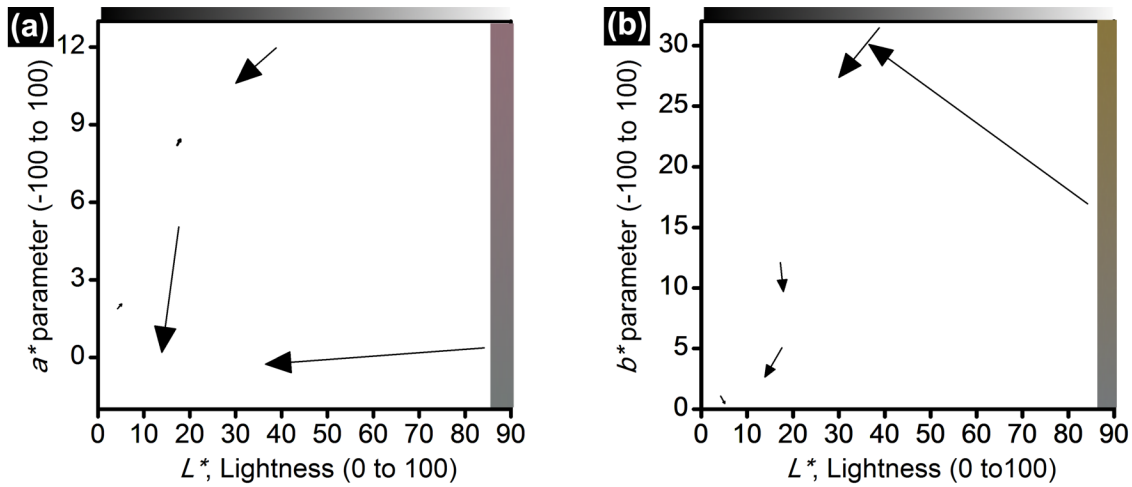
Figure 61 – Hair color change represented with vectors in the L* vs. a* and L* vs. b* spaces. (a-b) Charts are also furnished with the continuum color change in the ranges represented in the charts. Human limit perception for each axis (L*, a* or b*) is 1 unit. The total color change is proportional to the vector sizes. For (a) and (b) the significant changes after treatment is in the L* axis, particularly when stemming from higher values.

Besides the immediate color transformation caused by the treatment with (rGO/BSA)$_1$, the assessment of treatment duration was also measured. A sample of dark blonde was treated with the process and washed twelve times. Color measurements were carried out from the virgin state and intermediate states until the twelfth wash (Figure 62).
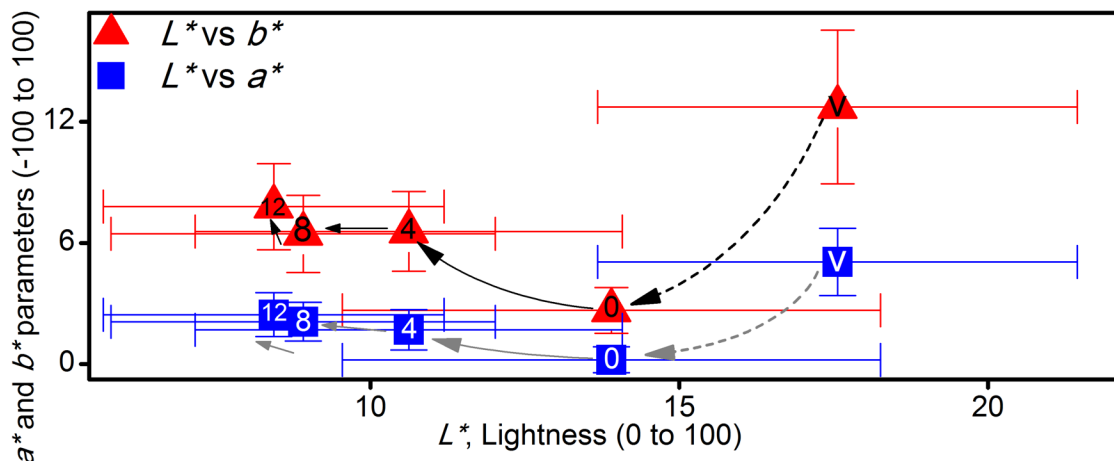
Figure 62 - Color change in human hair, from virgin state (v) to treated and washed. The numbers inside the symbols represent the number of times that hair was washed after the treatment with (rGO/BSA)$_1$. The dashed arrows represent the transformation from virgin to treated state on both L* vs. a* and L* vs. b* color spaces. The arrows with full lines represent the advancement of states (from 0th to 12th wash). Note that considering the standard deviations hair color does not change significantly from state o 8 to 12 washes, possibly indicating stagnation.

In Figure 62, the color evolution from virgin state (v) to the twelfth wash (12) has an evolution such that *L** values are lowered by the treatment with (rGO/BSA)$_1$ and also further lowered by shampoo washing processes. The *a** and *b** color parameter, as mentioned above, shows small change for this dark tone of blonde. This small change

in *a** and *b** dimensions is partially restored to near original values after the washing sequence.

In order to account for the independent effects of temperature exposure (during the thermal cycle of $(rGO/BSA)_1$ process) and washing, a control experiment was conducted. Such sample was measured in its original state (virgin), after exposure to temperature treatment (without application of $(GO/BSA)_1$) coating and after sequential washings in order to narrow the causation of the color change (Figure 63). The tests assert whether the color change is necessarily caused by the coating and not exposure to temperature and further washings. The result of the control experiment shows a large overlapping of colors during the twelve washing procedures and the original virgin state. Also, no bias towards moving the color distribution towards a different range was observed. Such overlapping indicates that the color change is not caused by washing and/or temperature exposure, and indeed by the treatment with $(rGO/BSA)_1$.
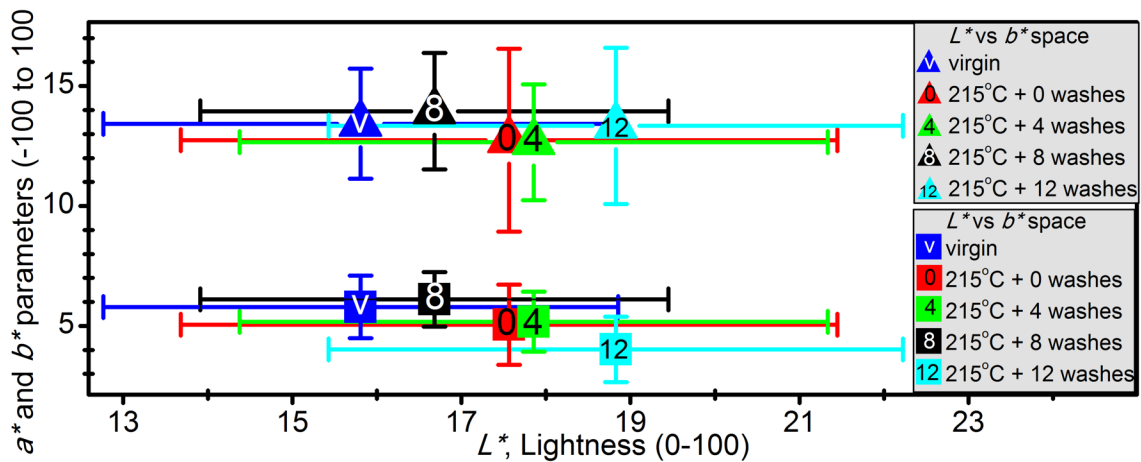
Figure 63 - Color change in virgin hair before and through 12 washing procedures. In all three-color dimensions (L*, a* and b*); no substantial change in the distribution of pixels values is observed nor a trend to shift the color to one or another direction throughout the washing procedures.

Furnished with such results, the category name that properly fits the $(rGO/BSA)_1$ treatment is "permanent", as the color is not restored to the original color after the sequence of washing.

3.3.5 Mechanical test

A further method to assess changes caused by the treatment with $(rGO/BSA)_1$ is by conducting a rupture test on a universal mechanical machine in the conditions of before and after treatment. Several pieces of information can be captured in this test; force at rupture, tenacity, elastic modulus, elastic limit, and turnover point. The force at rupture and maximum elongation are more abundantly published in the field of hair fiber studies.

The exposure of hair to different conditions plays a role in the total strength of chemical bonds of the hair fibers to a greater or lower degree. For example, upon exposure to hair bleaching, one study found a significant reduction of 32% in the breaking strength

compared to the control sample[1] (virgin condition)[195]. However, in two other studies with milder conditions of bleaching, no statistical difference in the rupture stress was observed[196,197]. A similar breadth of results is found in terms of the effects of photoirradiation (from UV to IR) on breaking strength of human hair[198], but in general long exposure to irradiation does tend to damage the mechanical properties of human hair due to the breakage of disulfide bonds and protein degradation.[198]

Besides chemical and photoirradiation exposure, hair can further be exposed to high temperatures, particularly during cosmetic procedures like hair straightening/curling (range of 110 to 250°C)[199–201] or blow-drying (up to 140°C)[202]. The use of high temperature during these grooming procedures may cause alteration of mechanical properties, and in general, the higher temperatures have more impact, especially when approaching the denaturation and pyrolysis ranges at ~230°C.[203] However, other factors in combination with the temperature will play a role in changing the mechanical properties of hair, like: type of hair[204], frequency of heating cycles[152,204,205], stress and moisture applied during heat exposure[199,206] and use of heat protection[207].

The application of $(GO/BSA)_1$ on human hair and the following thermal reduction requires subjecting the hair to low pH media and then exposing it to a relatively high temperature of 215°C. In order to assess whether these chemical and thermal attacks cause mechanical damage to hair, mechanical testing was conducted on both virgin hair and hair treated with $(rGO/BSA)_1$. The results of the stress at rupture and strain at rupture are presented in Figure 64.
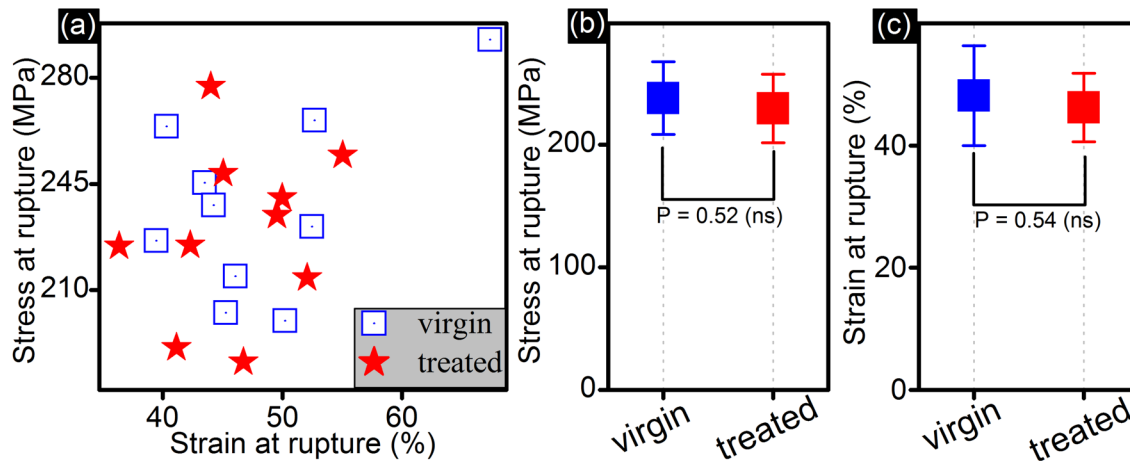
Figure 64 - Mechanical properties of hair before and after treatment with $(rGO/BSA)_1$. (a) Plot of data recorded at hair rupture; in x-axis the strain relative to the original size of hair and in the y-axis engineer stress resisted by the fiber at such moment (which is also the highest during the test). (b) Plot of stress average and standard deviation for virgin and treated hair (p-value at α = 0.05 show not significant (ns) difference). (c) Plot of strain average and standard deviation at rupture in virgin and treated hair (p-value at α = 0.05 show not significant (ns) difference).

---

[1] With significant statistical confidence P-Value << 0.05. The P-Value was calculated based on sample size and estimation for standard deviation. Standard deviation was considered to be ¾ of the space between the first and third quartile of the boxplot.

The sample was provided by a female Caucasian volunteer with straight blonde hair. Distance from the scalp approx. 50 cm and sample size between 5 and 6 cm.

The mechanical properties (stress and strain at rupture) are not significantly altered between the untreated (virgin) samples and the treated samples, showing values in similar ranges (as observed in scattered results from Figure 64a, showing overlapping clusters of data). The summary of both properties with average, standard deviations, and significance are displayed in Figure 64b and c. Despite the relatively small sample size (N=10), a t-test for these distributions indicated no significant (ns) change of values after the (rGO/BSA)$_1$ treatment. The averages and standard deviations of the stress of rupture and strain at rupture are in a typical range for Caucasian hair and observed elsewhere[208,209].

The fact that no significant changes are observed despite the exposure to acidic media and the high temperature opens the discussion to the factors that could be at work for this result. The following paragraphs explore the potentially relevant factors that either toughen or impair the hair strength.

3.3.5.1 Chemical exposure during dipping processes

As described on the materials and methods, the process to apply (GO/BSA)$_1$ on human hair requires dipping it into a buffer solution with BSA at pH 4.75 and later GO dispersion at pH ~2.6. The first media is mildly acidic, but in the range of typical shampoos[210] and not damaging[209]. The second pH despite being acidic it is not far from the isoelectric point of hair (pH 3.7) and not inherently destructive for the mechanical properties of hair[209], particularly over short periods of time and low temperature[152] (which are the conditions for applying (GO/BSA)$_1$). The chemical exposure probably does not play a role in the resulting mechanical properties of hair.

3.3.5.2 Strengthening effect of BSA

Ribeiro *et al.*[211] discovered the use of a hydrolyzed protein (PDB: 1HK0) that can recover the mechanical properties of bleached hair. Briefly: virgin hair Young's modulus (E_{virgin}) is strongly reduced after a succession of eight bleaching processes (modulus reduced to 85% × E_{virgin}) and after the treatment devised by them the Young modulus recovers above the original value of virgin hair, to 136% × E_{virgin}. The researchers[211] also conducted a control experiment with BSA (instead of the hydrolyzed protein 1HK0), to find that BSA recovered the young modulus to 99% × E_{virgin}. In terms of tensile strength (σ_{virgin}), bleached hair has 77% of σ_{virgin}, hair recovered with BSA has 96% of σ_{virgin}.

There are some limitations to extrapolate the effects on the use of BSA in our case since those researchers apply it on bleach-damaged hair. Bleaching creates cracks, holes, and scale lifting, which allow higher penetration of proteins. On the other hand, the experiments with (GO/BSA)$_1$ are done in virgin hair (not bleached), providing fewer opportunities for protein penetration due to the closed hair scales. However, two supporting arguments provide evidence that BSA provides some strengthening of human hair. First, the researchers concluded that a critical aspect of healing the hair properties is the size of the protein and observed that BSA does not penetrate the hair shaft even after the bleaching; meaning that BSA provides some healing by being on

the hair surface. Second, the researchers used an alkaline pH for the BSA adsorption (pH 8.0), which is far from the ideal pH for maximum adsorption of the protein on an acidic surface like hair[94].

3.3.5.3 Number of thermal cycles and source of heat

Based on a recent research[205], it was found that the number of thermal cycles has a cumulative detrimental effect on hair; 15-second cycles at 180°C (amassing to the total exposure of 0 to 20 minutes), result in increasing deterioration of strain at break and breaking stress of hair. The authors established that multiple thermal cycles induce cumulative damages in and on the hair scales as well as between the scales interface.

Also, it can be the case that the source of heat played a role since in this study[205] the hair absorbs the heat through direct contact with hot iron plate and not through the air (as in the case of $(rGO/BSA)_1$ treatment). The direct contact with the metallic interface can increase the temperature gradient and augment the proclivity of explosive release of steam trapped in the hair[199].

3.3.6 TGA

Thermogravimetric analysis (TGA) of human hair is a useful tool to observe how cosmetic products influence the moisture dynamics and decomposition of hair upon heating. The method is useful to substantiate claims regarding protection and repair of hair against thermal exposure (for example while straightening the hair)[207,212,213] and also provide temperature ranges that are appropriate for different kinds of hair[214].

Fundamentally, TGA measures the change of weight of a hair sample across a temperature cycle (typically a few mg of hair cut in mm pieces on a metallic tray). Such change in weight is related to water desorption (below 180°C) and later to thermal decomposition (above 180°C)[215]. Barba *et al.*[215] distinguished that the water in human hair (~15% of hair total mass) is embedded in "external" and "internal" structures; the external structures hold roughly 75% of the total water and can be removed by exposing hair to 65°C for 40 minutes, on the other hand, the remaining 25% of water content is attached internally and can be released in 30 minutes at 180°C.

The thermal decomposition of hair starts slowly at 170°C and evolves to maximum peaks of weight loss at 276°C and later at 305°C; the first maximum is a marker for the formation of inorganic gases (NH_3, CO_2, SCS, SCO, H_2S, and SO_2) and thiols, the second maxima is related to the substantial degradation and release of nitriles and aromatics[216]. Exothermic processes, which probably include oxidative ones, do not commence until 235°C and have peaks at 253°C, 303°C, and 565°C.[214]

In this research, TGA was done on Caucasian hair in two conditions, virgin and treated with $(GO/BSA)_1$. Both samples followed the same thermal cycle that is applied to transform $(GO/BSA)_1$ on $(rGO/BSA)_1$. Briefly, conditioned hair (kept for 24h at 50%RH and 20°C) is heated at 10K/min from room temperature to 215°C, at which stage it is kept isothermally for 5 minutes and brought quickly to room temperature conditions. The TGA of both samples is presented in Figure 65 with a further reference value from the literature[215] (same thermal cycle until 215°C).
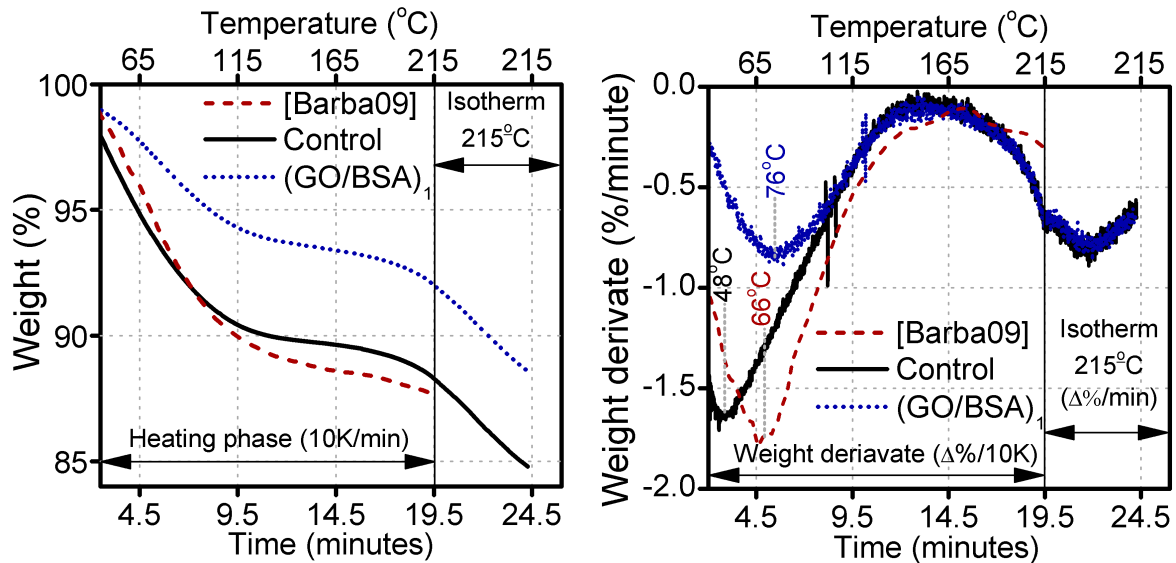
Figure 65 - TGA of Caucasian human hair in two conditions; virgin and treated with (GO/BSA)₁. (a) Weight evolution over thermal cycle (10K/min from 20°C to 215°C, 5 minutes hold at 215°C and return to room temperature). (b) weight from data in chart (a) differentiated over time (in the heating phase, the differentiation over temperature unit is 10 times lower due to 10K/min rate).

The control experiment in Figure 65 shows similar results to Barba *et al.*[215]. Comparing the weight losses in Figure 65a both samples lose roughly 12% of total mass lost until 215°C. When comparing both (control and ref.[215]) in terms of the derivate weight loss (Figure 65b) both show maximum loss rate of approximately -0.16%/K (or -1.6%/min at 10K/min heating) and a stable plateau with minute weight loss at 160°C before initiation of further mass loss. The position of the first peak of weight loss, however, is higher for ref.[215] at 66°C than in the control experiment at 48°C. The range of these rates, peak position, and plateau, are expected in control experiments of Caucasian hair and observed elsewhere[213,214,216–218].

Besides these control experiments, the third result plotted in Figure 65 in blue dots refers to the TGA of hair (from the same batch of the control experiment) pre-treated with (GO/BSA)₁. The exposure to the thermal cycle in the treated hair results in a remarkably distinct mass loss behavior. From Figure 65a it can be observed that the heating up to 215°C results in 8% of weight loss for the hair coated with (GO/BSA)₁ instead of 12% for the control experiment. Additional five minutes exposure to the isothermal phase (215°C) reduce further ~3.5% of mass in both samples, resulting in total mass loss of 11.4% (for coated sample) instead of 15.2% for the control experiment.

An extended analysis with the weight differentiation (Figure 65b) reveals further information of the thermal process in the treated hair; that is, the peak of water loss happens at 76°C, which is 28K higher than the control experiment and also higher than the typical peak position for virgin Caucasian hair (from 61°C to 66°C)[213–215,218]. Furthermore, in the heating cycle with the coated hair, the maximum water loss rate is approximately half of that for the control experiment (-0.083%/K vs. -0.162%/K). This mass loss event ceases at ~160°C and the sample proceeds to lose weight in the same fashion as the control experiment; similar weight derivates until reaching 215°C and throughout the five minutes isotherm at 215°C (blue and black curves in Figure 65b).

The contrasting difference of the first weight loss peak (in size and position) arising from the hair treatment with (GO/BSA)$_1$ can be interpreted with three hypotheses;

(i) the exposure to acidic media during application of (GO/BSA)$_1$ provides thermal stability of the hair and/or

(ii) the exposure to acidic media during application of (GO/BSA)$_1$ process dehydrates the loosely bound water content in the hair, and/or

(iii) the coating (GO/BSA)$_1$ works as a water seal membrane and retards the water loss of hair upon heating.

The hypothesis (i) can be supported by the fact that in the process of applying (GO/BSA)$_1$ the hair is exposed to a buffer at pH 4.75 and later to an even lower pH of ~2.6 (when dipping into the GO dispersion). The exposure to such low acidic media stabilizes the hair fibers thermally, increasing the temperature of degradation by 5K. This effect is due to the strengthening of structural scaffolds of intermediate filaments in the hair core.[209]. Also, connected to this idea is the fact that at this low pH the hair scales remain tightly attached to the hair shaft, as opposed to opening the scales when exposed to alkaline pHs[210,219].

The hypothesis (ii) is not self-evident, as exposure to these low pH media, actually, results in water uptake in the hair, and not dehydration[152,220]. Such statement may be challenged, however, in the case that dissolved small particles[1] may modify the sorption of water. These components may play a role in penetrating the hair shaft and replacing the loosely bound water, which would then not be observed to be released on hair treated with (GO/BSA)$_1$ (check Figure 65b, blue curve).

And finally, hypothesis (iii) is related to the membrane-characteristics of (GO/BSA)$_1$, which could play a role in the water diffusion of human hair. The diffusion of water through (GO/BSA)$_1$ was not assessed in this research; however, an educated guess for diffusion based on similar coatings to the ones investigated here, indicates a range between 10^{-6} to 10^{-8} cm^2/s[221,222]. In contrast, when it comes to the diffusion of water at room temperature in virgin Caucasian hair (untrammeled by any coatings or pretreatment), the order of magnitude of water diffusion lies in the range from 10^{-10} to $10^{-8.5}$ cm^2/s[207,223]. This means that the difference of water diffusion on the graphene-based coating is at least 3 times quicker than the diffusion on hair (but possibly also thousands of times quicker). Despite of not having the precise values of water diffusion in our nanometric coatings, it is reasonable to state that most of the water diffusion is limited by the hair natural tight structures, not by the nanometrically thin (GO/BSA)$_1$. However, the nanocoating may hinder enough water diffusion to the extent that it causes the temperature peak shift and its attenuation, in other words, acting as a moisture loss retardant.

The combination of hypothesis (i), (ii) and (iii) could offer some clues to explain the low water loss in human hair and the temperature shift of water loss. However, no

---

[1] Particles below the 1 nm rage can easily penetrate the hair shaft[270]. The dissolved particles stemming from the buffer and the GO dispersion which fit this criterion (<1 nm) are: Na$^+$, CH$_3$COO$^-$, CH$_3$COOH, MnO$_4^-$, Mn^{2+}, K$^+$, SO$_4^{2-}$, HSO$_4^-$, NO$_3^-$, H$_3$O$^+$. Possibly aromatic debris from the GO could fit these criteria also[244].

conclusive evidence could be established to explain such low and delayed water desorption behavior. Further tests are required in order to draw further conclusions regarding the water dynamics of the coating.

3.3.7 Safety considerations

The characterization and interpretations discussed above are performed in *ex vivo* samples for safety reasons. However, it is imperative that cosmetic products be scrutinized for hazardous effects on humans. Ultimately, the cosmetic has to pass tests that are highly dependent on the country where it would be sold.

In the European Union (EU), for example, safety assessment in animal models phased out from 1993 to full ban in 2013[224] and in order to mitigate the challenges of abdicating from *in vivo* research, the EU invests in projects to develop *in vitro* alternatives[225] and keeps an updated list of alternatives for public consultation[226]. Each cosmetic product placed in the EU must be linked to a "responsible person" who ensures the safety of the product by submitting a safety report. Among other regulations, it is required that cosmetics containing nanomaterials include the word "nano" on the packaging[227].

In the United States, a more liberal approach towards *in vivo* tests is applied: The FDA agency (U.S. Food & Drug Administration) recommends the manufacturer "to employ whatever testing is appropriate and effective for substantiating the safety of their products". At the same time, the agency enforces regulations such as the Animal Welfare Act and advocates for a minimal number of animals and for the most humane methods available.[228] The manufacturer may even use data from scientific journals to substantiate the safety of ingredients that are used in the cosmetic.

On the other side of the spectrum, in China, regulations require animal testing to ensure safe use for humans[229]. However, increasingly more *in vitro* methods are being accepted as an alternative for cosmetic safety assessment[230].

Regardless of the regulatory scope, a review of the ingredients used to treat hair with (rGO/BSA)$_1$ is an opportunity to identify potential pitfalls or substantiate the safety of each ingredient used during the cosmetic intervention. Here, it is considered that any of the ingredients might be shortly exposed to human skin (without injuries) or eyes. In order to limit exposure to this minimum (i) the treatment should be applied in a washing sink, (ii) the client should wear a standard cape towel and not have skin injuries on the neck and head and (iii) the hairstylist should wear gloves during the process. A short review of skin and eye exposure to such ingredients is described following.

3.3.7.1 BSA

BSA (*bovine serum albumin* CAS: 9048-46) is a protein present in cow's milk, more specifically, in the "whey protein" fraction[231]. In our process, it is used at the concentrations of 200 mg/l (0.02%), which is below typical values of native BSA in milk at 240 to 400 mg/l[231,232]. Skin allergy to cow's milk is more common to children (< 3%) than adults[233]. Natale *et al.*[233] investigated the allergenicity of individual proteins present in milk; the results are that in over 90% of the cases α_{s2}-casein and IgG caused

allergic reaction in people with milk allergy, while isolated BSA caused allergic manifestation in only 45% of the people with predisposal to milk allergy. Due to the low allergenicity and cosmetic properties, whey protein (which is composed of 5.4 to 8.6% of BSA[234]) is used as *leave-on* formulations in 62 registered products with concentration up to 0.5%[235]. Even at such concentration, it exceeds the amount of BSA in the buffer solution.

No data was found regarding BSA exposure to eye in the concentration used in our procedure. However, in control experiments[236,237] BSA[1] was applied to eye models as drug vehicles at ~0.1% and showed no tissue edema or eye irritation after 24h of exposure. Furthermore, whey protein is deemed as a safe cosmetic ingredient and registered in 16 products to be used in the eye area[235].

3.3.7.2 Acetate buffer

Sodium Acetate (CAS: 127-09-3) is used in our procedure with a concentration of 8.2%$_w$ in water. An SDS of this material used in the same concentration as in this research[238] (but not neutralized by acid) indicates to be tissue irritant upon eye contact causing redness, tearing, itching, burning and conjunctivitis. The solution applied on skin can cause redness and itching.

Acetic Acid (CAS: 64-19-7) is used in our procedure with a concentration of 6%$_{vol}$ in water. Such concentration is in the usual range of edible vinegars from 4% to 8%$_{vol}$[239]. Acetic acid in a concentration like this can be directly applied on skin in order to treat lice and other skin conditions[239]. Skin irritation had been reported in a case of long direct exposure (8h) to vinegar[239] or in 4h exposure at 10% concentration[240]. Ocular exposure to acetic acid at 10% concentration causes permanent eye injury; at 5% concentration, it causes severe irritation (recoverable in two weeks)[241].

No safety data sheet (SDS) was found for the acetate buffer at the conditions used in this research (0.2 M). However, the buffer solution (mixture of both acid and base) is probably less aggressive than individual solutions of acetic acid or the sodium acetate. The buffer pH is 4.75, which finds itself in the range of pH of healthy human skin; from 4.5 to 5.2[242].

3.3.7.3 Graphene Oxide

Graphene Oxide mixture (from Graphenea) stems from the Hummers method and is further dissolved in deionized water. The concentration in our procedure is 1000 µg/ml or 0.1%$_w$.[2] In a recent cytotoxicity study[243] on a skin model, no significant tissue harm was observed for 0.01%$_w$ concentration up to 10 days of exposure. Another study[244]

---

[1] 20µl/eye n PBS buffer.

[2] However, probably a very low concentration could be used in the process, as demonstrated in Figure 25d, where only the supernatant part of centrifuged GO is present and is still attached to BSA.

on GO 24h-exposure to structural cell concluded that the NOAEL/LOAEL[1] for such nanoparticle is 10/20 µg/ml. This possibly alludes to the fact that a quick removal of spill followed by intense water washing (therefore dilution) could neutralize harmful effects on human skin.

Single exposure of GO in eye model at 0.1 mg/ml manifested no short or long term corneal opacity, conjunctival redness, abnormality of the iris, or impairment of corneal epithelium[245,246]. On the other hand, 5-day repeated GO exposure to the eye causes reversible mild corneal opacity, conjunctival redness and corneal epithelium damage to a rat model (but also healable).[245]

Hair treated with (rGO/BSA)$_1$ will inevitably be in contact with the human skin in a similar way that a coated cloth would. Zhao *et al.*[247] devised a textile cloth coated with GO with demonstrated antibacterial properties and did not observe skin irritation. Since rGO displays lower toxicity than GO[248], it is expected to be just as innocuous on human skin contact. Another research[11] explored coated wearables with graphene where no irritation was observed on human skin even though the wearable was in direct contact with it. Based on biocompatibility studies, Ameri *et al.*[249] went even further and developed a graphene tattoo to be applied directly on human skin via wet transfer. The tattoo has an ultra-thin profile, allowing the coating to intimately be attached to the microscopically rough morphology of skin through van der Waals interactions.

---

[1] No observed adverse effect level/lowest observed adverse effect level at 80% of cell viability

3.4 Summary

The technique developed in chapter 2 was adapted to be more human-friendly and explored as a cosmetic procedure for human hair. The results of applying the graphene-like coating on human hair were evaluated through the lenses of multiple techniques, through which it was possible to measure the physical and cosmetic changes on human hair.

The graphene-based cosmetic was observed to finely coat human hair, conforming to its microstructures. Even after a sequence of 1-month equivalent washings (*shampoos*) the coating was detected to remain on hair. Most importantly in the point of view of cosmetics, it was discovered that the graphene-based coating bridges the hair scale gaps even after several washing procedures. Such scale closing effect may allow protection of the hair structure against chemical attacks.

The forces required to comb the treated hair were negatively affected by the coating, requiring between 9% and 26% more energy to comb it. This result is at odds with the expected effect following literature review; hair surface has coefficients of friction between 0.072 and 0.046, while the graphene-like material is expected to have μ = 0.026.[1]

In terms of electrical properties, it was found that rGO-Bio$_{nanocoatings}$ transformed hair into a dissipative surface. Such property allowed hair to be drastically less prone to static effects than a control experiment. Moreover, this effect lasted for at least the equivalent of a month at high performance (at least 90% of flyaway hair reduction).

Hair color change was characterized by a newly developed method here. The method requires very simple hardware; a document scanner and a printable color pallet. The method ensures reproducibility of light conditions at extremely low cost. With this technique it was observed that treatment with rGO-Bio$_{nanocoatings}$ lead to a general trend to darken hair. This trend is more pronounced for lighter colors and not significant for black hair. The color parameters are less affected than the general lightness, which keeps the looks of treated hair in naturally authentic color ranges.

Mechanical testing of the hair was also conducted in order to assess possibility of permanent damage resulting from application of rGO-Bio$_{nanocoatings}$. There was no statistical difference in terms of strain at rupture and stress at rupture for the treated hair in comparison to an untreated control experiment.

The last measurement conducted was thermogravimetry. It was discovered that the graphene-like coating worked as a heat protective technology. Treated hair reduced water loss upon heating by the factor between 25% and 33%, depending on the heating cycle. Moreover, the treatment delayed the peak of moisture loss by +28°C and reduced the maximum weight loss intensity by half.

---

[1] It was assumed that the reduced graphene oxide from a Li *et al.*[85] resembled ours. These coefficients were measured against Si_3N_4, force of 40nN and using a 40 to 60 nm ball indent.

The mechanisms and hypothesis explaining the above-described results are explored in the chapter. Finally, a critical view on the safety of the process was conducted. There is preponderance of evidence indicating that the ingredients are relatively safe as hair cosmetics, which is the first step before considering the conduction of certified toxicology assays.

4 Discussions and Outlook

As introduced in the research questions, this thesis is a contribution within multidisciplinary fields that are investigating the employment of graphene for new technologies. Before asserting if graphene is the material of the 21st century it is important to develop feasible processing routes and reconcile them with the fundamental aspects of graphene.

Here, a new layer-by-layer dipping process is presented, allowing the production of films with alternated materials; graphene oxide and bio-interfactants. The central theme presented in this thesis was the adsorption of these materials on each other and diverse substrates, allowing the scalable formation of nanometric coatings.

This thesis explores this scope by presenting two narratives, a *materials science* narrative (chapter 2) and a *materials engineer* narrative (chapter 3). In chapter 2, the chemistry of GO was explored as an opportunity to interact strategically with selected biomolecules and form nanometric coatings. In that chapter, the fundamental driving forces behind this new coating are investigated, and relationships are delineated between structures and their properties.

On the other hand, in chapter 3, a study case for the application of this material is presented. To the extent of my knowledge it is the first time that time that a truly nanometrically thin graphene-based film has been applied on human hair and characterized for its cosmetic properties. It was demonstrated in practical terms that the technology presented in chapter 2 delivered desired result as a hair cosmetic. Chapter 3 focused on measuring attained properties, developing new measurement techniques, and discussing reals-world aspects of deploying such innovation as a hair cosmetic.

Both approaches, in chapter 2 and 3, are interwoven with common themes, which will be presented in the next subchapters.

4.1 Theme 1: Water

One of the core themes that defines the process developed here is the fact that it is employed using aqueous media. This decision had multiple strategic features. Firstly, it has the characteristic of allowing a process that can be contained in a controlled space while gravity and capillarity ensure contact with target materials.

Secondly, there is the practical advantage of using the universal solvent, ubiquitous and readily available at high purity in most laboratories. This avoids bottlenecks in the R&D phase and later can facilitate employment in commercial settings.

The third advantage of using water is that most of the materials that have ever been studied have probably been characterized in the presence of water (if not in a laboratory, with computer simulations). This furnishes the researcher with a broad library of initial knowledge to start investigations and scout materials. Also, these properties are mapped through different water pH.

The fourth appealing aspect of using water is that it is the standard environment where biomolecules operate. That means making available a large library of molecules that readily perform predictable interactions with other solids and particles.[101]

These four aspects stemming from the use of water can be viewed individually in combination with graphene oxide:

(i)   Liquid state

By being in an aqueous media, graphene oxide is bound to relative slow motion (especially in conditions used in this research; at high concentrations with big flakes[250]). Such detail suggests that time is an important variable in case the goal is to transport large amounts of graphene oxide. On the other hand, this is not a hurdle, but a benefit, if the final goal is to achieve a nanometrically thin material.

From a practical point of view, once graphene oxide is embedded in a liquid, it can be easily manipulated, as numerous tools are already in place in many industries to deal with liquid manipulation. For example, in the case of being applied as a hair cosmetic, there are already tools to allow embedding hair in liquid media (hair washing sinks) or techniques to keep a liquid mixture on hair (increasing the viscosity of the fluid or developing a foam).

(ii)   Availability of water

Multiple other solvents allow higher dispersion and stability of graphene oxide (and graphene)[43,44,251]. However, the use of these other solvents would probably have rendered the processes more limited during the experimental phases and useless for several applications, mainly when the application is safety- and/or cost-critic.

In the study case explored in chapter 3, water was arguably the only practical solvent option. Either if the treatment was to be conducted in a hair salon or a domestic setting, the person applying the product could easily make further dilutions with water if required.

(iii)   Knowledge on the interactions with water

The behavior of graphene oxide has been thoroughly characterized in the presence of water (through a broad range of pH), allowing prediction of charges. Moreover, multiple simulations have also been conducted between graphene oxide and other substrates in the presence of water. This previous knowledge was fundamental during the development stages of GO-Bio$_{nanocoatings}$.

In the case of being applied as a cosmetic product, there is already vast established know-how on packaging technology. Most products are water-based, and the decision of using water deems to be practical and cost-effective when finding the right packaging for the appropriate shelf-life.

(iv)   Water being the medium for biomolecules

A priori, graphene oxide is a foreign material in any metabolism. However, the interactions between these materials have been vastly characterized.[252] The previous knowledge on this area supported the understanding of non-covalent

adsorption that easily develops between graphene oxide and biomolecules (further discussed in this chapter).

In terms of a commercial application, the use of graphene oxide in the presence of a near-physiologic media (biomolecule in water) can be used as a marketing strategy in the sense of mixing synthetic materials with natural ingredients.

4.2 Theme 2: Bio-interfactants and anchoring effects

Aside from the theme "water", there is also an interesting discussion on the theme of using biomolecules. In a way, the choice of using biomolecules in this research quest enabled the possibility to employ specialized molecules that guided evolution of life[253] through billions of years. However, from a materials science point of view, the task may not necessarily be to explore the role of biomolecules in evolution but to translate knowledge from biochemistry into the nanotechnology domain.

One case of translation between fields is the coining the term "bio-interfactant" to biomolecules that modify properties of a given surface.[46,254] In this research, two biomolecules (a cow derived protein and a fungi enzyme) were used precisely to that end. Possibly this tendency to modify surfaces serves a purpose in a metabolic system, but such biological roles are outside of the scope of this research. The scope of this research is rather to interpret the adsorption dynamics of these biomolecules as tools that operate predictively in the nanometric scale.

Understanding the interactions of these molecules is facilitated by prior research conducted on them and also by having compiled information at disposal, like the "Protein Data Bank".[255] The bio-interfactants used here, BSA and LAC, had previously been observed to strongly adhere to multiple substrates and change their properties. Even though these surfaces modifications are expressed differently among BSA and LAC, under closer inspection, they both were found to be beneficial to adsorb and anchor graphene oxide.

In the conditions explored in this research, LAC tends to adsorb driven by its dipole moment, orienting itself towards the negatively charged surface (quartz). BSA tends to have its adsorption event driven by hydrophobic residues. These tendencies, combined with the distribution of amino-acid residues, were found to play a distinctive role in adsorbing simultaneously to the substrate and to graphene oxide.

In both bio-interfactants about 10% of their solvent-accessible surfaces are composed of three residues: arginine, lysine, and histidine. These residues were found to be responsible for strong adhesion to both silica and graphene oxide. On LAC, these three residues are highly concentrated on one side of the molecule. On the other hand, BSA presents these residues well spread on its globular-shaped form.

The combination of the adsorption event and the distribution of such residues were decisive to result in a distinct degree of graphene oxide attraction. Both general and localized variations in a bio-interfactant play a role on the "double-sided tape" quality. In this aspect, BSA showed to attract more quantities of graphene oxide than LAC did.

Moreover, the bio-interfactants were tested for their capability to anchor and fix the adsorbed graphene oxide as a result from a mild thermal reduction. On the microscopic scale, delamination of coating without the bio-interfactants was observed (Figure 37d). On the other hand, instead of a delamination event, coatings with LAC and BSA manifested topographic ripples, which may be result from the stress caused by anchoring points (Figure 37e and f). These topographic features (i.e., deformation in graphene structure) may be an interesting artifact to manipulate the electronic characteristics of coatings: inducing, for example, band-gap, pseudomagnetic field, and carrier puddles.[134]

Besides such microstructural features, it was found that BSA remained strongly linked to the backbone of graphene oxide. This linking lead to the development of higher proportions of sp^2 sites and allowed more oxygen release comparing to the use of LAC. This distinction indicates that there may be other bio-interfactants that are possibly better sp^2 promoters (at even lower temperatures) and that could provide an even stronger anchoring. Achieving these characteristics are in line with the requirements of the hair cosmetic study case, where milder heating conditions, long product durability, and high performance would add value as a product.

It was not demonstrated whether covalent bonding was formed between the bio-interfactants and GO before or after the thermal reduction. It is the case, however, that the carboxylic groups from GO (typically on the edge of the flake) can covalently bind to free amine groups[1] [256,257] (which are present on the bio-interfactants). Regardless of this possibility, by exposing these coatings to harsh environments (for example the ultrasound waves in water), a higher deterioration for coatings without bio-interfactants was observed. Between the usage of LAC and BSA, it was observed that coatings with BSA require more energy to suffer disruption of its continuous structure. It could be the case that the reduced graphene oxide on $(rGO)_1$, $(rGO/LAC)_1$, and $(rGO/BSA)_1$ have, in this order, less likelihood of detaching from its anchoring points and folding on themselves[83] during the mechanical perturbation.

Another interesting result from the series of "robustness tests" was the performance of a high purity graphene monolayer on quartz. The high purity graphene crystal did not stand on the substrate, not even for 7 minutes when being inside an ultrasonic water bath (100% loss of electrical conductivity). The coatings stemming from graphene oxide suffered between 30% and 55% of the conductivity loss in such test and sustained conductivity for over 15h of exposure.

Peeling tests showed that it would require energies above 300 J/m^2 to completely remove our coatings from quartz substrate. This energy is at least 100 times of that energy required to remove a transferred CVD-graphene from quartz.[144] This result attests that defects on the graphene lattice can be taken advantage of and result in superior adhesive properties.

---

[1] Under specific media and mild temperatures (from 70 to 130°C)

4.3 Theme 3: Multi-layered structures

Lastly, another theme in this thesis is the intricacies of the repeatable layer-by-layer (LbL) process for the three families of materials (with LAC, BSA, or none). It was observed that bio-interfactants are responsible for scaling the properties of the coatings following a proportion to the number of depositions. For example, $(GO/LAC)_4$ absorbs twice the light than $(GO/LAC)_2$ does. On the other hand, the family of coatings without bio-interfactants, $(GO)_n$ and $(rGO)_n$ did not strongly manifest this linear tendency.

In this way, the number of depositions n in the LbL process could be employed as a parameter to model the characteristics of these coatings. By modeling the properties with functions dependent on n, it was possible to extrapolate the intrinsic properties of ideal single layers and compare them for different systems. This allowed to assert that the coatings with BSA provide higher electrical conductivity for the same light absorbance (as compared to LAC and the coatings without bio-interfactants). This idea further substantiates that BSA does lead to more graphene-like characteristics after thermal reduction. In other words, even considering that BSA is not electrically conductive and that it contributes to higher light absorbance, its use still results in a coating with higher electrical conductivity for the same absorbance than a coating only made from graphene oxide.

Another area investigated in the theme of multi-layered structures was the measurement of thickness throughout the 10 levels of deposition on the family of $(rGO/LAC)_n$ and $(rGO/BSA)_n$ coatings. For that, four independent techniques were employed to measure coating thickness: AFM, XPS, LSCM, and a model based on percolation theories. The cross-checking of the techniques allowed a better understanding of the structure of these coatings.

Most interesting was the fact that coatings can expand as a result of the thermal reduction, an effect named "puffing". Such phenomenon does not disrupt the scaling of electric and optic properties, meaning that (i) the electric properties are not limited by continuous overlapping contact between flakes and (ii) multiple air/coating interfaces do not affect the transmittance of photons (with 550 nm wavelength) substantially.

Possibly other bio-interfactants (beyond LAC and BSA) may lead to varying degrees of puffing. The resulting coatings may be useful as sensors[258], gas barrier[259] and coatings for anodes[260–262].

4.4 Open questions and suggestion for future research

4.4.1 Chemical reductions

This thesis explored only mild thermal reduction up to 250°C. The effects of anchoring were observed only under this condition. It could be interesting to investigate if BSA would still provide strong anchoring and selectivity of graphene oxide in higher temperature ranges.

If bio-interfactants could be used in more extreme conditions, the GO-Bio$_{nanocoatings}$ might aim to emulate graphene properties. I would suggest to reduce the coatings under further conditions like: high temperatures and presence of H$_2$, vacuum and high temperature, in phenylhydrazine, microwave, plasma or UV-light.[31]

As discussed in chapter 1, the cost of covering one square meter of graphene is 6 orders of magnitude higher than covering the same area with graphene oxide. Within this space, optimization on the chemical reduction of graphene oxide is of primordial interest and not a cost limitation.

4.4.2 One-step application

The application of graphene oxide is enabled through a functionalized surface with bio-interfactants. Perhaps graphene oxide can be functionalized in advance with these biomaterials in a stable mixture and allow assembly of films also via dip coating. This would have practical benefits, allowing 1-step application on surfaces. Bio-interfactants could be mixed with graphene oxide in diverse concentrations and tested for their adsorption in a quartz crystal microbalance.

4.4.3 Support from AI

An exciting direction to veer this research is by combining it with artificial intelligence (AI). As discussed previously, the localized and general variations of properties of the bio-interfactants play a role in its "double-sided tape" quality. AI could help accelerate research by a series of automated processes:

(i)   Scouting

An automated system could be developed for screening hundreds of thousands of biomolecules in the *Protein Data Bank*[255] for specific molecular features. For example, selecting biomolecules that have a higher concentration of desirable residues on their surface (arginine, lysine, and histidine).

(ii)   Scoring/Simulating

Some of the molecules may already have been studied for its adsorption behavior and may be available in the *Biomolecular Adsorption Database*[263], which would cut time of performing molecular dynamics simulation. The other candidates could be simulated for their adsorption tendencies towards desirable substrates. By having these potential candidates, and their adsorptive information, simple calculations can be conducted in order to score the potential of positive attractive forces towards graphene oxide. See references[52,264].

The experimental phase in the laboratory could start with the candidates found by the AI support.

4.4.4 Puffing effect after thermal reduction

As presented in chapter 2.2.2.3, it was suggested that there is a puffing effect after making the thermal reduction of thick GO-Bio$_{nanocoatings}$. It was expected that the

coating (rGO/BSA)$_{10}$ would be ~40 nm thick, but LSCM measured a thickness almost 6 times higher. It would be interesting to measure the thickness of the unreduced form (GO/BSA)$_{10}$. Such measurement could demonstrate if puffing happens due to thermal reduction or if the coating is already not densely packed after dip-coatings.

Moreover, I also suggest conducting destructive tests on coatings from n = 1 to 10 (like in chapter 2.2.3). This test would indicate if the puffing plays a negative role in the attachment quality of the coating.

4.4.5 Orientation of target

The relative orientation could play an interesting role in the adsorption of graphene oxide. In early-stage experiments (not shown in this thesis), I attempted to measure the effects of relative orientation during the dip-coatings. For example, instead of resting the sample with the target surface facing upwards, the orientations were changed (facing sideways and upside down). It could be that this changes the adsorption of bigger flakes and agglomerations (which are more driven by gravity). Moreover, for experiments "sideways" it could be that the large graphene oxide flakes and agglomerations slowly attach to substrates and relax driven by gravity. That would form coatings that have anisotropic electrical conductivity.

4.5 Final considerations and conclusion of study case

Human hair was found to be an interesting candidate to apply the here-developed nanometric coatings. Not only can it be applied with human-friendly conditions, but it also yielded effects that are sought for in the cosmetic industry. The four main effects observed were: (i) the coating demonstrated to bring an anti-flyaway effect. (ii) the coating caused color changes on human hair (with some degree of recoverability upon washing). (iii) the coating increased the hair combing forces. (iv) the coating decreased the moisture loss upon heating.

Upon literature review, it is possible to assert that the technology presented in this thesis is fundamentally innovative because of the way it works as a hair cosmetic. Figure 66 depicts sketches of cosmetic action. Figure 66a shows the two main hair structures: scales and cortex. Figure 66b shows two possibilities of cosmetic action (purple marks and red marks). Purple marks indicate the mechanism of traditional hair dyes (which enter the hair cortex and modifies its color chemically).

Red marks in Figure 66b shows how some cosmetics (like conditioners or semi-permanent hair dye) act. These cosmetics transfer properties to hair by being on and between hair scales. Figure 66c is a recent innovation that applies a 2 μm graphene oxide in polymer coating on hair[145]. The material allows high electrical conductivity as well as high heat conductivity to dissipate charges and heat added on hair.
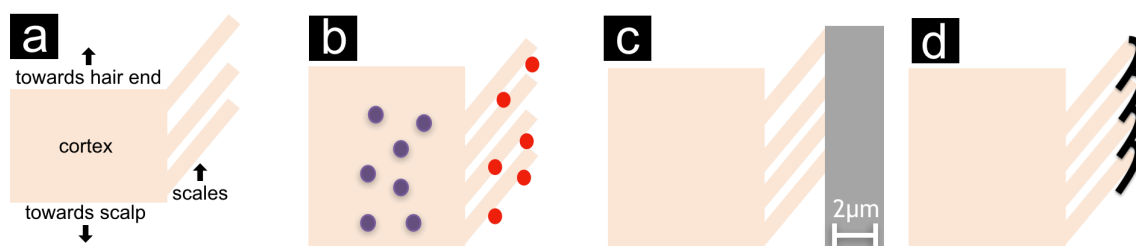
Figure 66 - Distinct hair cosmetic approaches. (a) simplified model representing an untreated hair. (b) Red circles represent superficial nanometric pigments which modify the hair color without chemical alterations (ex. henna). In purple circles, it is represented the action of chemical hair-dyeing (pigments penetrate hair structures). (c) A thick polymeric coating containing graphene[145] (in grey color) covers hair structure). (d) approach devised in this research; here, nanometrically-thin coating covers the microstructures of human hair bridging the space between scales.

The last case, Figure 66d, demonstrates how rGO-Bio$_{nanocoating}$ is attached to hair: a continuous, ultra-thin, electrically dissipative and strongly attached coating. Because of those properties, it manifests only minimal changes in bulk characteristics but allows 2D characteristics to be manifested in a higher degree and scalable along the hair fiber surface.

This 2D vs. bulk characteristics were in line with the demonstrated cosmetic benefits in this work (anti-static and water membrane). Arguably, there is a higher potential for rGO-Bio$_{nanocoatings}$ being explored to delivering 2D properties like better combability, higher softness, anti-bacterial function, anti-fungi function, and dust repellent. On the other hand, because of its ultra-thin nature, rGO-Bio$_{nanocoatings}$ may have a lower potential to deliver results that depend on bulk properties like UV-protection, mechanical strengthening, fiber straightening or curving, and intense color change.

Modifying the hair surface properties (optical, tribological, electrical, etc.) is exactly what many cosmetic products do. Opportunely, these properties are vastly researched and highly tunable for graphene-based materials, meaning that graphene-oxide is an excellent platform to develop multi-functional advanced cosmetics. It remains a challenge of the cosmetologists, scientists, and engineers to translate these modifications into safe solutions that achieve desirable macroscopic effects.

4.5.1 Future work for rGO-Bio$_{nanocoatings}$ as a hair cosmetic

4.5.1.1 Scale lifting

It was shown that rGO-Bio$_{nanocoatings}$ cover the hair finely, even bridging the gap between the scales. It could be interesting to measure up to which extent this affects the properties of hair:

(i)   Fatigue: Hair combing is equivalent to material fatigue, and it causes scale lifting. It could be interesting to investigate if the coatings could hinder this scale lifting after a cycle of controlled fatigue (30 grams)[152]. A technology like this would protect the scales of the hair and avoid an increase in hair wear and friction caused by the use of comb.

(ii)   Alkaline media: Hair scales are also lifted by the exposure to alkaline media. If the lifting is diminished by rGO-Bio$_{nanocoatings}$, it would allow to substantiate that the material protects against chemical exposures.

87

4.5.1.2 UV protection

Measurements of UVA, UVB and UVC radiation absorbances were measured for hair treated and untreated by rGO-Bio$_{nanocoatings}$ on blond hair (not published here). No statistical changes were observed. However, the process may be tuned with bio-interfactants that could absorb UV wavelengths or the process could be tuned by functionalizing graphene oxide with organic molecules that are already used as sunscreens, for example avobenzone, oxybenzone, and octyl methoxycinnamate[265]. Such solution could provide long-lasting sunscreens for hair (for example, for a full duration of a typical summer vacation).

4.5.1.3 Structure protection

It is unknown why rGO-Bio$_{nanocoatings}$ increased the friction properties of hair. Further investigations could aim at measuring the hair properties after a sequence of washings and/or applying hair conditioners. It is crucial to know exactly how rGO-Bio$_{nanocoatings}$ interacts with the most external part of hair. Based on microscopic images, it appeared that the coating had a stronger tendency to remain on already-broken scales on hair. That would be a desirable effect to claim, smoothing the rough structure of broken scales.

Yet, other questions remain. Is the coating attached to the natural hair oil 18-MEA? Does rGO-Bio$_{nanocoatings}$ protect the natural and desirable 18-MEA from the hair? Could it be that the strong adhesion of rGO-Bio$_{nanocoatings}$ could heal the surface properties of severely damaged hair[1]?. Those questions, if answered positively, could justify the safety assessment of a high demanding technology.

4.5.1.4 Diffusion through GO-Bio$_{nanocoatings}$

In chapter 3, the possibility that rGO-Bio$_{nanocoatings}$ could be performing as a water diffusion barrier was discussed. It appeared that the presence of the coating retarded moisture desorption on human hair. The simplest way of measuring such an effect with more precision would be by performing gravimetric sorption isotherms. Briefly; measure the weight of hair across controlled humidity in treated and untreated conditions (see in reference[266] figure 1). Such test on human hair could also be useful in order to determine the permeability of water through rGO-Bio$_{nanocoatings}$.

4.5.1.5 Gases from the thermal reduction

In chapter 3.3.7 a review on the safety aspects of (GO/BSA)$_1$ was conducted. However, the next step would be to assess the safety of the fumes released during the thermal reduction (using iron plate or hot air blowing). It is unclear if the gases released could be of a toxic nature. Mass spectroscopy combined with TGA could be

---

[1] From heating cycles, combing, and/or bleaching.

employed in order to reveal the gases (and concentrations) that are being released from the thermal reduction.

5 References

1.   Novoselov, K. S. Electric Field Effect in Atomically Thin Carbon Films. *Science (80-.).* **306**, 666–669 (2004).

2.   Hummers, W. S. & Offeman, R. E. Preparation of Graphitic Oxide. *J. Am. Chem. Soc.* **80**, 1339–1339 (1958).

3.   Wallace, P. R. The Band Theory of Graphite. *Phys. Rev.* **71**, 622–634 (1947).

4.   Ruess, G. & Vogt, F. Höchstlamellarer Kohlenstoff aus Graphitoxyhydroxyd. *Monatshefte für Chemie* **78**, 222–242 (1948).

5.   Boehm, H. P., Clauss, A., Fischer, G. O. & Hofmann, U. Das Adsorptionsverhalten sehr dünner Kohlenstoff-Folien. *Zeitschrift für Anorg. und Allg. Chemie* **316**, 119–127 (1962).

6.   Brink, L. *Nobel Lectures in Physics (2006 – 2010). Journal of Chemical Information and Modeling* **53**, (WORLD SCIENTIFIC, 2014).

7.   Hype Curve Concept Webpage. Available at: https://www.gartner.com/en/research/methodologies/gartner-hype-cycle. (Accessed: 5th November 2019)

8.   Iijima, S. Much Ado About Small Things. *Chem. Eng. News Arch.* **93**, 10–15 (2015).

9.   Iijima, S. Helical microtubules of graphitic carbon. *Nature* **354**, 56–58 (1991).

10.   Kostarelos, K. The long and short of carbon nanotube toxicity. *Nat. Biotechnol.* **26**, 774–776 (2008).

11.   Wang, Y. *et al.* Wearable and Highly Sensitive Graphene Strain Sensors for Human Motion Monitoring. *Adv. Funct. Mater.* **24**, 4666–4670 (2014).

12.   Rao, R. *et al.* Carbon Nanotubes and Related Nanomaterials: Critical Advances and Challenges for Synthesis toward Mainstream Commercial Applications. *ACS Nano* **12**, 11756–11784 (2018).

13.   Millington, R. B. & Nordberg, R. C. Process for preparing carbon fibers. (1966).

14.   Das, S., Warren, J., West, D. & Schexnayder, S. M. *Global Carbon Fiber Composites Supply Chain Competitiveness Analysis.* (2016).

15.   MaterialsToday. Available at: https://www.materialstoday.com/composite-applications/features/composites-flying-high-part-1/.

16.   Boehm, H. P., Setton, R. & Stumpp, E. Nomenclature and terminology of graphite intercalation compounds. *Carbon N. Y.* **24**, 241–245 (1986).

17.   Gao, W., Alemany, L. B., Ci, L. & Ajayan, P. M. New insights into the structure and reduction of graphite oxide. *Nat. Chem.* **1**, 403–408 (2009).

18. Wick, P. *et al.* Classification Framework for Graphene-Based Materials. *Angew. Chemie Int. Ed.* **53**, 7714–7718 (2014).

19. Shams, S. S., Zhang, R. & Zhu, J. Graphene synthesis: a Review. *Mater. Sci.* **33**, 566–578 (2015).

20. Lee, H. C. *et al.* Review of the synthesis, transfer, characterization and growth mechanisms of single and multilayer graphene. *RSC Adv.* **7**, 15644–15693 (2017).

21. Adetayo, A. & Runsewe, D. Synthesis and Fabrication of Graphene and Graphene Oxide: A Review. *Open J. Compos. Mater.* **09**, 207–229 (2019).

22. Kovtyukhova, N. I. *et al.* Non-oxidative intercalation and exfoliation of graphite by Brønsted acids. *Nat. Chem.* **6**, 957–963 (2014).

23. Tang, L. *et al.* Bottom-up synthesis of large-scale graphene oxide nanosheets. *J. Mater. Chem.* **22**, 5676 (2012).

24. Choucair, M., Thordarson, P. & Stride, J. A. Gram-scale production of graphene based on solvothermal synthesis and sonication. *Nat. Nanotechnol.* **4**, 30–33 (2009).

25. Sutter, P. How silicon leaves the scene. *Nat. Mater.* **8**, 171–172 (2009).

26. Kim, J., Lee, G. & Kim, J. Wafer-scale synthesis of multi-layer graphene by high-temperature carbon ion implantation. *Appl. Phys. Lett.* **107**, 033104 (2015).

27. Chen, M., Haddon, R. C., Yan, R. & Bekyarova, E. Advances in transferring chemical vapour deposition graphene: A review. *Mater. Horizons* **4**, 1054–1063 (2017).

28. Montes-Navajas, P. *et al.* Surface Area Measurement of Graphene Oxide in Aqueous Solutions. *Langmuir* **29**, 13443–13448 (2013).

29. Jung, I., Dikin, D. A., Piner, R. D. & Ruoff, R. S. Tunable Electrical Conductivity of Individual Graphene Oxide Sheets Reduced at "Low" Temperatures. *Nano Lett.* **8**, 4283–4287 (2008).

30. Larciprete, R. *et al.* Dual Path Mechanism in the Thermal Reduction of Graphene Oxide. *J. Am. Chem. Soc.* **133**, 17315–17321 (2011).

31. Singh, R. K., Kumar, R. & Singh, D. P. Graphene oxide: strategies for synthesis, reduction and frontier applications. *RSC Adv.* **6**, 64993–65011 (2016).

32. Kotov, N. A., Dékány, I. & Fendler, J. H. Ultrathin graphite oxide-polyelectrolyte composites prepared by self-assembly: Transition between conductive and non-conductive states. *Adv. Mater.* **8**, 637–641 (1996).

33. Dzukarnain, M. Z. B., Takami, T., Imai, H. & Ogino, T. Highly conductive, monolayer and large-area reduced graphene oxide films fabricated by electrical connection at the two-dimensional boundaries between the tiled graphene oxide

flakes. *Thin Solid Films* **615**, 247–255 (2016).

34. Pei, S., Zhao, J., Du, J., Ren, W. & Cheng, H.-M. Direct reduction of graphene oxide films into highly conductive and flexible graphene films by hydrohalic acids. *Carbon N. Y.* **48**, 4466–4474 (2010).

35. Fernández-Merino, M. J. *et al.* Vitamin C Is an Ideal Substitute for Hydrazine in the Reduction of Graphene Oxide Suspensions. *J. Phys. Chem. C* **114**, 6426–6432 (2010).

36. Barg, S. *et al.* Mesoscale assembly of chemically modified graphene into complex cellular networks. *Nat. Commun.* **5**, 4328 (2014).

37. Kong, C. Y. *et al.* Supercritical fluid conversion of graphene oxides. *J. Supercrit. Fluids* **61**, 206–211 (2012).

38. Chen, W., Yan, L. & Bangal, P. R. Preparation of graphene by the rapid and mild thermal reduction of graphene oxide induced by microwaves. *Carbon N. Y.* **48**, 1146–1152 (2010).

39. Manga, K. K., Zhou, Y., Yan, Y. & Loh, K. P. Multilayer Hybrid Films Consisting of Alternating Graphene and Titania Nanosheets with Ultrafast Electron Transfer and Photoconversion Properties. *Adv. Funct. Mater.* **19**, 3638–3643 (2009).

40. Becerril, H. A. *et al.* Evaluation of Solution-Processed Reduced Graphene Oxide Films as Transparent Conductors. *ACS Nano* **2**, 463–470 (2008).

41. Wu, J. *et al.* Organic solar cells with solution-processed graphene transparent electrodes. *Appl. Phys. Lett.* **92**, 263302 (2008).

42. Qian, W. *et al.* Solvothermal-assisted exfoliation process to produce graphene with high yield and high quality. *Nano Res.* **2**, 706–712 (2009).

43. Hernandez, Y., Lotya, M., Rickard, D., Bergin, S. D. & Coleman, J. N. Measurement of Multicomponent Solubility Parameters for Graphene Facilitates Solvent Discovery. *Langmuir* **26**, 3208–3213 (2010).

44. Konios, D., Stylianakis, M. M., Stratakis, E. & Kymakis, E. Dispersion behaviour of graphene oxide and reduced graphene oxide. *J. Colloid Interface Sci.* **430**, 108–112 (2014).

45. Paredes, J. I., Villar-Rodil, S., Martínez-Alonso, A. & Tascón, J. M. D. Graphene Oxide Dispersions in Organic Solvents. *Langmuir* **24**, 10560–10564 (2008).

46. Macul Perez, F. *et al.* Bio-interfactants as double-sided tapes for graphene oxide. *Nanoscale* **11**, 4236–4247 (2019).

47. Koenig, S. P., Boddeti, N. G., Dunn, M. L. & Bunch, J. S. Ultrastrong adhesion of graphene membranes. *Nat. Nanotechnol.* **6**, 543–546 (2011).

48. Kumar, R. M., Kumar, R. M., Lahiri, D. & Lahiri, I. Thermally reduced graphene oxide film on soda lime glass as transparent conducting electrode. *Surf.*

Coatings Technol. **309**, 931–937 (2017).

49. Annett, J. & Cross, G. L. W. Self-assembly of graphene ribbons by spontaneous self-tearing and peeling from a substrate. *Nature* **535**, 271–275 (2016).

50. López-Polín, G., Gómez-Herrero, J. & Gómez-Navarro, C. Confining Crack Propagation in Defective Graphene. *Nano Lett.* **15**, 2050–2054 (2015).

51. Dragneva, N. *et al.* Favorable adsorption of capped amino acids on graphene substrate driven by desolvation effect. *J. Chem. Phys.* **139**, 174711 (2013).

52. Stauffer, D. *et al.* An atomic charge model for graphene oxide for exploring its bioadhesive properties in explicit water. *J. Chem. Phys.* **141**, 044705 (2014).

53. Georgakilas, V. *et al.* Noncovalent Functionalization of Graphene and Graphene Oxide for Energy Materials, Biosensing, Catalytic, and Biomedical Applications. *Chem. Rev.* **116**, 5464–5519 (2016).

54. Lee, D. W. & Seo, J. W. sp 2 /sp 3 Carbon Ratio in Graphite Oxide with Different Preparation Times. *J. Phys. Chem. C* **115**, 2705–2708 (2011).

55. Bodik, M. *et al.* Fast low-temperature plasma reduction of monolayer graphene oxide at atmospheric pressure. *Nanotechnology* **28**, 145601 (2017).

56. Rajesh, C., Majumder, C., Mizuseki, H. & Kawazoe, Y. A theoretical study on the interaction of aromatic amino acids with graphene and single walled carbon nanotube. *J. Chem. Phys.* **130**, 124911 (2009).

57. Yang, K. *et al.* In vivo biodistribution and toxicology of functionalized nano-graphene oxide in mice after oral and intraperitoneal administration. *Biomaterials* **34**, 2787–2795 (2013).

58. Bourlinos, A. B. *et al.* Aqueous-phase exfoliation of graphite in the presence of polyvinylpyrrolidone for the production of water-soluble graphenes. *Solid State Commun.* **149**, 2172–2176 (2009).

59. Cai, M., Thorpe, D., Adamson, D. H. & Schniepp, H. C. Methods of graphite exfoliation. *J. Mater. Chem.* **22**, 24992 (2012).

60. Ni, N. *et al.* Understanding Mechanical Response of Elastomeric Graphene Networks. *Sci. Rep.* **5**, 13712 (2015).

61. Ferrari, A. C. *et al.* Science and technology roadmap for graphene, related two-dimensional crystals, and hybrid systems. *Nanoscale* **7**, 4598–4810 (2015).

62. Shao, F. *et al.* Layer-by-layer self-assembly TiO 2 and graphene oxide on polyamide reverse osmosis membranes with improved membrane durability. *Desalination* **423**, 21–29 (2017).

63. Wang, D. & Wang, X. Self-Assembled Graphene/Azo Polyelectrolyte Multilayer Film and Its Application in Electrochemical Energy Storage Device. *Langmuir* **27**, 2007–2013 (2011).

64. Zhang, D., Tong, J. & Xia, B. Humidity-sensing properties of chemically reduced graphene oxide/polymer nanocomposite film sensor based on layer-by-layer nano self-assembly. *Sensors Actuators B Chem.* **197**, 66–72 (2014).

65. Jeon, J.-W., Kwon, S. R. & Lutkenhaus, J. L. Polyaniline nanofiber/electrochemically reduced graphene oxide layer-by-layer electrodes for electrochemical energy storage. *J. Mater. Chem. A* **3**, 3757–3767 (2015).

66. Wang, X., Zhi, L. & Müllen, K. Transparent, Conductive Graphene Electrodes for Dye-Sensitized Solar Cells. *Nano Lett.* **8**, 323–327 (2008).

67. Moon, I. K. *et al.* 2D Graphene Oxide Nanosheets as an Adhesive Over-Coating Layer for Flexible Transparent Conductive Electrodes. *Sci. Rep.* **3**, 1112 (2013).

68. Watcharotone, S. *et al.* Graphene−Silica Composite Thin Films as Transparent Conductors. *Nano Lett.* **7**, 1888–1892 (2007).

69. Eda, G. *et al.* Transparent and conducting electrodes for organic electronics from reduced graphene oxide. *Appl. Phys. Lett.* **92**, 233305 (2008).

70. Diba, M., Fam, D. W. H., Boccaccini, A. R. & Shaffer, M. S. P. Electrophoretic deposition of graphene-related materials: A review of the fundamentals. *Prog. Mater. Sci.* **82**, 83–117 (2016).

71. Burkes, D. E. *et al. Fresh Fuel Characterization of U-Mo Alloys*. (2008).

72. Callister Jr, W. D. *Materials Science and Engineering - An Introduction (5th ed.)*. (John Wiley & Sons, 2007). doi:10.1108/acmm.2000.12847aae.001

73. Watts, J. F. & Wolstenholme, J. *An Introduction to Surface Analysis by XPS and AES*. (John Wiley & Sons, Ltd, 2003). doi:10.1002/0470867930

74. Wallart, X., De Villeneuve, C. H., Allongue, P., Henry de Villeneuve, C. & Allongue, P. Truly quantitative XPS characterization of organic monolayers on silicon: Study of alkyl and alkoxy monolayers on H-Si(111). *J. Am. Chem. Soc.* **127**, 7871–7878 (2005).

75. Kazi, S. N. *et al.* Investigation on the use of graphene oxide as novel surfactant to stabilize weakly charged graphene nanoplatelets. *Nanoscale Res. Lett.* **10**, 212 (2015).

76. Paredes, J. I., Villar-Rodil, S., Solís-Fernández, P., Martínez-Alonso, A. & Tascón, J. M. D. Atomic Force and Scanning Tunneling Microscopy Imaging of Graphene Nanosheets Derived from Graphite Oxide. *Langmuir* **25**, 5957–5968 (2009).

77. Compton, O. C., Dikin, D. A., Putz, K. W., Brinson, L. C. & Nguyen, S. T. Electrically Conductive "Alkylated" Graphene Paper via Chemical Reduction of Amine-Functionalized Graphene Oxide Paper. *Adv. Mater.* **22**, 892–896 (2010).

78. Akhavan, O. The effect of heat treatment on formation of graphene thin films from graphene oxide nanosheets. *Carbon N. Y.* **48**, 509–519 (2010).

79. You, S., Luzan, S. M., Szabó, T. & Talyzin, A. V. Effect of synthesis method on solvation and exfoliation of graphite oxide. *Carbon N. Y.* **52**, 171–180 (2013).

80. Hsu, H.-C. *et al.* Graphene oxide as a promising photocatalyst for CO 2 to methanol conversion. *Nanoscale* **5**, 262–268 (2013).

81. Maiti, R., Midya, A., Narayana, C. & Ray, S. K. Tunable optical properties of graphene oxide by tailoring the oxygen functionalities using infrared irradiation. *Nanotechnology* **25**, 495704 (2014).

82. Cote, L. J., Kim, F. & Huang, J. Langmuir−Blodgett Assembly of Graphite Oxide Single Layers. *J. Am. Chem. Soc.* **131**, 1043–1049 (2009).

83. Schniepp, H. C. *et al.* Bending Properties of Single Functionalized Graphene Sheets Probed by Atomic Force Microscopy. *ACS Nano* **2**, 2577–2584 (2008).

84. Gómez-Navarro, C. *et al.* Electronic Transport Properties of Individual Chemically Reduced Graphene Oxide Sheets. *Nano Lett.* **7**, 3499–3503 (2007).

85. Li, P. & Cheng, X. Nano-tribology studies of reduced graphene oxide films in air and in aqueous solutions with different pH values. *J. Mater. Res.* **32**, 323–333 (2017).

86. Yun, J.-M. *et al.* Morphological, optical, and electrical investigations of solution-processed reduced graphene oxide and its application to transparent electrodes in organic solar cells. *J. Ind. Eng. Chem.* **21**, 877–883 (2015).

87. Lin, J. *et al.* Biomimetic one-pot synthesis of gold nanoclusters/nanoparticles for targeted tumor cellular dual-modality imaging. *Nanoscale Res. Lett.* **8**, 170 (2013).

88. Fears, K. P., Petrovykh, D. Y. & Clark, T. D. Evaluating protocols and analytical methods for peptide adsorption experiments. *Biointerphases* **8**, 20 (2013).

89. Corrales Ureña, Y. R. *et al.* Investigations of biofilms formed on silica in contact with aqueous formulations containing laccase and maltodextrin. *Appl. Adhes. Sci.* **4**, 2 (2016).

90. Ithurbide, A., Frateur, I., Galtayries, A. & Marcus, P. XPS and flow-cell EQCM study of albumin adsorption on passivated chromium surfaces: Influence of potential and pH. *Electrochim. Acta* **53**, 1336–1345 (2007).

91. Fogel, R. & Limson, J. L. Probing fundamental film parameters of immobilized enzymes—Towards enhanced biosensor performance. Part I—QCM-D mass and rheological measurements. *Enzyme Microb. Technol.* **49**, 146–152 (2011).

92. Hakamada, M., Takahashi, M. & Mabuchi, M. Enhanced thermal stability of laccase immobilized on monolayer-modified nanoporous Au. *Mater. Lett.* **66**, 4–6 (2012).

93. Jachimska, B., Wasilewska, M. & Adamczyk, Z. Characterization of Globular Protein Solutions by Dynamic Light Scattering, Electrophoretic Mobility, and

Viscosity Measurements. *Langmuir* **24**, 6866–6872 (2008).

94. Jachimska, B., Tokarczyk, K., Łapczyńska, M., Puciul-Malinowska, A. & Zapotoczny, S. Structure of bovine serum albumin adsorbed on silica investigated by quartz crystal microbalance. *Colloids Surfaces A Physicochem. Eng. Asp.* **489**, 163–172 (2016).

95. Pérez-Fuentes, L., Drummond, C., Faraudo, J. & Bastos-González, D. Adsorption of Milk Proteins (β-Casein and β-Lactoglobulin) and BSA onto Hydrophobic Surfaces. *Materials (Basel).* **10**, 893 (2017).

96. Kubiak-Ossowska, K., Jachimska, B. & Mulheran, P. A. How Negatively Charged Proteins Adsorb to Negatively Charged Surfaces: A Molecular Dynamics Study of BSA Adsorption on Silica. *J. Phys. Chem. B* **120**, 10463–10468 (2016).

97. Corrales Ureña, Y. R. *et al.* Formation and composition of adsorbates on hydrophobic carbon surfaces from aqueous laccase-maltodextrin mixture suspension. *Appl. Surf. Sci.* **385**, 216–224 (2016).

98. Tavares, A. P. M. *et al.* Laccase immobilization over multi-walled carbon nanotubes: Kinetic, thermodynamic and stability studies. *J. Colloid Interface Sci.* **454**, 52–60 (2015).

99. Sosna, M., Chrétien, J.-M., Kilburn, J. D. & Bartlett, P. N. Monolayer anthracene and anthraquinone modified electrodes as platforms for Trametes hirsuta laccase immobilisation. *Phys. Chem. Chem. Phys.* **12**, 10018 (2010).

100. Camacho Córdova, D. I., Morales Borges, R., Arizaga, G. G. C., Wypych, F. & Krieger, N. Immobilization of laccase on hybrid layered double hydroxide. *Quim. Nova* **32**, 1495–1499 (2009).

101. Rabe, M., Verdes, D. & Seeger, S. Understanding protein adsorption phenomena at solid surfaces. *Adv. Colloid Interface Sci.* **162**, 87–106 (2011).

102. Belatik, A., Hotchandani, S., Carpentier, R. & Tajmir-Riahi, H.-A. Locating the Binding Sites of Pb(II) Ion with Human and Bovine Serum Albumins. *PLoS One* **7**, e36723 (2012).

103. Navaee, A. & Salimi, A. Efficient amine functionalization of graphene oxide through the Bucherer reaction: an extraordinary metal-free electrocatalyst for the oxygen reduction reaction. *RSC Adv.* **5**, 59874–59880 (2015).

104. Yang, A., Li, J., Zhang, C., Zhang, W. & Ma, N. One-step amine modification of graphene oxide to get a green trifunctional metal-free catalyst. *Appl. Surf. Sci.* **346**, 443–450 (2015).

105. Mattevi, C. *et al.* Evolution of Electrical, Chemical, and Structural Properties of Transparent and Conducting Chemically Derived Graphene Thin Films. *Adv. Funct. Mater.* **19**, 2577–2583 (2009).

106. Moon, I. K., Lee, J., Ruoff, R. S. & Lee, H. Reduced graphene oxide by chemical

graphitization. *Nat. Commun.* **1**, 73 (2010).

107. Manickam, S. *et al.* Exceedingly biocompatible and thin-layered reduced graphene oxide nanosheets using an eco-friendly mushroom extract strategy. *Int. J. Nanomedicine* **10**, 1505 (2015).

108. Wang, S. J., Geng, Y., Zheng, Q. & Kim, J.-K. Fabrication of highly conducting and transparent graphene films. *Carbon N. Y.* **48**, 1815–1823 (2010).

109. Bonanni, A., Ambrosi, A., Chua, C. K. & Pumera, M. Oxidation Debris in Graphene Oxide Is Responsible for Its Inherent Electroactivity. *ACS Nano* **8**, 4197–4204 (2014).

110. Khan, U. *et al.* Size selection of dispersed, exfoliated graphene flakes by controlled centrifugation. *Carbon N. Y.* **50**, 470–475 (2012).

111. Kubiak-Ossowska, K., Tokarczyk, K., Jachimska, B. & Mulheran, P. A. Bovine Serum Albumin Adsorption at a Silica Surface Explored by Simulation and Experiment. *J. Phys. Chem. B* **121**, 3975–3986 (2017).

112. Rouf, T. B. & Kokini, J. L. Biodegradable biopolymer–graphene nanocomposites. *J. Mater. Sci.* **51**, 9915–9945 (2016).

113. Zhang, H., Zhu, Z., Wang, Y., Fei, Z. & Cao, J. Changing the activities and structures of bovine serum albumin bound to graphene oxide. *Appl. Surf. Sci.* **427**, 1019–1029 (2018).

114. Seredych, M., Mikhalovska, L., Mikhalovsky, S. & Gogotsi, Y. Adsorption of Bovine Serum Albumin on Carbon-Based Materials. *C* **4**, 3 (2018).

115. Antonio Alves Júnior, J. & Baptista Baldo, J. The Behavior of Zeta Potential of Silica Suspensions. *New J. Glas. Ceram.* **04**, 29–37 (2014).

116. Yang, Z. *et al.* Flocculation performance and mechanism of graphene oxide for removal of various contaminants from water. *Water Res.* **47**, 3037–3046 (2013).

117. Huang, C.-J., Wang, L.-C., Liu, C.-Y., Chiang, A. S. T. & Chang, Y.-C. Natural zwitterionic organosulfurs as surface ligands for antifouling and responsive properties. *Biointerphases* **9**, 029010 (2014).

118. Phan, H. T. M., Bartelt-Hunt, S., Rodenhausen, K. B., Schubert, M. & Bartz, J. C. Investigation of Bovine Serum Albumin (BSA) Attachment onto Self-Assembled Monolayers (SAMs) Using Combinatorial Quartz Crystal Microbalance with Dissipation (QCM-D) and Spectroscopic Ellipsometry (SE). *PLoS One* **10**, e0141282 (2015).

119. Li, D., Müller, M. B., Gilje, S., Kaner, R. B. & Wallace, G. G. Processable aqueous dispersions of graphene nanosheets. *Nat. Nanotechnol.* **3**, 101–105 (2008).

120. Liu, K. *et al.* Green and facile synthesis of highly biocompatible graphene nanosheets and its application for cellular imaging and drug delivery. *J. Mater.*

Chem. **21**, 12034 (2011).

121. Chang, B. Y. S. *et al.* Facile hydrothermal preparation of titanium dioxide decorated reduced graphene oxide nanocomposite. *Int. J. Nanomedicine* (2012). doi:10.2147/IJN.S28189

122. Gui, Y. *et al.* Facile Solvothermal Synthesis and Gas Sensitivity of Graphene/WO3 Nanocomposites. *Materials (Basel).* **7**, 4587–4600 (2014).

123. Zhang, L. *et al.* Size-controlled synthesis of graphene oxide sheets on a large scale using chemical exfoliation. *Carbon N. Y.* **47**, 3365–3368 (2009).

124. Zhang, J. *et al.* Reduction of graphene oxide vial-ascorbic acid. *Chem. Commun.* **46**, 1112–1114 (2010).

125. Bautista, L. F., Morales, G. & Sanz, R. Biodegradation of polycyclic aromatic hydrocarbons (PAHs) by laccase from Trametes versicolor covalently immobilized on amino-functionalized SBA-15. *Chemosphere* **136**, 273–280 (2015).

126. Tully, J., Yendluri, R. & Lvov, Y. Halloysite Clay Nanotubes for Enzyme Immobilization. *Biomacromolecules* **17**, 615–621 (2016).

127. Singh, P. *et al.* Bovine serum albumin as a nanocarrier for the efficient delivery of ginsenoside compound K: preparation, physicochemical characterizations and in vitro biological studies. *RSC Adv.* **7**, 15397–15407 (2017).

128. Gebregeorgis, A., Bhan, C., Wilson, O. & Raghavan, D. Characterization of Silver/Bovine Serum Albumin (Ag/BSA) nanoparticles structure: Morphological, compositional, and interaction studies. *J. Colloid Interface Sci.* **389**, 31–41 (2013).

129. Jeong, H. K. *et al.* Thermal stability of graphite oxide. *Chem. Phys. Lett.* **470**, 255–258 (2009).

130. Zheng, Q. Bin *et al.* Improved electrical and optical characteristics of transparent graphene thin films produced by acid and doping treatments. *Carbon N. Y.* **49**, 2905–2916 (2011).

131. Robinson, J. T. *et al.* Wafer-scale Reduced Graphene Oxide Films for Nanomechanical Devices. *Nano Lett.* **8**, 3441–3445 (2008).

132. Stankovich, S. *et al.* Synthesis of graphene-based nanosheets via chemical reduction of exfoliated graphite oxide. *Carbon N. Y.* **45**, 1558–1565 (2007).

133. Schniepp, H. C. *et al.* Functionalized Single Graphene Sheets Derived from Splitting Graphite Oxide. *J. Phys. Chem. B* **110**, 8535–8539 (2006).

134. Deng, S. & Berry, V. Wrinkled, rippled and crumpled graphene: an overview of formation mechanism, electronic properties, and applications. *Mater. Today* **19**, 197–212 (2016).

135. Bao, W. *et al.* Controlled ripple texturing of suspended graphene and ultrathin graphite membranes. *Nat. Nanotechnol.* **4**, 562–566 (2009).

136. Acik, M. *et al.* The Role of Oxygen during Thermal Reduction of Graphene Oxide Studied by Infrared Absorption Spectroscopy. *J. Phys. Chem. C* **115**, 19761–19781 (2011).

137. García de la Torre, J. Hydration from hydrodynamics. General considerations and applications of bead modelling to globular proteins. *Biophys. Chem.* **93**, 159–170 (2001).

138. Haacke, G. New figure of merit for transparent conductors. *J. Appl. Phys.* **47**, 4086–4089 (1976).

139. Li, X. *et al.* Transfer of Large-Area Graphene Films for High-Performance Transparent Conductive Electrodes. *Nano Lett.* **9**, 4359–4363 (2009).

140. Choi, H. *et al.* Precise control of chemical vapor deposition graphene layer thickness using Ni x Cu 1−x alloys. *J. Mater. Chem. C* **3**, 1463–1467 (2015).

141. Nair, R. R. *et al.* Fine Structure Constant Defines Visual Transparency of Graphene. *Science (80-.).* **320**, 1308–1308 (2008).

142. Wang, Y., Tong, S. W., Xu, X. F., Özyilmaz, B. & Loh, K. P. Interface Engineering of Layer-by-Layer Stacked Graphene Anodes for High-Performance Organic Solar Cells. *Adv. Mater.* **23**, 1514–1518 (2011).

143. Rosli, N. N., Ibrahim, M. A., Ahmad Ludin, N., Mat Teridi, M. A. & Sopian, K. A review of graphene based transparent conducting films for use in solar photovoltaic applications. *Renew. Sustain. Energy Rev.* **99**, 83–99 (2019).

144. Das, S., Lahiri, D., Agarwal, A. & Choi, W. Interfacial bonding characteristics between graphene and dielectric substrates. *Nanotechnology* **25**, 045707 (2014).

145. Luo, C., Zhou, L., Chiou, K. & Huang, J. Multifunctional Graphene Hair Dye. *Chem* **4**, 784–794 (2018).

146. Herrwerth, S., Gruening, B., Koehle, H.-J. & Ulrich-Brehm, I. Quaternary dialkanolamine esters. (2015).

147. Brooke, D., Burns, J. S., Crookes, M. J., Britain, G. & Agency, E. *Using science to create a better place.* (Environment Agency, 2008).

148. Green, J. Composition of matter comprising a semi-permanent mascara and process to professionally apply the same. (2011).

149. Hoffmann, M. & Ning, J. Hair conditioning composition. (2018).

150. Robbins, C. R. Morphological, Macromolecular Structure and Hair Growth. in *Chemical and Physical Behavior of Human Hair* **74**, 1–104 (Springer Berlin Heidelberg, 2012).

151. Robbins, C. R. Genetic Control/Involvement in Hair Fiber Traits. in *Chemical and Physical Behavior of Human Hair* 177–204 (Springer Berlin Heidelberg, 2012). doi:10.1007/978-3-642-25611-0_3

152. Robbins, C. R. The Physical Properties of Hair Fibers. in *Chemical and Physical Behavior of Human Hair* 537–640 (Springer Berlin Heidelberg, 2012). doi:10.1007/978-3-642-25611-0_9

153. Popescu, C. & Höcker, H. Hair—the most sophisticated biological composite material. *Chem. Soc. Rev.* **36**, 1282 (2007).

154. Richena, M. & Rezende, C. A. Effect of photodamage on the outermost cuticle layer of human hair. *J. Photochem. Photobiol. B Biol.* **153**, 296–304 (2015).

155. Tanamachi, H., Tokunaga, S., Tanji, N., Oguri, M. & Inoue, S. Abstracts: 18-MEA and hair appearance. *Int. J. Cosmet. Sci.* **32**, 396–396 (2010).

156. Breakspear, S., Smith, J. R. & Luengo, G. Effect of the covalently linked fatty acid 18-MEA on the nanotribology of hair's outermost surface. *J. Struct. Biol.* **149**, 235–242 (2005).

157. Evans, D. J. & Lanczki, M. Cleavage of Integral Surface Lipids of Wool by Aminolysis. *Text. Res. J.* **67**, 435–444 (1997).

158. Robbins, C. R. Chemical Composition of Different Hair Types. in *Chemical and Physical Behavior of Human Hair* 105–176 (Springer Berlin Heidelberg, 2012). doi:10.1007/978-3-642-25611-0_2

159. Robbins, C. R. Interactions of Shampoo and Conditioner Ingredients with Hair. in *Chemical and Physical Behavior of Human Hair* 329–443 (Springer Berlin Heidelberg, 2012). doi:10.1007/978-3-642-25611-0_6

160. Obukowho, P. Neutralizing hair composition (US9420862B2). (2016).

161. Walker, R. *et al.* Composition for enhancing hair fiber properties (US20160175209A1). (2019).

162. Giles, C. C. D., Ellis, F. A., Murray, A. M., Pearce, M. L. & Red, P. E. Shampoo compositions (KR101490465B1). (2002).

163. Richardson, N. K., Schilling, K. M., Pocalyko, D. J. & Bailey, P. L. Covalent bonding of active agents to skin, hair or nails (US5490980A). (1996).

164. Ardila, L. M. Conditioner composition (KR101453218B1). (2015).

165. Robbins, C. R. Dyeing Human Hair. in *Chemical and Physical Behavior of Human Hair* 445–488 (Springer Berlin Heidelberg, 2012). doi:10.1007/978-3-642-25611-0_7

166. da França, S., Dario, M., Esteves, V., Baby, A. & Velasco, M. Types of Hair Dye and Their Mechanisms of Action. *Cosmetics* **2**, 110–126 (2015).

167. Gavazzoni Dias, M. F. Hair cosmetics: An overview. *Int. J. Trichology* **7**, 2 (2015).

168. Guerra-Tapia, A. & Gonzalez-Guerra, E. Cosméticos capilares: tintes. *Actas Dermosifiliogr.* **105**, 833–839 (2014).

169. Alessandrini, A. & Piraccini, B. Essential of Hair Care Cosmetics. *Cosmetics* **3**, 34 (2016).

170. Saravanan, G., Yamuna, G. & Nandhini, S. Real time implementation of RGB to HSV/HSI/HSL and its reverse color space models. in *2016 International Conference on Communication and Signal Processing (ICCSP)* 0462–0466 (IEEE, 2016). doi:10.1109/ICCSP.2016.7754179

171. SWIFT, J. A. Fine details on the surface of human hair. *Int. J. Cosmet. Sci.* **13**, 143–159 (1991).

172. Johnson, A., Trinh, P.-N. & Beard, B. Hair conditioner. (2006).

173. Pereira, A. *et al.* Ingredients for use in personal care compositions. (2019).

174. Hague, J. D., Khan-Lodhi, A. N. & Reid, E. S. Hair conditioning composition. (1997).

175. Robbins, C. R. Definitions of Consumer Relevant Hair Assembly Properties and How These are Controlled by Single Fiber Properties. in *Chemical and Physical Behavior of Human Hair* 641–707 (Springer Berlin Heidelberg, 2012). doi:10.1007/978-3-642-25611-0_10

176. Robbins, C. R. & Reich, C. Prediction of hair assembly characteristics from single-fiber properties. Part II. The relationship of fiber curvature, friction, stiffness, and diameter to combing behavior. *J. Soc. Cosmet. Chem.* **37**, 141–158 (1986).

177. Smith, J. R., Tsibouklis, J., Nevell, T. G. & Breakspear, S. AFM friction and adhesion mapping of the substructures of human hair cuticles. *Appl. Surf. Sci.* **285**, 638–644 (2013).

178. Tulachan, B., Singh, S. K., Philip, D. & Das, M. Harvesting electricity from human hair. *J. Soc. Cosmet. Chem.* **67**, 21–36 (2016).

179. Abie, S. M., Bergli, J., Galperin, Y. & Martinsen, Ø. G. Universality of AC conductance in human hair. *Biomed. Phys. Eng. Express* **2**, 027002 (2016).

180. Dyre, J. C. & Schrøder, T. B. Universality of ac conduction in disordered solids. *Rev. Mod. Phys.* **72**, 873–892 (2000).

181. Kumar, A. *et al.* Water mediated dielectric polarizability and electron charge transport properties of high resistance natural fibers. *Sci. Rep.* **8**, 2726 (2018).

182. Sadiku, M. N. O. & Akujuobi, C. M. Electrostatic discharge (ESD). *IEEE Potentials* **23**, 39–41 (2004).

183. Jayaweera, E. N., Wijewardhana, K. R., Ekanayaka, T. K., Shahzad, A. & Song, J. K. Triboelectric Nanogenerator Based on Human Hair. *ACS Sustain. Chem. Eng.* **6**, 6321–6327 (2018).

184. Invernizzi, F., Dulio, S., Patrini, M., Guizzetti, G. & Mustarelli, P. Energy harvesting from human motion: materials and techniques. *Chem. Soc. Rev.* **45**, 5455–5473 (2016).

185. Seshadri, I. P. & Bhushan, B. Effect of rubbing load on nanoscale charging characteristics of human hair characterized by AFM based Kelvin probe. *J. Colloid Interface Sci.* **325**, 580–587 (2008).

186. Jachowicz, J. & Garcia, M. L. Modifications of Human Hair. *J. Soc. Cosmet. Chem.* **36**, 189–212 (1985).

187. Bengtsson, M. All-day hair manageability for textured hair types. (Chalmers University of Technology, 2016).

188. Maddar, F. M., Perry, D., Brooks, R., Page, A. & Unwin, P. R. Nanoscale Surface Charge Visualization of Human Hair. *Anal. Chem.* **91**, 4632–4639 (2019).

189. Dupres, V. *et al.* Wetting and electrical properties of the human hair surface: Delipidation observed at the nanoscale. *J. Colloid Interface Sci.* **306**, 34–40 (2007).

190. Markarian, J. New developments in antistatic and conductive additives. *Plast. Addit. Compd.* **10**, 22–25 (2008).

191. Hair color market size. Available at: https://www.marketresearchstore.com/report/global-hair-color-market-2017-insights-demand-segmentation-169885. (Accessed: 1st November 2019)

192. Tobin, D. J. Hair color measurement. in *Colour Measurement* 371–392 (Elsevier, 2010). doi:10.1533/9780857090195.2.371

193. Ford, A. & Alanrobertsrdbbccouk, A. R. Colour Space Conversions. **1998**, 1–31 (1998).

194. Panhard, S., Lozano, I. & Loussouarn, G. Greying of the human hair: a worldwide survey, revisiting the '50' rule of thumb. *Br. J. Dermatol.* **167**, 865–873 (2012).

195. Santos Nogueira, A. C., Nakano, A. K. & Joekes, I. Impairment of hair mechanical properties by sun exposure and bleaching treatments. *J. Cosmet. Sci.* **55**, 533–537 (2004).

196. Barba, C. *et al.* Restoring important hair properties with wool keratin proteins and peptides. *Fibers Polym.* **11**, 1055–1061 (2010).

197. Nicholson, S., Daniels, G., Grant-Ross, P. & Tamburic, S. An Ex Vivo Comparison of The Tensile Strengthening Properties of Protein Derivatives on Damaged Hair. *J. Cosmet. Sci. J. Cosmet. Sci. Teglia, A. Secchi, G.Proteins*

Cosmet. **270**, 1106–1113 (1997).

198. Dario, M. F., Baby, A. R. & Velasco, M. V. R. Effects of solar radiation on hair and photoprotection. *J. Photochem. Photobiol. B Biol.* **153**, 240–246 (2015).

199. Ruetsch, S. B. & Kamath, Y. K. Effects of thermal treatments with a curling iron on hair fiber. *Int. J. Cosmet. Sci.* **26**, 217–217 (2004).

200. Ettlinger, J., Kirchen, L. & Yegles, M. Influence of thermal hair straightening on ethyl glucuronide content in hair. *Drug Test. Anal.* **6**, 74–77 (2014).

201. Marsh, J. M., Gray, J. & Tosti, A. *Healthy Hair*. *Healthy Hair* (Springer International Publishing, 2015). doi:10.1007/978-3-319-18386-2

202. Detwiler, S. P., Carson, J. L., Woosley, J. T., Gambling, T. M. & Briggaman, R. A. Bubble hair. *J. Am. Acad. Dermatol.* **30**, 54–60 (1994).

203. Gandhi, A. A., Kipling, S., Wright, L. & Latham, S. G. Curl Reversion and Damage: The Effect of Different Temperature Treatments on Hair. *J. Cosmetol. Trichology* **04**, 4–7 (2018).

204. Lima, C. R. R. de C. *et al.* Heat-damaged evaluation of virgin hair. *J. Cosmet. Dermatol.* 1–8 (2019). doi:10.1111/jocd.12892

205. Sayahi, E. *et al.* Effects of treatments with curling iron on human hair fibers. *Int. J. Recent Sci. Res.* **7**, 8736–8740 (2016).

206. Christian, P., Winsey, N., Whatmough, M. & Cornwell, P. A. The effects of water on heat-styling damage. *J. Cosmet. Sci.* **62**, 15–27 (2011).

207. Zhou, Y. *et al.* The effect of various cosmetic pretreatments on protecting hair from thermal damage by hot flat ironing. *J. Cosmet. Sci.* **62**, 265–282 (2011).

208. Ali, N., Marsh, J., Godfrey, S. & Williams, D. R. Aqueous MEA and Ammonia Sorption-Induced Damage in Keratin Fibers. *ACS Omega* **3**, 14173–14180 (2018).

209. Istrate, D., Popescu, C., Rafik, M. E. & Möller, M. The effect of pH on the thermal stability of fibrous hard alpha-keratins. *Polym. Degrad. Stab.* **98**, 542–549 (2013).

210. Gavazzoni Dias, M. F., Pichler, J., Adriano, A., Cecato, P. & de Almeida, A. The shampoo pH can affect the hair: Myth or Reality? *Int. J. Trichology* **6**, 95 (2014).

211. Ribeiro, A., Matamá, T., Cruz, C. F., Gomes, A. C. & Cavaco-Paulo, A. M. Potential of human γD-crystallin for hair damage repair: insights into the mechanical properties and biocompatibility. *Int. J. Cosmet. Sci.* **35**, 458–466 (2013).

212. Popescu, C. & Gummer, C. DSC of human hair: a tool for claim support or incorrect data analysis? *Int. J. Cosmet. Sci.* **38**, 433–439 (2016).
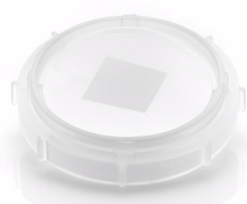
213. da Gama, R. M. *et al.* Thermal analysis of hair treated with oxidative hair dye under influence of conditioners agents. *J. Therm. Anal. Calorim.* **106**, 399–405 (2011).

214. MIHĂILĂ, A. & GHERGHEL, A. Thermal Analysis of Human Hair in Non-Isothermal and Isothermal Conditions. *Ann. Acad. Rom. Sci. Ser. Phys. Chem. Sci.* **2**, (2017).

215. Barba, C., Méndez, S., Martí, M., Parra, J. L. & Coderch, L. Water content of hair and nails. *Thermochim. Acta* **494**, 136–140 (2009).

216. Brebu, M. & Spiridon, I. Thermal degradation of keratin waste. *J. Anal. Appl. Pyrolysis* **91**, 288–295 (2011).

217. Monteiro, V. F., Maciel, A. P. & Longo, E. Thermal analysis of caucasian human hair. *J. Therm. Anal. Calorim.* **79**, 289–293 (2005).

218. Lima, C. R. R. D. C., De Almeida, M. M., Velasco, M. V. R. & Matos, J. D. R. Thermoanalytical characterization study of hair from different ethnicities. *J. Therm. Anal. Calorim.* **123**, 2321–2328 (2016).

219. Robbins, C. R. Reducing Human Hair Including Permanent Waving and Straightening. in *Chemical and Physical Behavior of Human Hair* 205–262 (Springer Berlin Heidelberg, 2012). doi:10.1007/978-3-642-25611-0_4

220. Nagase, S., Ohshika, M., Ueda, S., Satoh, N. & Tsujii, K. A Universal Structural Model for Human Hair to Understand the Physical Properties 1. *Bull. Chem. Soc. Jpn.* **73**, 2161–2167 (2000).

221. Devanathan, R., Chase-Woods, D., Shin, Y. & Gotthold, D. W. Molecular Dynamics Simulations Reveal that Water Diffusion between Graphene Oxide Layers is Slow. *Sci. Rep.* **6**, 29484 (2016).

222. Jiao, L., Zhang, L., Wang, X., Diankov, G. & Dai, H. Narrow graphene nanoribbons from carbon nanotubes. *Nature* **458**, 877–880 (2009).

223. Wortmann, F.-J., Hullmann, A. & Popescu, C. Water management of human hair. *Int. J. Cosmet. Sci.* **30**, 388–389 (2008).

224. Ban on Animal Testing.

225. Seidle, T. & Spielmann, H. *Alternative Testing Strategies Progress Report 2012 - Roadmap to next generation safety testing under Horizon 2020*. (2012).

226. EU Reference Laboratory for alternatives to animal testing.

227. Sharma, N., Singh, S., Kanojia, N., Grewal, A. S. & Arora, S. Nanotechnology: A Modern Contraption in Cosmetics and Dermatology. *Appl. Clin. Res. Clin. Trials Regul. Aff.* **5**, 147–158 (2018).

228. Animal Testing & Cosmetics (FDA).

229. Fischer, K. Animal Testing and Marketing Bans of the EU Cosmetics Legislation. *Eur. J. Risk Regul.* **6**, 613–621 (2015).

230. Luo, F. The current status of alternative methods for cosmetics safety assessment in China. *ALTEX* **36**, 136–139 (2019).

231. El-Agamy, E. I. The challenge of cow milk protein allergy. *Small Rumin. Res.* **68**, 64–72 (2007).

232. Le, T. T., Deeth, H. C. & Larsen, L. B. Proteomics of major bovine milk proteins: Novel insights. *Int. Dairy J.* **67**, 2–15 (2017).

233. Natale, M. *et al.* Cow's milk allergens identification by two-dimensional immunoblotting and mass spectrometry. *Mol. Nutr. Food Res.* **48**, 363–369 (2004).

234. Ribadeau-Dumas, B. & Grappin, R. Milk protein analysis. *Lait* **69**, 357–416 (1989).

235. Burnett, C. *et al.* Safety Assessment of Nylon as Used in Cosmetics. *Int. J. Toxicol.* **33**, 47S-60S (2014).

236. De Paiva, C. S. *et al.* Dry Eye–Induced Conjunctival Epithelial Squamous Metaplasia Is Modulated by Interferon-γ. *Investig. Opthalmology Vis. Sci.* **48**, 2553 (2007).

237. de Salamanca, A. E. *et al.* Chitosan Nanoparticles as a Potential Drug Delivery System for the Ocular Surface: Toxicity, Uptake Mechanism and In Vivo Tolerance. *Investig. Opthalmology Vis. Sci.* **47**, 1416 (2006).

238. SDS of Sodium Acetate. Available at: https://www.mccsd.net/cms/lib/NY02208580/Centricity/Shared/Material Safety Data Sheets _MSDS_/MSDS Sheets_Sodium_Acetate_Solution_1M_638_50.pdf.

239. Bunick, C. G. *et al.* Chemical burn from topical apple cider vinegar. *J. Am. Acad. Dermatol.* **67**, e143–e144 (2012).

240. York, M., Basketter, D., Cuthbert, J. & Neilson, L. Skin irritation testing in man for hazard assessment — evaluation of four patch systems. *Hum. Exp. Toxicol.* **14**, 729–734 (1995).

241. Heldreth, B. *et al.* Final Report of the Cosmetic Ingredient Review Expert Panel on the Safety Assessment of Methyl Acetate. *Int. J. Toxicol.* **31**, 112S-136S (2012).

242. Darlenski, R. & Fluhr, J. W. Measurement of Skin Surface Acidity. in *Agache's Measuring the Skin* 113–120 (Springer International Publishing, 2017). doi:10.1007/978-3-319-32383-1_12

243. Pelin, M. *et al.* Differential cytotoxic effects of graphene and graphene oxide on skin keratinocytes. *Sci. Rep.* **7**, 40572 (2017).

244. Gies, V. & Zou, S. Systematic toxicity investigation of graphene oxide: evaluation of assay selection, cell type, exposure period and flake size. *Toxicol. Res. (Camb).* **7**, 93–101 (2018).

245. Wu, W. *et al.* Evaluation of the toxicity of graphene oxide exposure to the eye. *Nanotoxicology* **10**, 1329–1340 (2016).

246. Yan, L. *et al.* Can Graphene Oxide Cause Damage to Eyesight? *Chem. Res. Toxicol.* **25**, 1265–1270 (2012).

247. Zhao, J. *et al.* Graphene Oxide-Based Antibacterial Cotton Fabrics. *Adv. Healthc. Mater.* **2**, 1259–1266 (2013).

248. Das, S. *et al.* Oxygenated Functional Group Density on Graphene Oxide: Its Effect on Cell Toxicity. *Part. Part. Syst. Charact.* **30**, 148–157 (2013).

249. Kabiri Ameri, S. *et al.* Graphene Electronic Tattoo Sensors. *ACS Nano* **11**, 7634–7641 (2017).

250. Esfahani, M. R., Languri, E. M. & Nunna, M. R. Effect of particle size and viscosity on thermal conductivity enhancement of graphene oxide nanofluid. *Int. Commun. Heat Mass Transf.* **76**, 308–315 (2016).

251. O'Neill, A., Khan, U., Nirmalraj, P. N., Boland, J. & Coleman, J. N. Graphene Dispersion and Exfoliation in Low Boiling Point Solvents. *J. Phys. Chem. C* **115**, 5422–5428 (2011).

252. Li, D. *et al.* When biomolecules meet graphene: from molecular level interactions to material design and applications. *Nanoscale* **8**, 19491–19509 (2016).

253. Harms, M. J. & Thornton, J. W. Evolutionary biochemistry: revealing the historical and physical causes of protein properties. *Nat. Rev. Genet.* **14**, 559–571 (2013).

254. Ureña, Y. R. C. *et al.* Interfactant action of an amphiphilic polymer upon directing graphene oxide layer formation on sapphire substrates. *Appl. Adhes. Sci.* **5**, 10 (2017).

255. Burley, S. K. *et al.* RCSB Protein Data Bank: biological macromolecular structures enabling research and education in fundamental biology, biomedicine, biotechnology and energy. *Nucleic Acids Res.* **47**, D464–D474 (2019).

256. Dreyer, D. R., Park, S., Bielawski, C. W. & Ruoff, R. S. The chemistry of graphene oxide. *Chem. Soc. Rev.* **39**, 228–240 (2010).

257. Shen, J. *et al.* Covalent attaching protein to graphene oxide via diimide-activated amidation. *Colloids Surfaces B Biointerfaces* **81**, 434–438 (2010).

258. Li, X. *et al.* Large-Area Ultrathin Graphene Films by Single-Step Marangoni Self-Assembly for Highly Sensitive Strain Sensing Application. *Adv. Funct. Mater.*

26, 1322–1329 (2016).

259. Su, Y. *et al.* Impermeable barrier films and protective coatings based on reduced graphene oxide. *Nat. Commun.* **5**, 4843 (2014).

260. Li, N. *et al.* High-rate lithium–sulfur batteries promoted by reduced graphene oxide coating. *Chem. Commun.* **48**, 4106 (2012).

261. Du, X., Guo, P., Song, H. & Chen, X. Graphene nanosheets as electrode material for electric double-layer capacitors. *Electrochim. Acta* **55**, 4812–4819 (2010).

262. Chang, J. *et al.* Multilayered Si Nanoparticle/Reduced Graphene Oxide Hybrid as a High-Performance Lithium-Ion Battery Anode. *Adv. Mater.* **26**, 758–764 (2014).

263. Vasina, E. N., Paszek, E., Nicolau, Jr, D. V. & Nicolau, D. V. The BAD project: data mining, database and prediction of protein adsorption on surfaces. *Lab Chip* **9**, 891–900 (2009).

264. Rimola, A., Sodupe, M. & Ugliengo, P. Affinity Scale for the Interaction of Amino Acids with Silica Surfaces. *J. Phys. Chem. C* **113**, 5741–5750 (2009).

265. Xie, S. *et al.* Graphene Oxide Transparent Hybrid Film and Its Ultraviolet Shielding Property. *ACS Appl. Mater. Interfaces* **7**, 17558–17564 (2015).

266. Barba, C. *et al.* Water absorption/desorption of human hair and nails. *Thermochim. Acta* **503**–**504**, 33–39 (2010).

267. Lee, D.-W., Kim, T. & Lee, M. An amphiphilic pyrene sheet for selective functionalization of graphene. *Chem. Commun.* **47**, 8259 (2011).

268. Used, C. ANTISTATIC AGENTS IN VARIOUS INDUSTRIAL PRODUCTS. in *Handbook of Antistatics* 287–357 (Elsevier, 2016). doi:10.1016/B978-1-895198-95-9.50017-0

269. CHEN, N. & BHUSHAN, B. Atomic force microscopy studies of conditioner thickness distribution and binding interactions on the hair surface. *J. Microsc.* **221**, 203–215 (2006).

270. Sakai, M., Nagase, S., Okada, T., Satoh, N. & Tsujii, K. A Universal Structural Model for Human Hair to Understand the Physical Properties 2. Mechanical and Permeation Behaviors. *Bull. Chem. Soc. Jpn.* **73**, 2169–2177 (2000).

6 Annexes

Annex 1 - Cost of graphene-based products.

WINDLE & MOODIE

COVENT GARDEN

APPOINTMENTS   SALON   PRODUCTS   STYLEBOOK   STOCKISTS   BLOG

SHOP   STORY   DELIVERY   T&CS

BACK TO SHOP

INVISIBLE DAY & NIGHT CREAM
WITH MONOI OIL AND SUGAR BEET
UV PROTECTOR

AWARD WINNER, Into The Gloss 2017 Top 25 Beauty Products

A "behind-the-scenes" moisturiser that brings hair to life. Revitalises faded locks with a healthy shine. Infused with monoi oil from the South Pacific to give far-reaching lustre and vitality, sugar beet extract to inject moisture, and aloe vera to sooth. Contains a **UV filter**.

Gently massage into the hair morning and night, or whenever the hair is thirsty. Do not rinse out.

100% Vegan and Gluten free.

£22.00 - 60ML

QUANTITY   1

ADD TO BASKET

SHARE - f ✈ ⓟ in ➕ 8⁺

LEARN MORE

The idea behind this product is to bring **skincare concepts into haircare**. Hair suffers from various forms of abrasion – from environmental damage and combing, to styling. We also learned that more damage is done to hair in the process of sleeping, when hairs rub against each other and create friction. The Invisible day & night cream is created to **protect hair** against any form of abrasion, day and night.

91% of our products are vegetarian suitable
74% of our products are vegan suitable
78% of our products are gluten free

INCI LISTINGS
Aqua (Water), Cetearyl Alcohol, Distearoylethyl Dimonium Chloride, Plumeria Acutifolia (Monoi) Flower Extract, Glyceryl Stearate, Betaine, Crambe Abyssinica Seed Oil, Creatine, Ethylhexyl Methoxycinnamate, PEG-100 Stearate, Benzyl Alcohol, Dicaprylyl Ether, Parfum (Fragrance), Gluconolactone, Lauryl Alcohol, Hydroxyethyl Ethylcellulose, Aloe Barbadensis (Aloe Vera) Leaf Extract, Sodium Benzoate, Hydrolysed Lupine Seed Extract, Salicylic Acid, Brassica Campestris (Rapeseed) Seed Oil, Glycerin, Hydroxyisohexyl 3-Cyclohexene Carboxaldehyde, Sorbic Acid, Butylphenyl Methylpropional, Sodium Hyaluronate, Rosmerinus Officinalis (Rosemary) Leaf Extract

https://www.windleandmoodie.com/hairproducts/shop/invisible-day-and-night-cream/
(accessed 17.02.2019)

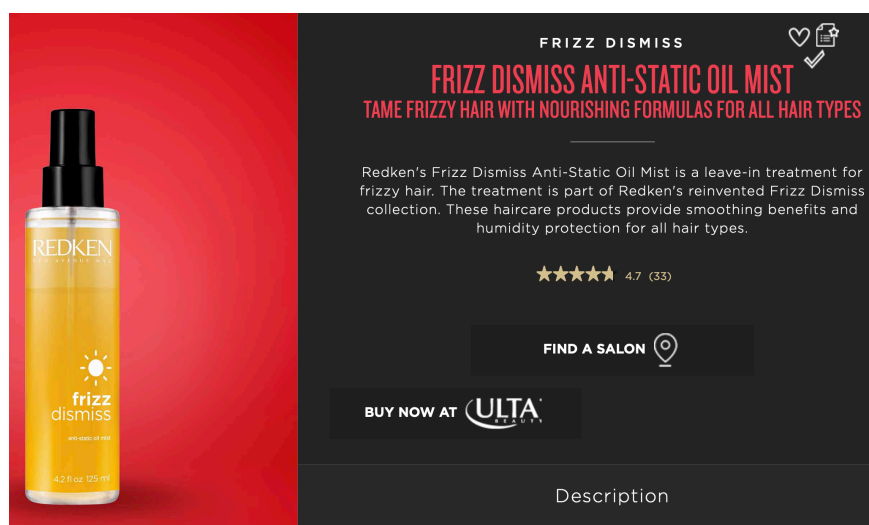*Annex 2 - Windle & Moodie product and description.*

the science

It's powered by our patented Healthy Hair Molecule (OFPMA), which in this formula does three things: blocks humidity, smooths hair and helps repel dirt and oil to keep hair cleaner, longer. The result: your hair will look and feel smooth and soft and will stay cleaner, longer.

https://www.livingproof.com/no-frizz/nourishing-styling-cream/R118.html?cgid=shop-by-benefit-antifrizz#start=1
(accessed 18.02.2019)

Annex 3 - Living proof product description

https://www.redken.com/products/hair-care/frizz-dismiss/frizz-dismiss-anti-static-oil-mist
(accessed 18.03.2019)

Annex 4 - Redken product description.

FELIPE PEREZ

E-Mail: fmacul@gmail.com
Phone: +49 176 75412303
Birth Date: 05 July 1988
Nationalities: Italian & Brazilian

CURRENT OCCUPATION

09/2019 – now
Engineering Trainee - *International Future Leadership Program*
Bayer AG, Leverkusen, Germany.

EDUCATION

02/2015 – 09/2019
PhD Candidate in Materials Engineering
University of Bremen: Faculty of Production Engineering & Fraunhofer Institute of Manufacturing Technology and Advanced Materials (IFAM), Bremen, Germany

PhD Challenge: Develop a novel graphene-based coating technology with antimicrobial properties

- Planned and carried out new nanomaterial development
- Interdisciplinary research including: laboratory experiments, molecular dynamic simulations and data science
- Major inventor of a patent to make graphene and biomolecules coating (Pub.No.: DE102017108831)
- First author of paper in high-impact factor journal
  - ➤ doi.org/10.1039/C8NR08607A
- Supported academic projects by interns (most notably 3rd prize at "Jugend forscht" contest in chemistry)

02/2008 – 02/2014
Graduated as Materials Engineer
Federal University of Santa Catarina, Brazil

- Final grade: 8.36/10.0
- Diploma thesis grade: 9.5/10.0
- Tutor of Mechanical Properties of Materials

09/2012 – 09/2013
Exchange Student (Master's level)
Imperial College London, United Kingdom

- Attended courses in Biomaterials & Mathematic Modeling

PROFESSIONAL EXPERIENCE

05/2018 – 09/2019
Founder and PM of *Nanohair*
Partially sponsored by Fraunhofer Venture, Munich, Germany.

Goal: Applying own research into marketable technologies

- Developing new hair care formulation, hands-on in laboratory
- Survey of patents and literature to identify biocompatibility of formulation
- Defining and executing roadmap towards commercialization into hair care industry
- Promoting research and initiating collaborations with external partners

03/2014 – 12/2014
Project Manager
CP monitoramento e diagnóstico, Piracicaba, Brazil

- Supported expansion of family business by monitoring and diagnosing environment dynamics of harmful sinantropic fauna in populated areas of Brazil

09/2012 – 09/2013
Student Assistant Researcher – New Materials Development
Centre for Advanced Structural Ceramics (CASC), Imperial College London, United Kingdom

- Supported development of ultra-light graphene foams

111

- Co-designed process for enhanced mechanical performance and co-directed mechanical tests of foams
- Co-author of two published papers in high-impact factor journals:
  - www.nature.com/articles/ncomms5328
  - www.nature.com/articles/srep13712

12/2012 – 05/2013
Universia Ambassador
London, United Kingdom

- Blogged about own international study experience at Imperial College London
- Provided support for students planning on studying in the UK

06/2011 – 05/2012
Internship in Process Engineering
Bremer Institut für angewandte Strahltechnik: BIAS, Bremen

- Designed dashboard interface in LabView to automate a plasma process
- Developed a mathematic model to optimize parameters of the plasma process using laws of thermodynamics -> Model successfully expanded process capabilities, allowing coating on silicon wafer

CORE STRENGHTS

Analytical Thinking
High Willingness to Learn
Creative Problem Solving
Decision Making
Project Management
Self-Motivated Personality

AWARDS

- **Full Doctorate Research Studies** at University of Bremen & Fraunhofer IFAM in Bremen, Germany awarded by The Brazilian National Council for Scientific and Technological Development (CNPq) in 2014

- **Post-Graduation Year of Master-level Studies** at Imperial College London, United Kingdom awarded by CAPES, a Brazilian government agency in 2012

FURTHER SKILLS

Language

English	full working proficiency
Spanish	full working proficiency
Portuguese	full working proficiency
German	Intermediate

Software

MS Excel, MS PowerPoint, MS Word, Outlook, R*, MatLab, LabView, Origin and Adobe Photoshop

*Attended online course on R software: The Analytics Edge offered by MITx (01/2016)

Certificates

Data-driven Decision Making, PwC (03/2016)

Laboratory and Characterization Techniques

Experienced in laboratory equipment and safety standards;
Zeta-Potential, UV-Vis Spectroscopy, TGA, Peeling Tests, Surface Electrical Properties, Laser Confocal Microscopy, XPS, Optical Tensiometer and SEM

Personal Interests

Skiing, different cultures, cuisine and artificial intelligence

Lörrach, July 2020